CHEMISTRY AND TRANSPORT OF LAYERED PHENOMENA IN THE MESOSPHERE-LOWER THERMOSPHERE

by

Christopher William Kelly

Submitted in accordance with the requirements for the degree of

PhD

The University of Leeds

School of Earth and Environment

October, 2020

The candidate confirms that the work submitted is his own, except where work which has formed part of jointly-authored publications has been included. The contribution of the candidate and the other authors to this work has been explicitly indicated below. The candidate confirms that appropriate credit has been given within the thesis where reference has been made to the work of others.

Chapter 4 is guided by a section of a Space Weather commentary paper on which the candidate is a co-author:

Jackson, D.R., Fuller-Rowell, T.J., Griffin, D.J., Griffith, M.J., Kelly, C.W., Marsh, D.R. and Walach, M.T. 2019. Future Directions for Whole Atmosphere Modeling: Developments in the Context of Space Weather. *Space Weather.* **17**(9), pp.1342-1350.

The candidate contributed towards the commentary on the role of chemistry in building blocks for better models (Section 3.2). Co-authors provided equivalent content in the other sections for their respective topics of expertise.

Chapter 6 is based on a Geophysical Research Letters paper on which the candidate is the first author:

Kelly, C.W., Chipperfield, M.P., Plane, J.M.C., Feng, W., Sheese, P.E., Walker, K.A. and Boone, C.D. 2018. An Explanation for the Nitrous Oxide Layer Observed in the Mesopause Region. *Geophysical Research Letters.* **45**(15), pp.7818–7827.

The observations referenced in this study were provided by co-authors from the Atmospheric Chemistry Experiment group at the University of Toronto and the University of Waterloo and were originally reported in a separate publication. The candidate designed and implemented the novel method used to drive the model, performed the simulations and compared the model output with the observations. All plots and evaluations performed are the candidate's own work.

ACKNOWLEDGEMENTS

First and foremost, I would like to thank my supervision team of Martyn Chipperfield, John Plane, Wuhu Feng, David Jackson and Daniel Marsh. Not only has their guidance and expertise enabled me to complete the work presented in this thesis, it has also given me an invaluable skillset for my onward career.

From Leeds, I would like to thank the past and present core members of the TOMCAT research group (Andreas, Chris, Evgenia, Giorgio, Joey, Matilda, Richard, Sandip, Tim and Yajuan) for providing such a welcoming and supportive atmosphere. On a personal note, thanks to all of my friends at ICAS, in particular Laura, Sarah and Tom, with whom I have shared both an office and the whole PhD experience.

Outside of Leeds, I would like to thank those officially and unofficially involved in my Met Office Academic Partnership, notably Daniel Griffin, James Manners, Luke Abraham, Matthew Griffith and Olaf Morgenstern. Their advice has helped me overcome various technical hurdles during my PhD.

Finally, special thanks to Mum, Dad, Stephen, Simon and of course Rosie for the incredible support and encouragement that they have all given me along the way.

I acknowledge the Natural Environment Research Council (NERC) and the UK Met Office for funding this project (NE/N008340/1).

ABSTRACT

The formation and properties of many naturally occurring layered phenomena in the mesosphere-lower thermosphere (MLT, 50-110 km) are not fully understood. Such layers, through their inclusion in chemistry-climate model studies, offer considerable insight into the chemical and transport properties of the MLT. In part, this thesis reports the first phase of chemistry developments for the Met Office's new high altitude (~120 km) chemistry-climate model: the Extended Unified Model coupled to the UK Chemistry and Aerosols scheme (Extended UM-UKCA). The initial work reported here has added a realistic representation of neutral chemistry in the MLT, focusing on atomic oxygen (O) and atomic hydrogen (H). This contributes towards the Met Office's strategic goal of a Sun-to-Earth coupled forecasting system, whilst providing a testbed for associated model performance diagnostics to be developed for the MLT. In particular, an atomic sodium (Na) chemistry diagnostic package is developed and used here to quantitatively attribute the physical and chemical deficiencies of this early version of the Extended UM-UKCA to the magnitude and variation of the resultant Na layer distribution. Motivated by recent Atmospheric Chemistry Experiment (ACE) limb satellite measurements of a layer of enhanced nitrous oxide (N_2O) in the MLT, peaking around 94 km, this thesis also reports the development of a novel N_2O production parametrisation to explain and allow a first model simulation of the observations.

With suitable extensions to O and H chemistry included, Extended UM-UKCA simulations reproduce the target climatological H profile through the MLT, but show an approximate ×10 O-excess, weighted towards the summer pole. Na chemistry diagnostic simulations reveal this as a cause of a similar magnitude Na-excess and an even greater Na^+-excess, although model transport deficiencies also contribute. The expected Na compound partitioning is reproduced, negating some discrepancies in minor compounds, partly attributable to the breakdown of assumptions in the background chemistry. Sub-grid scale physics parametrisations, such as eddy diffusion, should be prioritised in future model versions to improve vertical transport, while the provision of chemical heating will enable a more realistic seasonal temperature gradient to be generated, assisting meridional transport. A further

extension to the model lid height (≥ 140 km) is recommended to reduce the impact of atmospheric wave reflection off of the upper boundary. Simulations of the N_2O layer, performed in the reference Whole Atmosphere Community Climate Model (WACCM) to overcome noted deficiencies in the Extended UM-UKCA, provide strong quantitative support for the satellite observations. Furthermore, the results show that essentially all of the N_2O enhancement occurs through a new mechanism ($N_2(A^3\Sigma_u^+) + O_2$) based on secondary electrons. The contribution of a previously proposed mechanism ($N(^4S) + NO_2$) appears to be less important than originally suggested, attributable to no more than 20% of overall N_2O simulated at any altitude or latitude band. Therefore, the new mechanism needs to be included in relevant chemistry-climate models for a realistic description of N_2O in the MLT.

TABLE OF CONTENTS

LIST OF TABLES

LIST OF FIGURES

1 INTRODUCTION

1.1 Background

The Earth's atmosphere from the surface to around 120 km can be divided into four primary vertical layers based on the mean temperature profile (Figure 1.1): the troposphere, the stratosphere, the mesosphere and the thermosphere. The mesosphere-lower thermosphere (MLT) describes the interface between the Earth's atmosphere and outer space. It spans between about 50 and 110 km in altitude, starting above the stratosphere and extending into the first few kilometres of the thermosphere (Brasseur and Solomon, 2005).

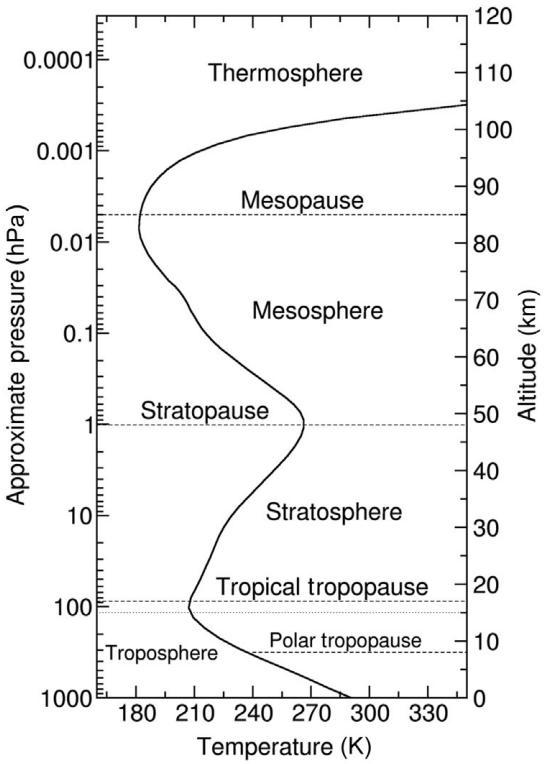

Figure 1.1 Global mean atmospheric temperature profile. From Braesicke (2015).

The distinct location of the MLT affords conditions for particularly interesting and varied atmospheric chemistry. Through this region, chemicals readily exist as a blend of compounds, atoms and ions (Mlynczak and Hunt, 2015). However, the driving force behind the chemistry of the MLT is the presence of atomic oxygen (Plane et al., 2015). Atmospheric waves play a progressively important role in constituent transport with increasing altitude through the MLT. Here, air density measures several orders of magnitude lower than surface values (Martin, 1965), causing wave amplitudes to grow exponentially with height (Vincent, 2015). Such waves drive a robust MLT circulation, causing a large seasonal temperature gradient and significant dynamical variability (Smith, 2012).

Figure 1.2 Noctilucent clouds over Leeds at 2200 UT on 21st June 2019 (photographed by author).

Different types of layered phenomena have a well-established presence in the MLT. This includes ice layers (Russell et al., 2009) observed as noctilucent clouds such as in Figure 1.2, as well as both neutral and ionised atomic metal layers derived from meteors (Plane, 2003). Significant scientific insight can be sought from the study of MLT layers. For example, changes in ice layers have been linked to anthropogenic climate change (von Zahn, 2003) and metal layers provide a tool for the study of mesospheric dynamics (Gardner et al., 2017).

The effect of solar radiation and energetic particles, known as space weather, also plays a critical role in the MLT. Chemical compounds can be dissociated, raised to states of higher energy or ionised when exposed to space weather. This mechanism drives important chemical reactions such as ozone (O_3) depletion via the production of radicals (Swider and Keneshea, 1973) and thermospheric heating through the quenching of excited atomic oxygen (Mlynczak and Solomon, 1993).

1.2 Motivation

It is no longer sufficient to individually represent the components of the Sun-to-Earth system through separate models. Such an approach is rapidly becoming incompatible with the forecasting advancements demanded by the world's leading meteorological agencies (Jackson et al., 2019). It is therefore becoming necessary to adopt a cohesive approach whereby models are combined to provide an interactive representation of processes originating from the surface of the Sun, right through to the surface of the Earth. For example, the link between solar variability and variability in tropospheric climate has been known for some time e.g. Ineson et al. (2011). Similarly, tropospheric weather has been long-known to impact the ionosphere e.g. Immel et al. (2006). However, the associated models have historically had little or no representation of the processes outside their immediate domain. Thanks to continual

advances in scientific insight and computing infrastructure, the atmospheric modelling community is now in a position to change this. Part of this thesis reports the development of an essential component to the UK Met Office's progress in this task: the coupling of chemistry to an extended altitude configuration of the Met Office climate and forecasting model. Furthermore, the formulation of this model (Griffith et al., 2020) provides a testbed to address the first two of the following three specific scientific problems.

Firstly, a suitable method for representing neutral chemistry in the MLT has not yet been established in the context of the new Met Office model. Central to this is ensuring that the vertical upper boundary of the model accounts for the truncation of the atmosphere at the initial model lid height of 120 km. This is typically done by prescribing the top level of key constituents to an external source of data. An existing US coupled chemistry-climate model of the whole-atmosphere with a comparable altitude limit (Gettelman et al., 2019) uses data from an empirical model (Picone et al., 2002) for this purpose. However, a case has been made for using full numerical models with complete descriptions of the thermosphere instead, based on recent technical developments e.g. Liu et al. (2018). There is therefore motivation to review the suitability of prescribing output from such models as vertical upper boundary conditions for the neutral chemistry of the new Met Office model.

Secondly, there is uncertainty in the role of chemistry and transport on the distribution and seasonal variation of the atomic sodium (Na) layer (an atomic metal layer) in the MLT. The Na layer comprises various short-lived intermediate compounds that are not directly observable (Plane, 2015). At present, the previously mentioned US model is the only fully interactive chemistry-climate model that has been used to simulate this phenomenon. The new Met Office model offers a unique opportunity to investigate connections between the simulated background MLT and the resulting Na layer composition, based on the known chemical and physical differences between the models. Furthermore, such experiments will assist the understanding of the magnitude and profile of the meteoric input itself – an issue highlighted by a recent model study (Li et al., 2018).

Finally, the impact of space weather on MLT chemistry is not comprehensively understood. This is in part due to the sparsity of chemical observations available above

the mesopause (Jackson et al., 2019). When such observations are made, they are often uncorroborated. This is true for the first satellite measurements of a nitrous oxide (N_2O) layer in the mesopause region, reported by Sheese et al. (2016). It is important that all sources of atmospheric N_2O production are quantitatively accounted for, as N_2O is an important greenhouse gas and is now, due to the decline in halogenated source gases, considered the most important anthropogenic ozone-depleter (Ravishankara et al., 2009). There is therefore immediate motivation to develop a reasonable mechanism for this unexpected source.

1.3 Objectives

The overall objective of this thesis is to further scientific understanding of the chemical and transport properties of layered phenomena in the MLT. It focuses on the provision of new modelling tools, from the development of chemistry for a climate model of the whole atmosphere, to parametrisations of individual novel atmospheric processes. The results from this work intend to establish the atomic Na layer as a suitable diagnostic of model chemistry and transport, as well as provide the first model explanation for uncorroborated observations of an N_2O layer. The specific research questions are:

1. How does the Met Office's chemistry-climate model perform in the MLT and what is the best way to optimise neutral chemistry below the 120 km lid?
2. How does the chemical and physical structure of the background MLT influence the distribution and seasonal evolution of the atomic Na layer?
3. What is the underlying mechanism behind novel observations of an N_2O layer in the mesopause region?

The research approach is split into two stages. The first stage, which addresses question 1, is to provide a suitable representation of neutral chemistry in the MLT for the Met Office Unified Model with thermospheric extension (Extended UM). The framework for this will be provided by the UK Chemistry and Aerosols (UKCA) scheme, thus creating the Extended UM-UKCA. Important photochemical reactions in the MLT need to be either added, parametrised or extended (if already present). In addition, the case for representing the impact of important thermospheric processes from above the new model lid needs to be considered for selected chemical tracers.

The successful completion of this research stage is essential to suitably represent the key components of the MLT: atomic oxygen, atomic hydrogen and temperature.

The second stage is to utilise the new model alongside existing modelling tools to answer research questions 2 and 3. This will happen with the development of: i) an atomic Na chemistry scheme for the Extended UM-UKCA; and ii) a lower-thermospheric N_2O production mechanism for an existing chemistry-climate model. Simulations of the atomic Na layer can be used to diagnose chemical and physical deficiencies in the simulated background MLT, while the physical reasoning behind the N_2O production mechanism can be used to explain the previously unaccounted for observations.

1.4 Thesis Layout

The work documented in this thesis is split into seven chapters. Chapter 2 presents background information on the chemistry, composition and transport properties of the MLT, including focused literature reviews on both the Na layer and the N_2O layer. Chapter 3 provides individual descriptions of the various models and observations used in this thesis, with particular attention payed to the Extended UM. Chapter 4 introduces the Extended UM-UKCA, specifically reporting developments to the treatment of photolysis, the inclusion of upper-boundary conditions and the provision of offline chemical heating rate calculations. Chapter 5 describes the method used to implement a sodium chemistry scheme in the Extended UM-UKCA and investigates the chemistry and transport of the Na layer in the new model. Chapter 6 describes the mechanism derived to parametrise N_2O production in the MLT and provides the first model explanation for the observations of a lower-thermospheric source. Finally, Chapter 7 summarises the scientific findings from this thesis within the context of the original objectives and research questions.

2 THE MESOSPHERE-LOWER THERMOSPHERE

2.1 Introduction

The mesosphere-lower thermosphere (MLT) is characterised by a variety of physical and chemical properties. Knowledge of the driving processes for, and the implications of, such properties is essential in our quest to better understand this unique region of the atmosphere.

In this chapter, I review key literature that documents the MLT to provide a scientific background for the research questions proposed in Chapter 1. Where applicable, I also provide context with other parts of the atmosphere. Section 2.2 introduces the composition and chemistry of the MLT. Section 2.3 summarises the thermal properties of the region, while Section 2.4 reviews constituent transport. Section 2.5 provides an overview of space weather – a major driver of atmospheric chemistry in the MLT. Sections 2.6 and 2.7 review existing scientific understanding of the two atmospheric layered phenomena particularly relevant to this thesis: Section 2.6 considers the atomic sodium layer, while Section 2.7 considers the novel nitrous oxide layer. The key points from this literature review are summarised in Section 2.8.

2.2 Composition and Chemistry

The region of the atmosphere below 100 km in altitude is known as the homosphere. This is because molecular nitrogen (N_2) and molecular oxygen (O_2) uniformly constitute about 80 and 20%, respectively, of the total number density. As a result of this, the vertical variation of mean molecular mass is small (Brasseur and Solomon, 2005). Upwards of 100 km, diffusive separation occurs between compounds. Through diffusive separation, the most lightweight compounds are lifted upwards, while the heavier compounds are brought downwards. This, combined with significant O_2 photolysis above 80 km, means that atomic oxygen (O) becomes the increasingly dominant chemical component with altitude, while N_2 and O_2 abundances become

increasingly less significant. To reflect this vertical variation in composition, the region of the atmosphere above 100 km is called the heterosphere (Brasseur and Solomon, 2005). Particularly lightweight species, such as atomic hydrogen (H) and helium (He) are also important, especially towards the top of the heterosphere. Figure 2.1 depicts the relative contributions of N_2, O_2 and O to the total number density of the heterosphere, up to an altitude of 500 km.

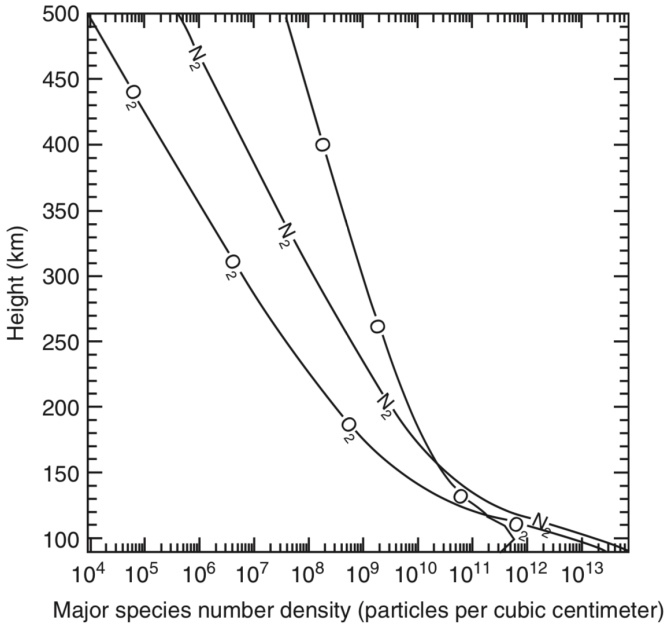

Figure 2.1 Global mean profiles of the three major chemical components of the heterosphere, calculated for solar medium conditions. From Solomon and Roble (2015).

2.2.1 Atomic Oxygen and Atomic Hydrogen

The MLT extends between about 50 and 110 km in altitude, across the threshold between the homosphere and heterosphere. Atmospheric density in this region is sufficiently low enough to support the existence of O and H populations that would otherwise be quickly consumed by chemical reactions (Mlynczak and Hunt, 2015). The chemistry of the MLT is dominated by the reactions of O (Plane et al., 2015). By far, the main source of O is through the photolysis of O_2

$$O_2 + h\nu \rightarrow O(^3P) + O(^3P). \qquad \text{(R2.01)}$$

The global mean concentration of O peaks at around 95 km, where it is typically between 4 and 6×10^{11} cm^{-3}. O density is modulated by the 11-year solar cycle, with the upper limit of this range realised at solar maximum and the lower limit at solar minimum (Mlynczak and Hunt, 2015). The primary mechanism for O destruction occurs through the following reaction series, as listed by Plane et al. (2015):

$$O + O_2 + M \rightarrow O_3 + M \quad \text{(R2.02)}$$

$$H + O_3 \rightarrow OH + O_2 \quad \text{(R2.03)}$$

$$O + OH \rightarrow H + O_2 \quad \text{(R2.04)}$$

$$H + O_2 + M \rightarrow HO_2 + M \quad \text{(R2.05)}$$

$$O + HO_2 \rightarrow OH + O_2 \quad \text{(R2.06)}$$

Below about 80 km, the chemical lifetime of O is less than a day, yielding a diurnal variation in its distribution (Friederich et al., 1999). Here, typical day-side concentrations of O are several orders of magnitude greater than the corresponding night-side concentrations. However, since atmospheric density falls by approximately an order of magnitude for every 5 km altitude increment in the MLT, so does the rate of reaction R2.02 (Plane et al., 2015). Hence, there is no distinguishable diurnal variation in O throughout the upper portion of the MLT, with the typical chemical lifetime of O being 1 year at 105 km (Friederich et al., 1999). H acts as a catalyst through reactions R2.03 and R2.04, enabling the removal of O in the MLT. The predominant source of H in the MLT is the photolysis of water vapour at Lyman-α (121.6 nm)

$$H_2O + h\nu \rightarrow OH + H \quad \text{(R2.07)}$$

(Verronen et al., 2013). Note that this channel is not an important source of H in the lower atmosphere, where photolysis occurs at longer wavelengths. H follows a similar diurnal distribution pattern to O throughout the MLT, due to their closely aligned chemistry schemes (Plane et al., 2015). The other product of reaction R2.07, OH, is part of the odd hydrogen ($HO_x = H + OH + HO_2$) family, responsible for significant ozone (O_3) destruction. Details of this process are provided in Section 2.5.2. A discussion on ozone destruction caused by odd nitrogen and other reactive nitrogen compounds ($NO_y = NO + NO_2 + NO_3 + HNO_3 + \ldots$) is also provided in the same section.

2.2.2 The Ions

The harsh environment of solar radiation in the MLT can cause ionisation of the chemical constituents at all latitudes. That is:

$$X + h\nu \rightarrow X^+ + e^-, \qquad \text{(R2.08)}$$

where X is a neutral atom or molecule, $h\nu$ is UV or X-ray solar radiation, X^+ is an ionised atom or molecule and e^- is a liberated electron. Towards the poles, energetic particle precipitation (EPP, see Section 2.5) may induce the same effect through:

$$X + e^* \rightarrow X^+ + 2e^-, \qquad \text{(R2.09)}$$

where e^* is an energetic electron or proton (Brasseur and Solomon, 2005). The region of the atmosphere where such ionisation occurs is named the ionosphere, which extends vertically over the upper mesosphere and a large part of the thermosphere. The ionosphere is split by altitude range into three regions: the *D* region (<90 km), the *E* region (90-150 km) and the *F* region (150-500 km) (Kelley, 2009). Total ion density exhibits a significant diurnal variation (shown for the *E* region in Figure 2.2). Here, peak density is up to a factor of 100 smaller on the night-side than it is on day-side, as without the primary ionisation source of solar radiation, the dissociative recombination of molecular ions through

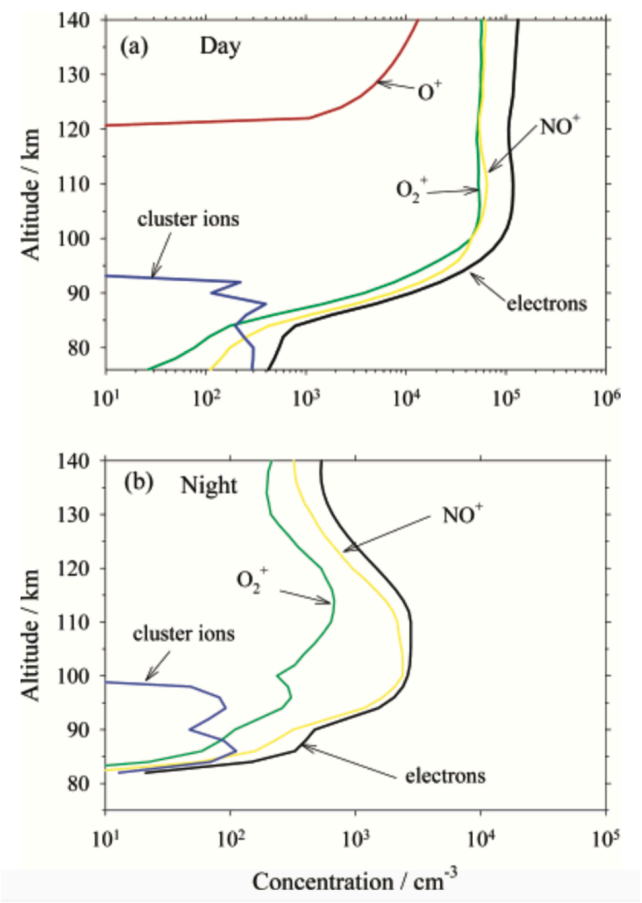

Figure 2.2 Diurnal variation in the chemical composition of the ionosphere. From Plane (2003).

$$O_2^+ + e^- \rightarrow O + O \qquad \text{(R2.10)}$$

and

$$NO^+ + e^- \rightarrow N + O \qquad \text{(R2.11)}$$

outweighs their EPP-induced production. This does not happen to the atomic ions in the *F* region, as maintaining energy and momentum conservation is kinetically unfavourable in single-product recombinations such as

$$O^+ + e^- \rightarrow O. \qquad \text{(R2.12)}$$

In addition, the rates of such reactions are small (Kelley, 2015).

2.2.3 Atomic Metal Layers

An interesting chemical feature of the MLT is its support of various atomic metal layers. The Earth's atmosphere has a continuous input of material from meteoroids, sourced primarily from dust trails of sublimating comets and fragments of the asteroid belt (Plane, 2003). Metals constitute a proportion of the mass of meteoroids. Upon atmospheric entry, the contained metals are ablated at various efficiencies, causing the injection of different metal atoms at different altitudes (Plane, 2015). A recent estimate for the total meteoric mass injection rate is 43 ± 14 t d^{-1} (Carrillo-Sánchez et al., 2016). The relative abundances of ozone and O are important in meteoric metal chemistry. Upon reaction with ozone, metal atoms are converted to metal oxides, enabling the subsequent formation of a range of compounds. Reaction of such compounds with O, however, reduces the compounds and reforms the metal atoms. Since the MLT exhibits a greater abundance of O than ozone above about 80 km (Plane, 2015), the metals are able to maintain their atomic configurations in the MLT. Meteoric metals are heavily involved in both the neutral and ion chemistry of the MLT, with neutral compounds

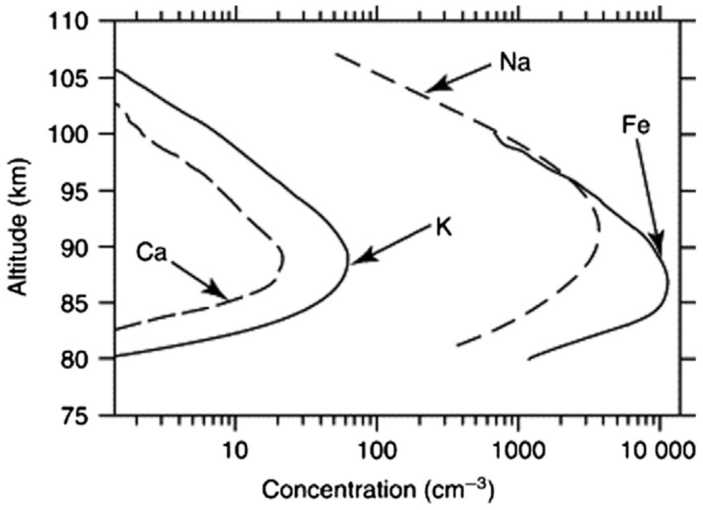

Figure 2.3 Annual mean altitude profiles of Fe, Na, K and Ca based on LIDAR observations. From Plane (2015).

dominating below about 100 km and ionic compounds dominating above (Plane et al., 2015).

Particularly notable atomic metal layers include those of iron (Fe), sodium (Na), potassium (K) and calcium (Ca). Altitude profiles for each of these species are shown in Figure 2.3. Since the Na layer is the topic of interest in Chapter 5, Section 2.6 of this literature review provides a separate, more detailed discussion specific to the status of Na layer research.

2.3 Thermal Properties

The primary vertical layers of the Earth's atmosphere are assigned based on their thermal properties. Shown in Figure 1.1 of Chapter 1, in order of ascending altitude, they include the troposphere, the stratosphere, the mesosphere and the thermosphere. In the troposphere, atmospheric temperature decreases with height, up to an inversion point called the tropopause. In the stratosphere, temperature increases with height, up to another inversion point called the stratopause. Temperature decreases with height once again in the mesosphere, up to the next inversion point called the mesopause. The coldest natural temperatures on Earth are recorded at the mesopause during polar summer (Varney and Kelley, 2015), a feature that makes the MLT a particularly interesting region to study. Above the mesopause is the thermosphere, where temperature continually increases with height.

Absorption of short-wave solar radiation largely provides the radiative heating of the lower and middle atmosphere. This is dominated by water vapour in the troposphere and ozone in the stratosphere (Brasseur and Solomon, 2005). Such heating is approximately balanced by cooling through the emission of long-wave radiation (Andrews, 2000). As with the heating, this is dominated by water vapour in the troposphere, but by carbon dioxide in the stratosphere (Brasseur and Solomon, 2005). Upwards through the MLT, there are short-wave heating contributions from ozone and increasingly O_2. Longwave cooling in the MLT is primarily provided by carbon dioxide (Brasseur and Solomon, 2005), but nitric oxide (NO) has a role in the lower thermosphere (Knipp et al., 2017). In the ionosphere, joule heating (transformation of electrical energy to heat through collisions between electrons, neutrals and ions (Kato, 1962)) arises. The contributions of both joule heating and NO cooling are enhanced

during and after space weather events (see Section 2.5), when energetic particle fluxes and NO densities are increased. The opposing radiative impact of each process acts as a thermostat on lower-thermospheric temperature (Knipp et al., 2017). However, it is chemical heating that provides the overall largest source of heating in the MLT (Marsh et al., 2007).

The enthalpy change, ΔH, describes the heat evolved from a process under constant pressure. For chemical reactions, that is the difference between the enthalpies of the products and the enthalpies of the reactants. If $\Delta H > 0$, heat is required to initiate the reaction which is described as endothermic. Conversely, if $\Delta H < 0$, heat is released by the reaction which is exothermic (Andrews, 2000). Photolysis (the breaking up of molecules by light) initiates exothermic reactions in the MLT (Marsh et al., 2007). A high proportion of the absorbed energy is converted to chemical energy. As the density of the MLT is low, large separation exists between particles. It can therefore take time for such chemical energy to be released as heat through subsequent chemical reactions (Mlynczak and Solomon, 1993). The principal source of chemical heating in the MLT is through reactions involving O atoms (Brasseur and Solomon, 2005).

2.4 Transport Properties

Atmospheric transport occurs on a variety of different spatial and temporal scales. Transport processes are broadly split into two key regimes: large-scale advection and small-scale turbulence (Brasseur and Solomon, 2005). To assess the net flow of air parcels through a particular region of the atmosphere, large-scale advection should be considered. The principal drivers of large-scale advection are i) the upwards propagation of tropospheric waves and ii) the variation of incident solar radiation. Key examples of tropospheric waves include gravity waves and planetary waves. Gravity waves are compressional oscillations formed by the vertical displacement and subsequent gravity-induced restoration of air parcels, initially triggered by topography or convection (Fritts, 2015). Planetary waves are global oscillations driven by the rotational forces of the Earth, formed by the angular displacement of air parcels and subsequent restoration by the Coriolis force (Smith and Perlwitz, 2015).

2.4.1 Transport Circulation

Figure 2.4 depicts transport circulation in the middle atmosphere. A form of meridional circulation occurs in the stratosphere, known as the Brewer-Dobson Circulation (BDC) (Brewer, 1949; Dobson, 1956). The leading driving force of the BDC is energy deposition from planetary waves, although gravity waves are also a contributing factor (Cohen et al., 2014). Upwelling of air parcels occurs in the tropical lower stratosphere, before air is carried poleward and downward by the BDC in both hemispheres (Strahan, 2015). Above this exists a different meridional circulation pattern in the MLT. The several orders of magnitude reduction in air density (Martin, 1965) affords conditions for exponential growth of gravity wave magnitudes (Vincent, 2015). Hence it is gravity waves that provide the major driving force of circulation in the MLT (Brasseur and Solomon, 2005). Mesospheric air is lifted from the summer pole and transported across towards the winter pole, where it descends. This results in adiabatic cooling over the summer pole and adiabatic heating over the winter pole, responsible for temperature perturbations of up to 50 K (Vincent, 2015).

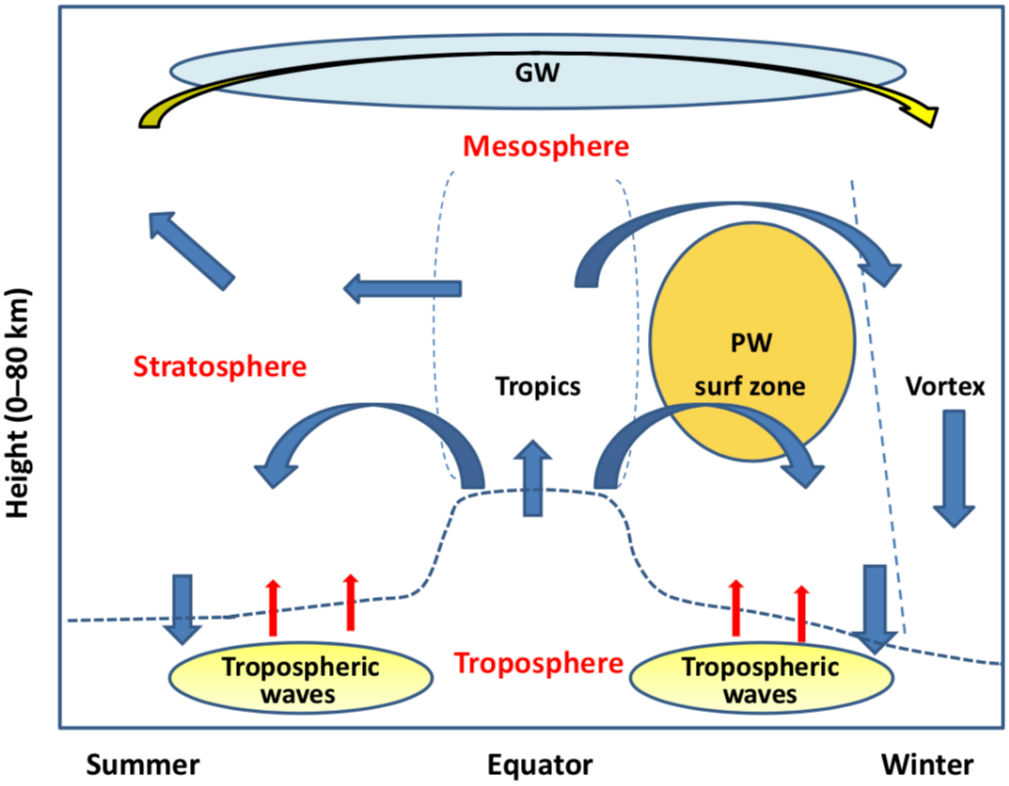

Figure 2.4 Schematic of the mean transport circulation in the middle atmosphere. From Strahan (2015).

The polar regions also host an important dynamical feature, known as the wintertime polar vortex. During winter, a portion of the atmosphere enters polar night. Here, there is no longer a short-wave heating contribution from ozone (see Section 2.3) causing temperatures to fall and air to descend. Since the tropics continue to be heated, a temperature gradient forms between the wintertime pole and the equator. This temperature gradient drives a strong pressure gradient, causing air to be forced poleward through a flow pattern known as the polar jet. The Coriolis force induces zonal motions on the polar jet, generating the wintertime polar vortex. The wintertime polar vortex extends from the tropopause to the stratopause (Schoeberl and Newman, 2015). Strong winds of the subpolar jets create a dynamical barrier against meridional transport, isolating the wintertime polar regions from the rest of the stratosphere (Brasseur and Solomon, 2005).

Upwards through the thermosphere, the summer-to-winter mean circulation pattern of the MLT is maintained (Solomon and Roble, 2015), although dynamical processes become governed primarily by the *in situ* absorption of solar radiation (Brasseur and Solomon, 2005). The day-side of the thermosphere expands as it is heated, inducing a pressure gradient against the night-side, which in turn drives zonal winds (Solomon and Roble, 2015). Variations in solar activity levels are known to impact this flow. In general, wind velocities increase with solar activity, although this is the result of a balance between competing processes. High solar activity intensifies the zonal pressure gradient and reduces kinematic viscosity, which both accelerate winds. However, under the same conditions, wind damping from enhanced electron density and ion drag increases (Hedin and Mayr, 1987).

2.4.2 Atmospheric Tides

Further global-scale waves, known as atmospheric tides exist throughout the MLT. Atmospheric tides have periods that are harmonics of a solar day. Notably, there is a 24-hourly diurnal tide and a 12-hourly semidiurnal tide (Hagan et al., 2001). Tides that propagate in sequence with the Sun's apparent zonal motion are referred to as migrating tides, otherwise they are called non-migrating tides. The principal driver of migrating tides is the daily radiative heating cycle in the middle and lower atmosphere, caused by the periodic absorption of short-wave solar radiation (see Section 2.3). The principal driver for non-migrating tides is instead latent heat release

in the troposphere (Brasseur and Solomon, 2005). Similar to the propagation of gravity waves in the MLT, the amplitude of atmospheric tides increases rapidly with height. The diurnal tide is observed to reach altitudes of up to about 110 km, while the semidiurnal tide may reach up to 300 km. However, it is from the mesopause up to about 200 km where such tidal forcing from the lower atmosphere has a significant impact on thermospheric dynamics (Solomon and Roble, 2015). Consequently, this region also sees tidal variations in atmospheric temperature. Typical temperature perturbations of 10 K are recorded at 100-120 km, increasing to 100 K at 150 km (Brasseur and Solomon, 2005).

2.4.3 Diffusive Separation

Another source of vertical transport in the thermosphere is diffusive separation above 100 km (see Section 2.2). This differs to the previously discussed transport mechanisms, as it acts on individual compounds based on their relative mass, rather than as a bulk motion in the atmosphere.

2.5 Space Weather

The MLT is particularly susceptible to space weather. Space weather primarily describes the effect of long-term and sudden changes in solar activity on the terrestrial environment (Hapgood, 2017). An official definition was devised by the European Cooperation in Science and Technology (COST) Action 724 in 2007:

“Space weather is the physical and phenomenological state of natural space environments. The associated discipline aims, through observation, monitoring, analysis and modelling, at understanding and predicting the state of the Sun, the interplanetary and planetary environments, and the solar and non-solar driven perturbations that affect them, and also at forecasting and nowcasting the potential impacts on biological and technological systems.” (COST, 2007)

2.5.1 Sources of Space Weather

Space weather is mainly caused by solar activity changes on timescales from centuries to hours, but also by galactic cosmic rays (GCRs) from outside the solar system. Historically, solar activity is known to enter long-term periods of grand minima and

maxima (Lockwood et al., 2012). Within this trend is the previously mentioned 11-year solar cycle, whereby solar UV and the solar wind periodically oscillate in flux. Most unpredictable are single-event effects, caused by rapidly occurring phenomena such as solar radiation storms and severe energetic particle precipitation (EPP) (Hapgood, 2017). Solar radiation storms arise from a plasma process known as magnetic reconnection. This is often followed by coronal mass ejections (CMEs) and solar flares. CMEs are violent releases of solar plasma, while solar flares are bursts of X-ray and extreme-UV (EUV) radiation (Hapgood, 2017). EPP includes protons, electrons, and some larger ions that have been accelerated either directly by the sun during CMEs or solar proton events (SPEs), by radiation belts during geomagnetic storms, or by GCRs (Sinnhuber et al., 2012).

Space weather impacts the physical and chemical properties of the MLT through both solar activity trends and single-event effects. For example, atmospheric temperature and hence neutral density are modulated by geomagnetic activity, while space weather initiates chemical processes in the MLT (Pulkkinen, 2007) (see the following section). Figure 2.5 shows an example of space weather propagation and impact, including its inception at the Sun, dissipation through the Earth's magnetic field and observation as the aurora.

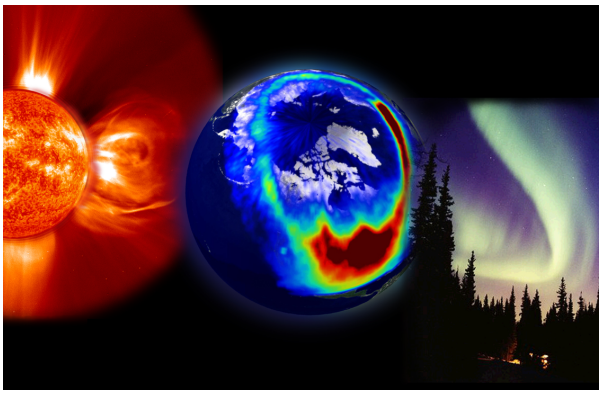

Figure 2.5 Illustrative representation of space weather. Includes a solar storm (left), the Earth's auroral oval (middle) and the aurora borealis (right). Image credit: NASA.

2.5.2 Impact on Atmospheric Chemistry

Stratospheric ozone depletion has been attributed to mesospheric production of NO_y (Crutzen et al., 1975; Funke et al., 2005), and more recently HO_x (Verronen et al., 2013) after EPP events. NO_y-induced ozone depletion occurs through the 'direct effect', as well as the 'indirect effect'. The former refers to the *in situ* destruction of mesospheric and upper stratospheric ozone (Funke et al., 2011; Jackman et al., 2001) Conversely, the indirect effect occurs when NO_y is transported down to the

stratosphere through confinement in the wintertime polar vortex (see Section 2.4.1). This transport is enabled by the typical lifetime of NO_y being around 1 month at 60 km (Brasseur and Solomon, 2005). The main route for mesospheric NO_y production at all latitudes involves the photolysis of N_2

$$N_2 + h\nu \rightarrow N(^4S) + N(^2D), \quad \text{(R2.13)}$$

although EPP also causes significant N_2 dissociation over the polar regions ($N_2 + e^* \rightarrow N(^4S) + N(^2D) + e^-$). This is followed by the reaction of ground or first excited state atomic nitrogen with oxygen

$$N(^4S, ^2D) + O_2 \rightarrow NO + O \quad \text{(R2.14)}$$

(Funke et al., 2005). Ozone is then catalytically destroyed in the stratosphere via

$$NO + O_3 \rightarrow NO_2 + O_2 \quad \text{(R2.15)}$$

and

$$NO_2 + O \rightarrow NO + O_2 \quad \text{(R2.16)}$$

(McElroy et al., 1992).

The most significant example of ozone depletion via the indirect effect, so-far documented, occurred after the extreme solar storms and associated SPEs of late October 2003 and the strong Sudden Stratospheric Warming (SSW) of December 2003. Randall et al. (2005) reported satellite observations of stratospheric NO_y mixing ratios of around 80 ppb at 40 km over some locations, with corresponding stratospheric ozone depletion of up to 60%. It was recognised that this extraordinary event was caused by a combination of both severe EPP and favourable meteorological conditions (Randall et al., 2005). A study by Manney et al. (2005) described the 2003-2004 major stratospheric warming and subsequent rapid, exceptionally strong recovery of the polar vortex. Later work by Randall et al. (2006) reported large mixing ratios of stratospheric NO_y in 2005-2006. Unlike 2003-2004 there was no significant geomagnetic activity that winter, however there was again an exceptionally strong polar vortex. It appeared that the large stratospheric NO_y mixing ratios observed in 2003-2004 could not be attributed to EPP from the SPEs alone, which had their impact erased by the SSW. Sinnhuber et al. (2014) found the influence of EPP-NO_y from the

indirect effect to exceed the direct impact of the SPE by nearly a factor of 10. However, it was hypothesised by Lu et al. (2008) that the solar wind itself could partly influence the strength of the wintertime polar vortex. Baumgaertner et al. (2011) performed atmospheric chemistry general circulation model simulations that linked high geomagnetic activity levels to a strong polar vortex, mediated by NO_y-induced stratospheric ozone loss. These findings were verified by Seppälä et al. (2013), who summarised the impact of geomagnetic activity on stratospheric and tropospheric dynamics:

- "Reduced upward propagation of waves into the stratosphere in early winter, followed by
- Enhanced equatorward reflection of waves from the polar vortex edge,
- Warming of the polar upper stratosphere and cooling below, starting in December–January and continuing into March,
- Descent of the warming signal from January to March,
- Anomalously strong polar vortex in late winter, as measured by changes in zonal mean zonal winds, leading to positive Northern Annular Mode anomalies."

Mechanisms for NO_y production other than reactions R2.13 and R2.14 exist. One example, the reaction

$$N_2O + O(^1D) \rightarrow 2NO \qquad \text{(R2.17)}$$

is the primary source of NO_y in the lower and middle stratosphere (Portmann et al., 2012). Since the nitrous oxide (N_2O) involved in this process originates from surface emissions (Brasseur and Solomon, 2005), it is traditionally considered that the MLT contains no appreciable quantity of N_2O. Novel observations of an N_2O layer in the MLT provide the motivation for Chapter 6 of this thesis. Section 2.7 of this literature review provides the scientific background for *in situ* N_2O production in the MLT.

Ozone depletion by HO_x is limited to the direct effect, as HO_x is short-lived and not transported far. Typically, HO_x will exist for around 1 hour at an altitude of 60 km (Brasseur and Solomon, 2005). Similar to NO_y production, the primary mechanism for HO_x production at all latitudes in the mesosphere is the photolysis of water vapour (reaction R2.07) (Verronen et al., 2013). However, during EPP events the enhanced

ionisation causes additional HO_x production in polar regions via water cluster ion chemistry (Verronen and Lehmann, 2013). Subsequent ozone destruction then occurs largely through the catalytic cycle

$$OH + O_3 \rightarrow HO_2 + O_2 \quad \text{(R2.18)}$$

and

$$HO_2 + O_3 \rightarrow OH + 2O_2 \quad \text{(R2.19)}$$

(McElroy et al., 1992). Andersson et al. (2014) observed up to 90% short-term ozone depletion at 60-80 km during severe energetic electron precipitation (EEP) events. The occurrence of severe EEP events (defined by Andersson et al. (2014) as when the daily mean Medium Energy Proton and Electron Detector (MEPED) electron precipitation count rate exceeds 150 counts s^{-1}) has been correlated to the 11-year solar cycle. Interestingly, for solar cycle 23 (1996-2008), most severe EEP events were observed during the transition between the solar maximum and the following minimum. Andersson et al. (2014) suggested that although ozone depletion from single EEP events is short lived, the combined impact from frequent events could lead to mesospheric ozone variability on solar cycle timescales.

EEP can be divided into three energy categories: low-energy/auroral (less than 30 keV) electrons (LEE), medium-energy (between 30 and 300 keV) electrons (MEE), and high-energy (between 300 keV and several MeV) electrons (HEE) (Brasseur and Solomon, 2005). Historically, chemistry-climate model studies have only included the contribution of LEE (e.g. (Baumgaertner et al., 2009; Rozanov et al., 2012)). However, the contribution of MEE was included in simulations reported by Arsenovic et al. (2016). The authors attributed a proportion of the NO_y generated by the model to MEE, and found that with this additional source, the model better replicated satellite observations of NO_y. To fully represent the importance of EPP on atmospheric chemistry, future model studies will need to also incorporate HEE.

GCRs have been shown to influence surface climate through atmospheric chemistry. Incident GCRs ionise atmospheric gas molecules and the resulting charged secondary particles cause further ionisation down into the atmosphere, reaching depths dependent on the original GCR energy. Calisto et al. (2011) reported chemistry-

climate model simulations assessing the impact of such GCR-induced ionisation cascades on NO_y, HO_x and ozone. In the lower stratosphere, they found NO_y enhancements of up to 4% and corresponding ozone decreases of over 3% in the Northern Hemisphere (NH) polar region. This can be largely attributed to the NO_y catalytic ozone depletion cycle given by Reactions R2.15 and R2.16. In the troposphere, NO_y enhancements of up to 20% were simulated in the Southern Hemisphere (SH) polar region, leading to ozone increases of up to 3%. NO_y is a precursor to ozone production in the troposphere through the photolysis of NO_2

$$NO_2 + h\nu \rightarrow NO + O \qquad \text{(R2.20)}$$

followed by the association of O and O_2 with the presence of a third body, M,

$$O + O_2 + M \rightarrow O_3 + M \qquad \text{(R2.21)}$$

(Monks et al., 2015). Although GCRs also cause HO_x production, Calisto et al. (2011) simulate a net reduction in HO_x across the atmosphere when GCR impacts are included. Any HO_x enhancements are surpassed by an improved efficiency of NO_y-induced OH removal through

$$OH + NO_2 + M \rightarrow HNO_3 + M \qquad \text{(R2.22)}$$

due the large abundance of NO_y (Jackman et al., 2016). Maximum HO_x reductions of around 3% were reported by Calisto et al. (2011), occurring in the middle latitudes of the upper troposphere. Corresponding meteorological results from this study during NH winter include an acceleration of zonal wind of up to 5 m s^{-1} below 40 km, and a deceleration of up to 3 m s^{-1} above 70 km. Surface air warming of around 2 K was identified in Eastern Europe and Russia, whereas cooling of a similar magnitude was reported in Siberia and Greenland (Calisto et al., 2011).

Jackman et al. (2016) obtained similar results from their chemistry-climate model simulations, reporting maximum polar NO_y enhancements of 6% in the NH and 15% in the SH, occurring in the lower stratosphere and troposphere, respectively. Their corresponding ozone changes for the same regions were slightly smaller than Calisto et al. (2011), yielding a reduction of up to 1% in the NH lower stratosphere, and an increase of up to 2% in the SH troposphere. Both studies attributed this latitudinal ozone variation to the fact that the SH is the lesser polluted hemisphere, concluding

that ozone production is more sensitive to supplementary NO_y from GCR in the SH, than it is in the NH (Calisto et al., 2011; Jackman et al., 2016).

2.6 The Atomic Sodium Layer

From the atomic metal layers discussed in Section 2.2.3, it is the Na layer that has been studied the most comprehensively. This is largely because it is the easiest to observe through spectroscopy. For example, while Mg is the most abundant metallic constituent of meteoroids, visibility of its optical transition at 285.2 nm is blocked by the stratospheric ozone layer (Plane, 2015). Scientific understanding of the formation and evolution of the Na layer has progressed rapidly in the last few years as a result of better observations, focused laboratory studies and computational advancements.

2.6.1 Physical and Chemical Properties

The atomic Na layer exists globally in the MLT, peaking at between 88 and 92 km altitude (Plane, 2003). Na atoms are sourced from meteoric ablation, as described in Section 2.2.3. The Na layer is an excellent tracer of constituent transport in the MLT due to two key properties: i) it has a relatively long chemical lifetime of over a day (Xu and Smith, 2003) and ii) it exerts a strong sensitivity to temperature (Plane, 2003). Its involvement in both neutral and ion-molecule reactions results in the formation of various other Na compounds, as shown in Figure 2.6. Above 100 km, ion chemistry generally dominates, allowing Na^+ to become the major constituent of the layer. It is only at the 80 km O shelf (see Section 2.2.3) where metal oxidation begins to take

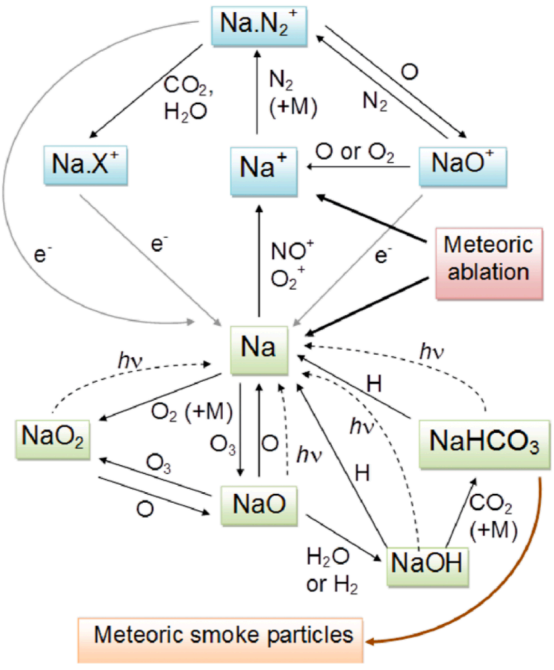

Figure 2.6 Schematic depicting the chemical interactions between Na layer compounds in the MLT. From Plane et al. (2015).

over and the stable reservoir of $NaHCO_3$ provides an efficient sink of atomic Na (Plane, 2015).

2.6.2 Observations

An emission of 589 nm light in the Earth's airglow was originally reported in the 1920s. A few years later Sydney Chapman suggested an electronic state transition in Na as an explanation for the source of the emission (Plane, 2015). Ground-based photometers were then used in the 1950s to measure the emissions and provide the first quantitative observations of the Na layer (Plane et al., 2015). At present, there are two main methods used to observe the Na layer. Firstly, the resonance lidar technique (Plane, 2003) and secondly, satellite limb-scanning spectroscopy (Plane et al., 2015).

There are a significant number of Na layer observations made from ground-based lidar instruments across the globe, e.g. (Gardner et al., 2005; States and Gardner, 1999; Zhou et al., 2005). The layer has also been observed by three satellite instruments: the Global Ozone Measurement by Occultation of Stars (GOMOS) (Fussen et al., 2010) the Optical Spectrograph and Infra-Red Imager System (OSIRIS) (Fan et al., 2007; Gumbel et al., 2007; Hedin and Gumbel, 2011) and the SCanning Imaging Absorption spectroMeter for Atmospheric CHartographY (SCIAMACHY) (Casadio et al., 2007) (see Chapter 3 for descriptions of each instrument). Although there are currently no operational observations of the Na^+ component of the layer, measurements from historical rocket launches exist (e.g. (Kopp, 1997), see Chapter 3). It is only Na and Na^+ that can be directly observed (Plane, 2015), therefore studies using computational models are essential for understanding Na layer chemistry.

2.6.3 Model Studies

The Na layer has been studied by various generations of models through the computational era. Examples include early models where the steady-state assumption is applied to Na chemistry (McNeil et al., 1995), independent time-resolved models (Plane, 2004) and nonlinear models with representation of atmospheric waves (Xu and Smith, 2004). More recently, Marsh et al. (2013) provided the first integration of a meteoric Na scheme into a fully interactive chemistry-climate model. Their study used the Whole Atmosphere Community Climate Model (WACCM) (Marsh et al.,

2013). WACCM simulations well-replicated the observed global distribution and seasonal variation of Na. Figure 2.7 shows a plot from the study, where total column monthly means of Na are compared against lidar observations. Marsh et al. (2013) also provided computational support to the observations of Fussen et al. (2010), indicating that the Na layer is strongly influenced by the MLT global circulation.

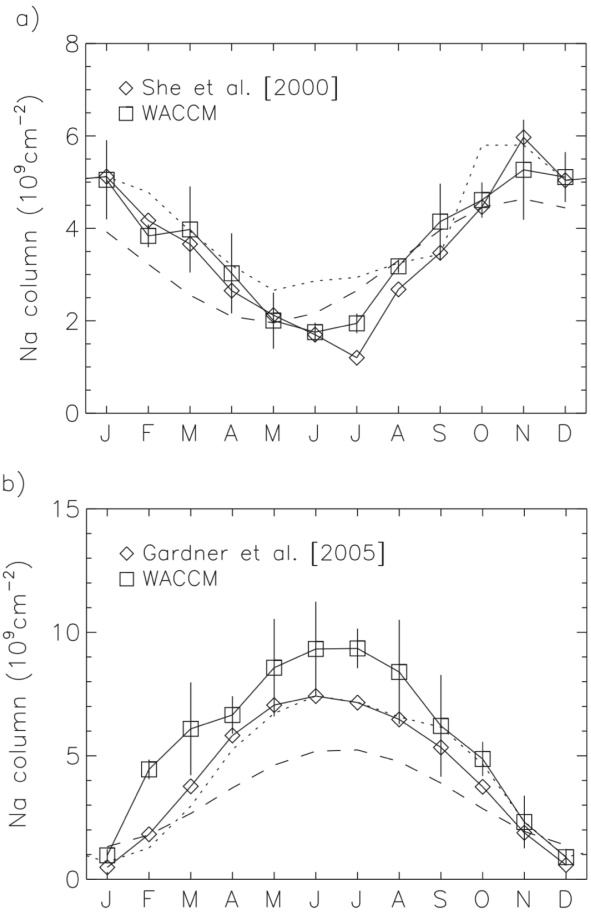

Figure 2.7 WACCM vs. lidar observations. Total column (10^9 cm^{-2}) monthly mean of Na for (a) Fort Collins and (b) South Pole lidar observations. From Marsh et al. (2013).

A shared limitation of Marsh et al. (2013) and the other model studies is the specified rate of injection of Na atoms into the model. Estimates of this quantity have historically varied significantly (Plane, 2012). However, Carrillo-Sánchez et al. (2016) recently constrained the total rate of meteoric mass input to 43 ± 14 t d^{-1}, with an associated Na input rate of 0.3 t d^{-1}. The simulations in Marsh et al. (2013) were driven by an Na mass input rate of just 0.035 t d^{-1} (equivalent to a total meteoric mass input rate of 4.6 t d^{-1}). This was based on the lower end of a previous estimate, nearly factor of ten smaller than the Carrillo-Sánchez et al. (2016) estimate. Li et al. (2018) reported updated WACCM Na scheme simulations, driven by the Carrillo-Sánchez et al. (2016) Meteoric Input Function (MIF). WACCM is known to underestimate the vertical transport of minor species in the MLT, because short wavelength gravity waves are not resolved on the horizontal grid scale of the model (~150 km). These sub-grid waves contribute to vertical chemical and dynamical transport of constituents while dissipating, and this can exceed transport driven along mixing ratio gradients by the turbulent eddy diffusion

produced once the waves break (Gardner et al., 2017). Because these additional vertical transport mechanisms are underestimated, the MIF of each metal needs to be divided by a specific factor in order to correctly simulate the observed *absolute* metal density (Plane et al., 2018). Notably, a factor of five reduction was found to be necessary for the Na input rate (Li et al., 2018). There is scientific interest to test this MIF scaling factor in other chemistry-climate model studies, in order to further understanding of the drivers behind the discrepancy between what is simulated and observed.

2.7 The Nitrous Oxide Layer

The wide availability of Na layer observations, as discussed in the previous section, is an exception to the general trend of there being a sparsity of chemical observations available above the mesopause (Jackson et al., 2019). The potential for an N_2O layer in the MLT is an active debate. Recent developments to satellite retrieval techniques have extended the limits of observable altitudes, potentially highlighting a new source of N_2O.

2.7.1 Surface Sources of N_2O

The major source of N_2O present in the Earth's atmosphere is from surface emissions. The primary production mechanism for this involves nitrification and denitrification bacterial processes in soil (Brasseur and Solomon, 2005). N_2O is then transported into and through the stratosphere via the Brewer-Dobson circulation (Brewer, 1949; Dobson, 1956) (see Section 2.4.1). It is well known that N_2O is a precursor to stratospheric NO_y, through reaction R2.17. As explained in Section 2.5.2, NO_y depletes ozone through the catalytic cycle shown in reactions R2.15 and R2.16 (Crutzen, 1970). Ravishankara et al. (2009) noted that N_2O is now the most important anthropogenic ozone-depleter, largely due to the success of the Montreal Protocol in reducing the emissions of the historically dominant ozone-depleters: chlorine- and bromine-containing halocarbons. N_2O is also an important greenhouse gas, with anthropogenic emissions causing a steady increase in atmospheric N_2O concentrations over the past three decades (IPCC, 2014).

2.7.2 Atmospheric Sources of N_2O

It is usually assumed that N_2O has no *in situ* atmospheric sources, although potential sources in the MLT have been identified. One reaction mechanism postulated by Zipf and Prasad (1982), based on their laboratory work, is that secondary electron impact from EEP (see Section 2.5.2) promotes N_2 to the excited triplet state

$$N_2(X^1\Sigma_g^+) + e^- \rightarrow N_2(A^3\Sigma_u^+) + e^-, \quad \text{(R2.23)}$$

where the $N_2(A^3\Sigma_u^+)$ state lies 7.63 eV above the $N_2(X^1\Sigma_g^+)$ ground state (Gillan et al., 1996). In a similar manner, reaction R2.23 can be induced by photoelectrons (energetic electrons produced by photoionisation of atmospheric species) (Nagy and Banks, 1970). This is then followed by a reaction with O_2

$$N_2(A^3\Sigma_u^+) + O_2 \rightarrow N_2O + O \quad \text{(R2.24a)}$$

to produce N_2O. The other, dominant (>70%) channel of $N_2(A^3\Sigma_u^+) + O_2$ produces ground state N_2 and atomic oxygen

$$N_2(A^3\Sigma_u^+) + O_2 \rightarrow N_2(X^1\Sigma_g^+) + 2O. \quad \text{(R2.24b)}$$

N_2O produced in the MLT would be transported down to the stratosphere through the wintertime polar vortex via seasonal mesospheric circulation (Fisher and O'Neill, 1993) (see Section 2.4.1). Enhanced descent of such N_2O would be possible after a major SSW event, particularly if the stratopause reforms at significantly higher altitudes, as has occurred several times this century (Karpechko et al., 2017), most notably during the winter of 2009 (Manney et al., 2009).

Until recently, the mechanism suggested by Zipf and Prasad (1982) was largely disregarded as there were no high-altitude observations available to verify it. However, following measurements from the Atmospheric Chemistry Experiment - Fourier Transform Spectrometer (ACE-FTS) (Bernath et al., 2005) on-board SCISAT-1 and the Michelson Interferometer for Passive Atmospheric Sounding (MIPAS) instrument (Fischer and Oelhaf, 1996) on-board Envisat, discussion of the potential for MLT production of N_2O was reopened. Using N_2O retrievals from ACE-FTS data limited to near 60 km, Semeniuk et al. (2008) argued that N_2O production

in the upper mesosphere was highly likely. The authors suggested that it could be attributed to the reaction of ground state N with NO_2

$$N(^4S) + NO_2 \rightarrow N_2O + O, \qquad \text{(R2.25)}$$

peaking at around 75 km, where both reactants are produced via MEE impact in the mesosphere. This reaction occurs only on the night-side, or in polar night, as day-side NO_2 abundances are small due to NO_2 photolysis (Funke et al., 2008). Semeniuk et al. (2008) included reaction R2.25 in the Canadian Middle Atmosphere Model (CMAM), and provided simulations that supported the satellite observations. Meanwhile, using MIPAS data limited to near 70 km, Funke et al. (2008) also suggested that the primary source of N_2O production in the MLT was likely to be reaction R2.25. However, they acknowledged the potential for a significant contribution to enhancements from the lower thermosphere via the mechanism described by Zipf and Prasad (1982).

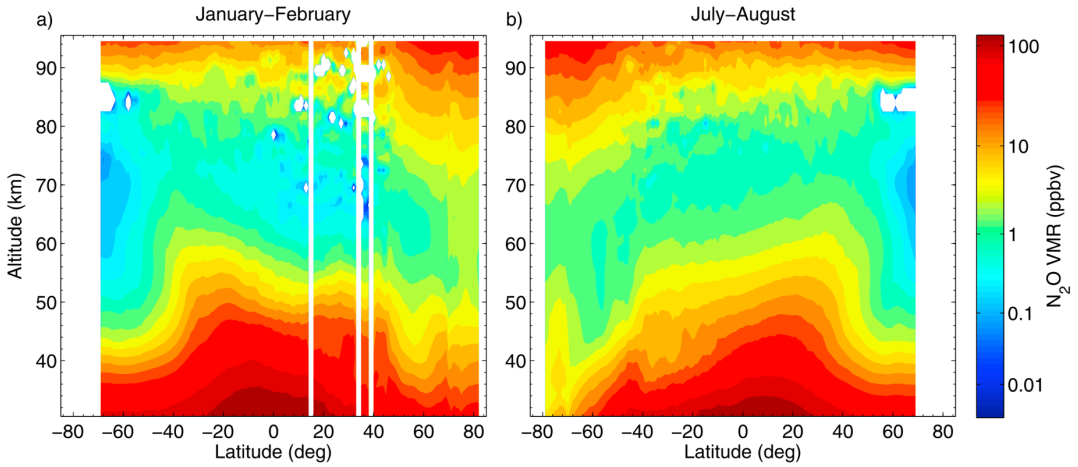

Figure 2.8 ACE-FTS N_2O climatology (ppb) for (a) January-February and (b) July-August over the 2004-2013 period. From Sheese et al. (2016).

Sheese et al. (2016) provided first measurements of what appears to be this previously overlooked source, using v3.5 of the ACE-FTS data. Compared to the data available to Semeniuk et al. (2008), the altitude limit for N_2O was increased from 60 to 94.5 km by employing less conservative micro-window sets. This data was the first of its kind to extend into the lower thermosphere, up to where the signal is close to the noise (Boone et al., 2013). Figure 2.8 shows latitudinal cross-section plots of the ACE-FTS dataset from Sheese et al. (2016). Mean N_2O volume mixing ratios (VMRs) on the order of 20-40 ppb were reported for the polar winters near 94.5 km, decreasing to

10-20 ppb at low latitudes. Note that the large VMRs do in fact correspond to small N_2O concentrations of ~10^5 molecules cm^{-3} compared to typical near-surface N_2O concentrations of ~10^{13} molecules cm^{-3}. So far, there have been no corroborating observations to confirm this discovery and, prior to Kelly et al. (2018) (the basis of Chapter 6), reaction R2.24a had not been included in any chemistry-climate model.

2.8 Summary

A combination of physical and chemical properties make the MLT an incredibly varied region of the atmosphere. Molecules, atoms and ions all coexist, each representing a significant fraction of the total composition. The chemistry of the MLT is dominated by O, produced primarily via the photolysis of O_2 (Mlynczak and Hunt, 2015). An abundance of O enables the formation of layered phenomena such as atomic metal layers (Plane et al., 2015) and facilitates the heating of the region through exothermic chemical reactions (Marsh et al., 2007). The mean transport circulation of the MLT is driven by the upwards propagation of tropospheric waves. Upwelling of mesospheric air occurs over the summertime pole, with meridional motions towards the wintertime pole where air eventually descends (Vincent, 2015). Unlike the lower atmosphere, bulk motion does not provide a complete representation of transport in the MLT. A process called diffusive separation occurs above 100 km, providing vertical transport of individual compounds based on their relative mass (Brasseur and Solomon, 2005).

The atomic Na layer is the most well-studied of all atomic metal layers. Metal input is sourced from the ablation of meteors in the Earth's atmosphere, with a recent estimate of the Na input rate being 0.3 t d^{-1} (Carrillo-Sánchez et al., 2016). The Na layer peaks at around 90 km, below which the chemistry is largely neutral, resulting in $NaHCO_3$. Ion-molecule chemistry dominates above the peak, producing Na^+. The long chemical lifetime (Xu and Smith, 2003) and strong temperature dependency (Plane, 2003) of the Na layer lend to its use as a tracer of transport in the MLT. Na is well-observed by lidar and satellite instruments (e.g. States and Gardner (1999), Fussen et al. (2010)), Na^+ has been observed by rocket sounding experiments (e.g. (Kopp, 1997)), but it is not possible to directly observe other Na compounds (Plane, 2015). Previous model studies of the Na layer have not been coupled to global chemistry-climate models (e.g. McNeil et al. (1995), Plane (2004) and Xu and Smith

(2004)), aside from more recent WACCM studies, based on the Na scheme of Marsh et al. (2013). Marsh et al. (2013) originally managed to replicate the observed global distribution and seasonal variation of Na, using an estimate of the injection rate that was around ten times lower than the Carrillo-Sánchez et al. (2016) estimate. Li et al. (2018) reported updated WACCM simulations using the revised MIF, but found a factor of five reduction in the input rate of Na was now necessary, attributable to known model deficiencies in the vertical transport of minor species in the MLT. Understanding of the drivers behind the discrepancy between what is simulated and observed may be furthered by testing this MIF scaling factor in other chemistry-climate model studies.

Space weather impacts (notably solar UV radiation and EPP) cause the production of ozone-depleting radicals HO_x and NO_y in the MLT, primarily through the dissociation of H_2O and N_2, respectively. The *in situ* destruction of mesospheric ozone has been attributed to HO_x produced in this way (Andersson et al., 2014). Meanwhile, NO_y-enriched mesospheric air may be brought down into the stratosphere through a polar vortex under certain dynamical conditions, following which stratospheric ozone depletion has been reported (Funke et al., 2005). N_2O is another precursor to NO_y, but it is usually assumed that N_2O has no *in situ* atmospheric sources. However, satellite observations of N_2O enhancements at around 70 km (Funke et al., 2008; Semeniuk et al., 2008) and more recently at around 95 km (Sheese et al., 2016) have challenged this assumption. The inclusion of a likely N_2O production mechanism in chemistry-climate model simulations can assess the feasibility of an N_2O layer in the MLT.

3 MODELS AND OBSERVATIONS

3.1 Introduction

Simulations from mathematical models of the Sun-to-Earth system are an essential tool for scientific research and operational forecasting alike. Models are used to understand the processes behind the current conditions of our environment, as well as make informed predictions of both past and future environmental conditions. For example, solar flare models have been used to estimate historical magnetic fluxes based on sunspot number records (Aulanier et al., 2012), weather models are central to any modern meteorological forecast e.g. Rawlins et al. (2007) and climate models are used to project future climate change scenarios e.g. Eyring et al. (2016). However, to be useful, models require reliable observations to compare against. Observations of the mesosphere lower-thermosphere (MLT) can be made from the Earth's surface by lidar, directly in the Earth's atmosphere through rocket sounding and from space via satellite instruments.

In this chapter, I discuss the models and observations that are used and developed in Chapters 4, 5 and 6. Section 3.2.1 provides an overview of the Met Office Unified Model and the development programme set to convert it into a model of the whole atmosphere. Brief descriptions of the other models are provided in the subsequent subsections of Section 3.2 and in Section 3.3, followed by the observations in Section 3.4. The most important details from the chapter are summarised in Section 3.5.

3.2 Models

3.2.1 UM and Extended UM

The Unified Model (UM) (Cullen, 1993; Walters et al., 2019) and the Extended UM (Griffith et al., 2020) are versions of the combined weather forecasting and climate model developed by the UK Met Office. The UM provides a detailed representation of the global atmosphere with its dynamical core (based on the fully compressible, non-hydrostatic Euler equations (Wood et al., 2014)) combined with parametrisations of various physical processes. The non-hydrostatic dynamical core of the UM

distinguishes it from many other atmospheric models, as the hydrostatic approximation is commonly used by models to simplify the treatment of momentum in the vertical direction. It assumes that the most important vertical forces acting on a parcel of air are the vertical pressure gradient and gravity. Some phenomena, such as sound waves, are overlooked by this assumption (Brasseur and Solomon, 2005). Furthermore, the hydrostatic approximation breaks down with large vertical accelerations, as exist in the thermosphere, potentially making it less suitable for whole atmosphere modelling applications compared to non-hydrostatic formulations (Jackson et al., 2019). A notable feature of the output from a non-hydrostatic model is that the vertical grid is on altitude levels instead of pressure levels, as seen in hydrostatic model output.

A framework exists to couple the UM to models of other terrestrial components, such as the ocean (Storkey et al., 2018), land surface (Harper et al., 2018) and atmospheric chemistry (Archibald et al., 2019) (described in Section 3.2.2). Simulations of the coupled model, known as the UK Earth System Model (UKESM) (Sellar et al., 2019), are used to investigate the response of the Earth's climate to future pollutant emission scenarios and land use changes. Climate configurations of the UM have a maximum model lid height of 85 km (Walters et al., 2019) (cutting-off in the upper-mesosphere). The Extended UM (directly building on the existing formulation of the UM) is the product of an initiative to raise this lid into the thermosphere (Jackson et al., 2019).

Harry (2015) made the first documented attempt to run the UM with a vertical extension, testing 100 km and 120 km ceilings. These runs could not progress without intensifying the 'sponge layer' (for the restraining of vertical motions) via the model's vertical wave damping coefficient. The specific cause of the problem was left unknown, until it was revisited by Griffith et al. (2020). In their study, Griffith et al. (2020) tested the UM at model lid heights of 100 km, 120 km and 135 km. As with Harry (2015), attempts to run the Extended UM before upgrading any physics parametrisations resulted in significant model instabilities that led to frequent crashes and anomalous output. Crashes were largely triggered by errors associated with the model 'halos'. When the UM is run in parallel on a high performance computer, divisions of the model domain are spread across multiple computational processors. Each processor can only access a specific horizontal square of the model domain. Model halos refer to an interpolation applied across the surrounding grid points, used

to allow for advection between processors. Excessive wind speeds generated over the poles were found to extend beyond the limits of their halo. The authors diagnosed the breakdown of the Local Thermodynamic Equilibrium (LTE) assumption validity in the MLT as the cause of the problem.

Measures were imposed in subsequent Extended UM simulations to avoid this issue. Firstly, the halo size and the vertical wave damping coefficient were both increased. Secondly, a treatment of temperature forcing was applied from 70 km upwards. The temperature forcing works as follows. When applied, both shortwave and longwave radiation are switched off. The forcing then incrementally 'pushes' the UM temperature field towards the globally and temporally invariant climatological profile shown in Figure 3.1, based on data from the US Standard Atmosphere (USSA) (COESA, 1976), the Committee of Space Research (COSPAR) International Reference Atmosphere (CIRA) (Fleming et al., 1990) and a specified exobase temperature of 1000 K. The forcing acts over a relaxation timescale of 24 hours, as to preserve some of the internal influence of model dynamics on air temperature (Griffith et al., 2020). A fixed vertical resolution of 3 km was applied to the additional levels above the original 85 km lid. This thickness was optimised to provide the best possible representation of fine scale features without causing additional model instabilities. Griffith et al. (2020) found that the model was more susceptible to crashing with increasing lid height, so adjusted the vertical wave damping coefficient accordingly. A version of the Extended UM with non-LTE (NLTE) implementation has recently been developed. This has reduced the extent to which the model relies on artificial temperature forcing, maintaining

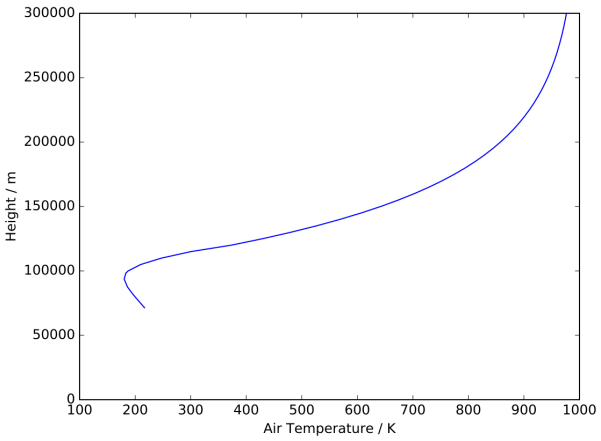

Figure 3.1 Climatological temperature profile, used for forcing in Extended UM simulations. Based on (70-86 km) the US Standard Atmosphere (USSA) (COESA, 1976); (86-119.7 km) the Committee on Space Research (COSPAR) International Reference Atmosphere (CIRA) (Fleming et al., 1990); and (>119.7 km) asymptotic treatment towards exobase temperature of 1000 K. From Griffith et al. (2020).

stability with a longer relaxation timescale of 35 hours and without the need for any forcing between 70 and 90 km whatsoever. Hence, this enables a more realistic seasonal temperature variation to be simulated in this region.

Table 3.1 Properties of the Extended UM vs. the standard release UM.

Configuration/ variant	Standard	Extended
Model lid height	85 km	120 km
Number of levels	85	100
Temperature forcing above	n/a	90 km
Vertical damping coefficient	0.05	0.25
Radiation scheme	LTE	NLTE

In Chapter 4, the Extended UM with NLTE implementation is used as the base model for the coupled chemistry. The 120 km altitude lid configuration (containing 100 altitude levels) was selected for this purpose based on an assessment of the benefits of additional levels against the drawbacks of larger instabilities. All simulations reported from this model configuration have a horizontal resolution of 1.25° (latitude) × 1.875° (longitude). The key differences between this particular version of the Extended UM and the standard release UM, from which it is derived, are summarised in Table 3.1.

At the time of writing, the Extended UM remains an active Met Office development project with ongoing preparation of additional physics processes. The next step will be the inclusion of eddy diffusion, an important process for chemical transport in the MLT (Brasseur and Solomon, 2005). Following this, molecular viscosity and molecular diffusion are due to be added. This will be necessary for the stability of further increments to the altitude of the Extended UM model lid, as the importance of molecular physics on wave amplitude regulation above 150 km was highlighted by ray-tracing experiments conducted in Griffin and Thuburn (2018).

3.2.2 UKCA

UK Chemistry and Aerosols (UKCA) (Archibald et al., 2019; Morgenstern et al., 2009; Mulcahy et al., 2018; O'Connor et al., 2014) is a community framework led by the Met Office and the UK National Centre for Atmospheric Science (NCAS) that converts the UM into a chemistry-climate model. The UKCA scheme simulates atmospheric composition on a global scale by connecting aerosol and gas phase chemistry in the troposphere and stratosphere (Archibald et al., 2019). The key aim of UKCA is to support climate and environmental change research. Different configurations of UKCA exist, enabling detail to be either added or removed from a particular region or process. For example, the StratTrop configuration provides a detailed representation of both stratospheric and tropospheric chemistry (O'Connor et al., 2014), the (lesser-used) Strat configuration contains detailed stratospheric chemistry with simplified tropospheric chemistry (Morgenstern et al., 2009) and GLOMAP mode provides a focused description of aerosol processes (Mulcahy et al., 2018). Figure 3.2 shows a plot from an example study, where UM-UKCA simulations are used to model future changes in the tropical ozone (O_3) column. The 11-year ensemble mean is shown to predict a return of the ozone column to 1980s values by around 2040 and to 1960s values close to the mid-century (Keeble et al., 2017).

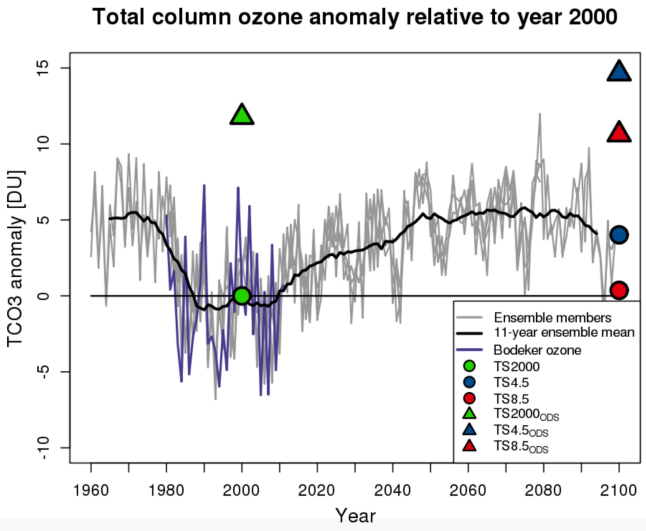

Figure 3.2 Total-column ozone anomalies from year-2000 conditions over the tropics, projected to 2100 by UM-UKCA ensemble simulations. From Keeble et al. (2017).

In Chapter 4, UKCA is used to provide the Extended UM with neutral chemistry developments in the MLT. Representation of upper atmospheric chemistry will enable top-down impacts on stratospheric ozone to be directly simulated, potentially improving the accuracy of UM-UKCA projections, such as the example in Figure 3.2. The UKCA Strat scheme is selected as a template for this work, instead of the more

widely used StratTrop scheme. This is because the highly detailed tropospheric representation in StratTrop makes it unnecessarily computationally expensive for simulations focused on the MLT. In the Strat scheme, O_2, N_2 and CO_2 are treated as uniform, while the excited species $O(^1D)$ is calculated via a steady-state approximation. There were no branches of the Strat UKCA code available at UM version 11.3 (required for compatibility with the Extended UM), so it was necessary to upgrade the most recent Strat scheme code branch available (provided by Olaf Morgenstern). Further technical details on this are included in the Appendix.

3.2.3 WACCM and WACCM-X

The Whole Atmosphere Community Climate Model (WACCM) (Garcia et al., 2007; Gettelman et al., 2019; Marsh et al., 2013) and WACCM with thermosphere and ionosphere eXtension (WACCM-X) (Liu et al., 2018; Liu et al., 2010) are both advanced models provided by the US National Center for Atmospheric Research (NCAR). WACCM is a global atmosphere model that includes fully interactive neutral and ion chemistry, covering altitudes from the Earth's surface to the lower thermosphere, extending to a model lid of 5.96×10^{-6} hPa (~140km). Unlike the UM, WACCM has a finite-volume dynamical core requiring the hydrostatic approximation. Vertical resolution in the MLT is ½ a scale height (3-4 km) (Feng et al., 2013) and the default Prandtl number for the production of turbulence from breaking gravity waves is 4. It is part of the Community Earth System Model (CESM) (Danabasoglu et al., 2020; Hurrell et al., 2013), which has the primary aim of understanding and predicting the behaviour of the Earth's climate. WACCM-X contains an added representation of the thermospheric physics occurring above the vertical limit of WACCM, extending further to a model lid of 4.1×10^{-10} hPa (typically 500-700 km, varying by solar and geomagnetic activity). It was built to study the sensitivity of the upper atmosphere to solar and magnetospheric inputs and understand connections to the lower atmosphere (Liu et al., 2010). Figure 3.3 presents a plot from an example study, where WACCM-X was used to simulate the atmosphere-ionosphere response to the 21st August 2017 solar eclipse. The temporary lack of photolysis is shown to result in a significant depletion of atomic oxygen (O) with a corresponding enhancement of ozone (McInerney et al., 2018). The study also reports signatures of the lower atmospheric dynamical response to the eclipse in the upper

atmosphere. This demonstrates the important detail that can be sought from fully-coupled, whole atmosphere models.

In Chapter 4, the prescription of upper-boundary conditions for selected variables in the Extended UM-UKCA is considered, based on data from a standard WACCM-X simulation. This data is available with registration through the NCAR Climate Data Gateway: https://www.earthsystemgrid.org/dataset/ucar.cgd.ccsm4.f.e20.FXSD.f19_f19.001.atm.hist.monthly_ave.html.

In Chapter 5, simulations with a new Extended UM-UKCA atomic sodium (Na) scheme are compared to the free-running WACCM simulation reported in Li et al. (2018). This was based on the model configuration of Mills et al. (2016), augmented with the Na scheme described in Marsh et al. (2013). Horizontal resolution was set to 1.9° (latitude) × 2.5° (longitude), while this particular configuration contained 70 altitude levels, extending to the default model lid (~140 km). The Prandtl number was set equal to 2, as recommended by Garcia et al. (2014).

In Chapter 6, model simulations are performed using a specified dynamics version of WACCM. The configuration described in Kinnison et al. (2007) is modified with a novel source of nitrous oxide (N_2O) production in the MLT. The horizontal resolution,

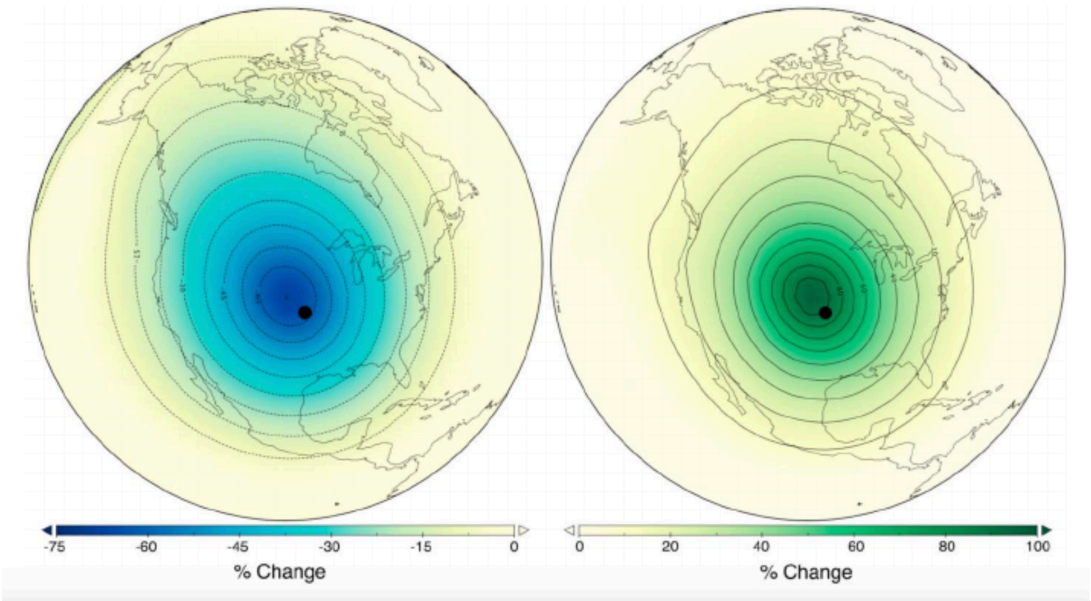

Figure 3.3 WACCM-X simulated impact of 21st August 2017 solar eclipse on atomic oxygen (left) and ozone (right) at 65 km, 1800 UT, over North America. From McInerney et al. (2018).

model lid pressure and Prandtl number are unchanged from the WACCM simulations used in Chapter 5. This WACCM configuration does, however, contain 88 altitude levels.

3.2.4 GLOW

Global Airglow (GLOW) (Solomon, 2017) is another model provided by NCAR. It is a single-column, single-time model operating between altitudes of 80 and ~600 km, designed to simulate upper atmospheric light emissions at discrete wavelengths caused by the relaxation of excited chemical constituents. When run repeatedly over horizontal space and through time, it can be used to generate a 3D time series (Solomon, 2017). The required input parameters for GLOW include Ap index and F10.7 (solar flux at 10.7 cm). Figure 3.4 shows example GLOW output, where model simulations have been used to derive thermospheric O composition. The WACCM simulations in Chapter 6 are driven by GLOW input to provide the photoelectron-induced production rate of excited triplet state molecular nitrogen, $N_2(A^3\Sigma_u^+)$, over 2013. Ap indices and F10.7 data were taken from the National Oceanic and Atmospheric Administration (NOAA) database and are accessible through: ftp://ftp.ngdc.noaa.gov/STP/GEOMAGNETIC_DATA/INDICES/KP_AP ftp://ftp.swpc.noaa.gov/pub/weekly/RecentIndices.txt.

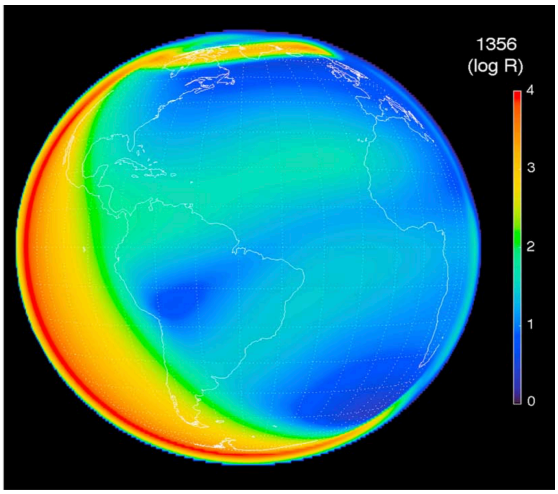

Figure 3.4 Global distribution of emissions at 135.6 nm from atomic oxygen in the $O(^5S)$ doublet state, generated by GLOW, based on general circulation model output. Snapshot at 0000 UT, over the Atlantic. From Solomon (2017).

3.3 Empirical Models

3.3.1 MSIS

Mass Spectrometer Incoherent Scatter (MSIS) (Hedin et al., 1977; Picone et al., 2002) is an empirical model of the whole atmosphere developed by the US Naval Research Laboratory (NRL). It generates a global distribution of atmospheric composition, total

mass density and temperature based on mass spectrometry measurements from various satellite instruments and rocket probes, as well as incoherent scatter measurements (Nisbet, 1967) from a collection of ground-based stations. The incoherent scatter method works by measuring light backscattered from the free electrons in the ionosphere (Gordon, 1958). MSIS combines and integrates these observations to provide an estimation of the above parameters from ground to exobase (near 500 km (Solomon and Roble, 2015)) with complete horizontal coverage. In Chapter 4, MSIS output for temperature, O and atomic hydrogen (H) is used in comparisons with Extended UM-UKCA and WACCM-X output.

3.4 Observations

3.4.1 SCIAMACHY

SCanning Imaging Absorption SpectroMeter for Atmospheric CHartographY (SCIAMACHY) was an instrument on-board the ESA EnviSat satellite, operational between 2002 and 2012. It took measurements within the wavelength range of 240-2380 nm, initially probing the atmosphere between altitudes of 5-100 km (Burrows et al., 1995), before the altitude limit was reduced to 93 km in late 2003. SCIAMACHY derived atmospheric composition via three different viewing geometries: limb, nadir and occultation. Each of these are depicted in Figure 3.5. The overall objective of SCIAMACHY was to investigate global atmospheric change, with a particular focus on tropospheric pollution and stratospheric ozone depleting substances (Bovensmann et al., 1999). It also had the capability to retrieve atomic Na from limb measurements, which are used in Chapter 5. Extended UM-UKCA and WACCM simulations of the atomic Na layer distribution are compared to SCIAMACHY data.

3.4.2 GOMOS

Global Ozone Monitoring by Occultation of Stars (GOMOS) (Kyrölä et al., 2004) was another instrument on-board EnviSat. Measurements were made within the wavelength range of 245-942 nm via the stellar occultation technique. This works by replicating the solar occultation geometry shown in Figure 3.5, but with the incident light provided by stars instead of the Sun. The principal aim of GOMOS was to record the stratospheric ozone distribution to a high degree of accuracy, however it also monitored other trace gases, aerosols and temperature, within a maximum altitude

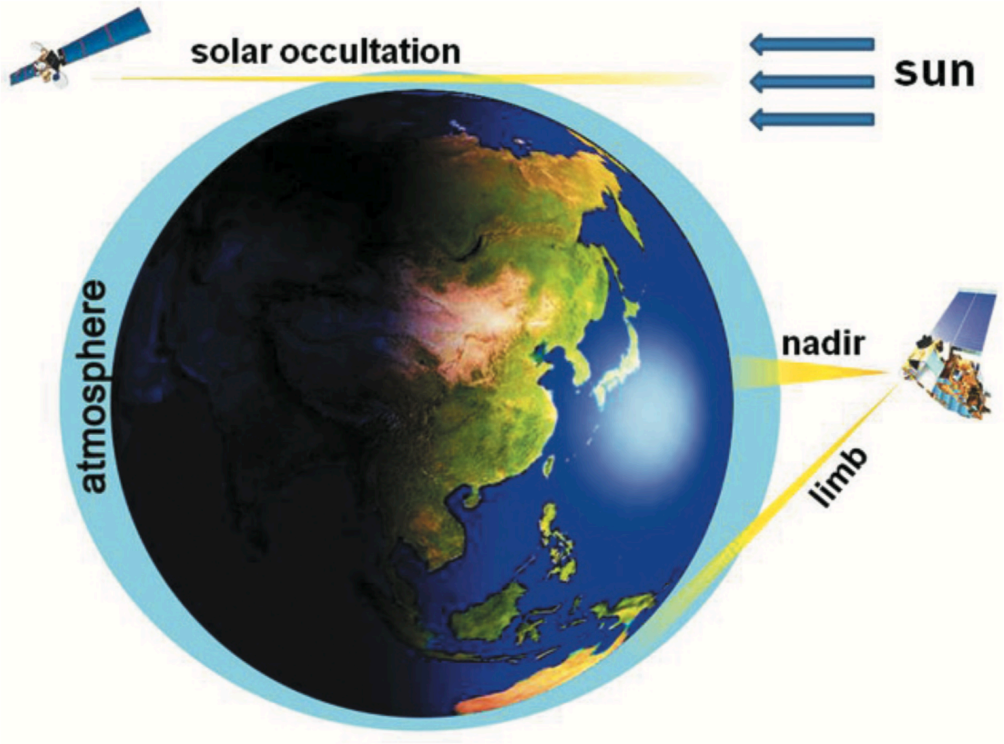

Figure 3.5 Schematic of observational geometries from different satellite measurement techniques. Shown are solar occultation and limb viewing (horizontal), and nadir viewing (vertical). From Lee et al. (2009).

range of 5-250 km (Bertaux et al., 2004). In this remit, GOMOS also provided observations of atomic Na, which are used in Chapter 5.

3.4.3 OSIRIS

Optical Spectrograph and Infra-Red Imager System (OSIRIS) (Llewellyn et al., 2003) is equipment on-board the Swedish Odin satellite, operational since 2001. Via two separate instruments, it measures radiance profiles of the Earth's limb (geometry shown in Figure 3.5). A UV-visible spectrograph works between the wavelength range of 280-800 nm, while an infrared imager observes through three different wavelength channels: 1.53, 1.27 and 1.26 μm. Combined, OSIRIS covers altitudes of 10-100 km, deriving minor species altitude profiles from terrestrial absorption features and detecting airglow in the MLT (Llewellyn et al., 2004). The primary purpose of OSIRIS is to provide a better understanding of the mechanisms responsible for stratospheric ozone depletion, although it was also designed to study mesospheric chemistry (Llewellyn et al., 2003). Atomic Na retrievals from OSIRIS are used in Chapter 5, alongside equivalent data from GOMOS and SCIAMACHY.

3.4.4 SABER

Sounding of the Atmosphere using Broadband Emission Radiometry (SABER) (Russell III et al., 1999) is an instrument on-board the NASA Thermosphere-Ionosphere-Mesosphere Energetics and Dynamics (TIMED) satellite, operational since 2001. It works by measuring emissions of the Earth's limb (Figure 3.5) akin to OSIRIS, but in the infrared wavelength range of 1-17 μm (Esplin et al., 1994). The mission was designed to provide a focused investigation of the chemical composition, temperature variation and key emission features of the atmosphere between altitudes of 60-180 km (Mlynczak, 1997). In Chapter 4, SABER observations of temperature, O and H are used alongside MSIS data for Extended UM-UKCA performance testing.

3.4.5 ACE-FTS

Atmospheric Chemistry Experiment – Fourier Transform Spectrometer (ACE-FTS) is the main payload on-board the Canadian satellite SCISAT-1, operational since 2003. It works primarily in solar occultation (geometry shown in Figure 3.5) (Bernath et al., 2005). ACE-FTS operates in the near-infrared wavelength range of 2.2-13.3 μm, typically covering altitudes of 10-100 km. Similar to many of the other instruments discussed in this section, a particular focus of ACE-FTS is to further understanding of ozone-related processes. However, it is also designed to study connections between atmospheric chemistry and climate change. A key limitation of ACE-FTS is that measurements can only be made at sunrise and sunset. The orbit of SCISAT-1 enables a maximum of 32 occultation events per day (Boone et al., 2013), resulting in a relatively sparse spatial coverage. However, this is compensated by the high signal-to-noise ratio of the instrument, allowing a

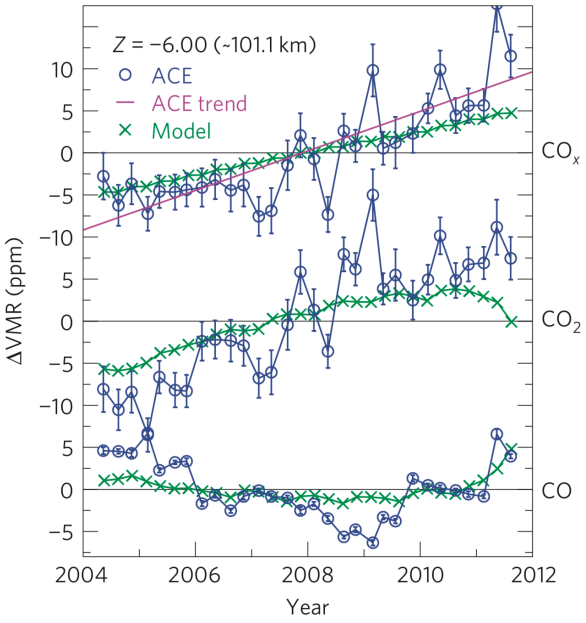

Figure 3.6 Increasing VMR residuals of carbon dioxide in the lower thermosphere (~101 km), calculated from ACE-FTS observations. From Emmert et al. (2012).

comprehensive list of chemical retrievals to be made. At processing version 3.5 of the data, retrievals are available for 36 different molecules, 21 subsidiary isotopologues (molecules of shared chemical formula but different neutron number) and high altitude carbon dioxide (CO_2) (Boone et al., 2013). Figure 3.6 shows a plot from an example study, where ACE-FTS data was used to investigate CO_2 trends in the lower thermosphere. The study reported a rate of CO_2 increase that was about 10 ppm per decade faster than what was predicted by an atmospheric model. In this thesis, the work reported in Chapter 6 was motivated by ACE-FTS observations of N_2O in a similar region, published in Sheese et al. (2016).

3.4.6 Rocket Data

Data from numerous historical rocket sounding campaigns is used in Chapter 5 to provide observations of Na^+ (ionised atomic Na). The dataset contains measurements from a non-uniform selection of locations, dates and times, but is fairly large. Given this, I made the decision to use all available data and apply statistical treatments to it.

Table 3.2 Description of the campaigns that provided rocket data used in Chapter 5.

Campaign	Location	Reference
Noctilucent Clouds Perseids	Kiruna (Sweden)	(Kopp et al., 1985)
Cold Arctic Mesopause Project	Kiruna (Sweden)	(Kopp et al., 1984)
Perseids Meteor Shower	Wallops Island (Virginia, USA)	(Herrmann et al., 1978; Kopp, 1997)
Winter Anomaly Campaign	Wallops Island (Virginia, USA)	(Grebowsky et al., 1998)
International Solar Eclipse Campaign	Red Lake (Canada)	(Kopp, 1997; Kopp and Herrmann, 1984)
European Energy Budget Campaign	Kiruna (Sweden)	(Kopp, 1997; Kopp et al., 1985; Offermann, 1985; Offermann et al., 1981)

Contributing campaigns are listed in Table 3.2 and include launches from Kiruna (Sweden), Wallops Island (Virginia, USA) and Red Lake (Canada) that occurred

between 1976 and 1982. In Chapter 5, the arithmetic mean, geometric mean and median of the individual profiles compiled from this dataset are used to infer a consensus for the observed Na^+ profile.

3.5 Summary

The UM is a climate and forecasting model developed by the Met Office. It forms the basis of the Extended UM, the product of an initiative to raise the UM model lid into the thermosphere (Jackson et al., 2019). The current, best available version of the Extended UM has its model lid height set to 120 km and contains an NLTE radiation scheme. However, it requires temperature to be forced towards a globally and temporally invariant climatological profile from above 90 km in order to maintain model stability. It is this Extended UM version that is used as the starting point in this thesis for coupling to a chemistry scheme. The Strat scheme of UKCA is used as a template for this purpose, with associated neutral chemistry developments for the MLT reported in Chapter 4.

WACCM is a global atmosphere model developed by NCAR that already includes fully interactive neutral and ion chemistry, covering all altitudes from the Earth's surface to the lower thermosphere (~140 km). The Extended UM differs to WACCM in its dynamical formation. The Extended UM has a fully compressible non-hydrostatic dynamical core, whereas WACCM has a finite-volume dynamical core working under the hydrostatic approximation. The hydrostatic approximation breaks down with large vertical accelerations as exist in the thermosphere, potentially making non-hydrostatic formulations preferable in the upper atmosphere (Jackson et al., 2019). For this reason, the Extended UM may be better suited for whole atmosphere modelling applications than WACCM, especially when future versions with more detailed descriptions of physics are released. However, WACCM is currently the most comprehensive tool available for studying chemistry and transport in the MLT in a whole atmosphere setting. Therefore, WACCM is used in Chapter 6 to support an explanation for uncorroborated observations of N_2O production in the MLT.

Model performance after each development step reported in this thesis is evaluated against the best available corresponding observations. Observations from various instruments and methods are used, including satellite measurements made from the

limb, nadir and occultation geometries; as well as rocket sounding measurements from a range of campaigns. Reliable observations provide an essential resource for effective model development, as is shown in Chapters 4 and 5, while models can also be a valuable tool to provide physical reasoning for otherwise unexplained observations, as is shown in Chapter 6.

4 COUPLED CHEMISTRY FOR THE EXTENDED UNIFIED MODEL

4.1 Introduction

Through my co-authorship of a commentary paper on the future directions of whole atmosphere modelling (see Jackson et al. (2019)), I contribute towards the discussion on building blocks for chemistry in whole atmosphere models. In this chapter, I use the conclusions from the publication to guide the development of chemistry in the UK Chemistry and Aerosols (UKCA) framework for the Met Office Extended Unified Model (Extended UM). Opening efforts have been directed towards neutral chemistry in the Mesosphere-Lower Thermosphere (MLT). Atomic oxygen (O) and atomic hydrogen (H) are the major influencers on the aeronomy of this region (Mlynczak and Hunt, 2015). It is therefore critical for a coupled chemistry-climate model of the whole atmosphere to accurately simulate their abundances. This requires adequate representation of chemistry and radiation above the stratopause, where the majority of far-UV (FUV) and extreme-UV (EUV) radiation is absorbed.

This chapter reports the first vertical extension phase of the UKCA coupled Extended UM (Extended UM-UKCA), with a focus on the methods used to generate realistic magnitudes of O and H. In this instance, an intermediate model lid height of 120 km altitude is specified. Significant technical work is required to enable compatibility between UKCA and the Extended UM. This includes the transformation of all 3D UKCA input files from the original 85-level (85 km lid) vertical grid to the extended 100-level (120 km lid) vertical grid, as well as a myriad of model specific changes. In the interest of brevity, an overview of the modifications necessary to recreate the basic version of the Extended UM-UKCA that is used as the starting point in this chapter is provided in the Appendix.

Section 4.2 reports work completed to generate a realistic global mean temperature profile in the MLT. Section 4.3 documents the inclusion of shorter wavelength photolysis for the key reactions relevant to O and H production. Section 4.4 considers the prescription of upper boundary conditions for both O and H, to account for the

processes occurring above the 120 km lid. With this, the first estimates of Extended UM-UKCA chemical heating rates are made in Section 4.5, representing the largest source of heating in the MLT (Marsh et al., 2007). The key results from the testing completed in this chapter are summarised in Section 4.6.

4.2 Temperature

Many of the chemical reactions in the MLT display a strong temperature dependence. In order for the resulting rates of such reactions to be realistic in the Extended UM-UKCA, atmospheric temperature must be suitably constrained. As referenced in Chapter 3, the Extended UM configuration that I am building upon has its temperature field forced to a fixed climatological profile in the thermosphere. Before any chemistry developments take place, it is necessary to first evaluate the suitability of this treatment by comparing the model temperature output against observations.

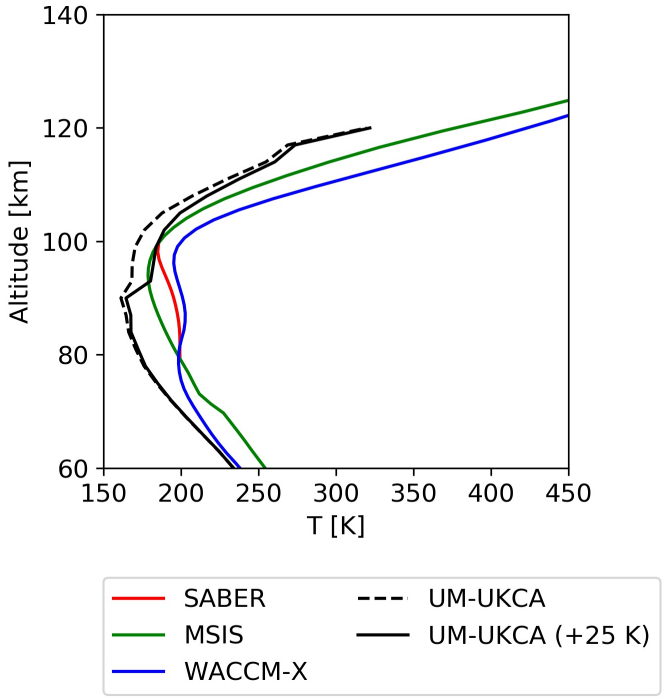

Figure 4.1 Zonal mean, meridional mean for range 80°S-80°N, annual mean altitude profiles of atmospheric temperature (K). Profiles include (dashed black) UM-UKCA without temperature adjustment, (solid black) UM-UKCA with temperature adjustment, (solid red) SABER observations, (solid green) MSIS data and (solid blue) WACCM-X data.

Figure 4.1 shows the temperature profile of the MLT for the Extended UM-UKCA in its unmodified state, alongside corresponding satellite data from the Sounding of the Atmosphere using Broadband Emission Radiometry (SABER) instrument (Russell III et al., 1999), empirical model data from Mass Spectrometer Incoherent Scatter (MSIS) (Hedin et al., 1977; Picone et al., 2002) and reference model data from the Whole Atmosphere Community Climate Model with thermosphere and ionosphere extension (WACCM-X) (Liu et al., 2018; Liu et al., 2010). Upwards of about 75 km, the UKCA

profile begins to fall below MSIS and WACCM-X. This is a result of the model containing no treatment of chemical heating (Mlynczak and Solomon, 1993). To address this, the temperature forcing (as described in Section 3.2.1) comes into effect at altitudes above 90 km. A stepped increase at this height is clearly visible in the UKCA profile, but it is not significant enough to guide the profile towards the reference values. Another key feature of this plot is the disagreement between WACCM-X and the observations above about 100 km. Since MSIS and SABER corroborate each other, the MSIS data will be used as the target reference profile in the lower thermosphere, rather than the WACCM-X data. It should be anticipated that this temperature difference will cause a similar disparity between WACCM-X and the observations in the subsequent chemistry sections, particularly when converting constituent mixing ratios to atmospheric number densities.

In order to get the Extended UM-UKCA to better replicate the now-established temperature reference profile, I tuned the forcing code to apply an additional 25 K increment. The profile containing this change, also shown in Figure 4.1, eliminates the temperature deficit previously generated around the mesopause. Between 90 and 100 km, UM-UKCA (+25 K) is within ±3 K of MSIS. Note that below 90 km, where no forcing is applied, the difference between UM-UKCA (+25 K) and MSIS is still up to ±25 K. Meanwhile, above 100 km, where the applied forcing becomes increasingly less effective with altitude, a maximum offset of ±60 K is seen at the very top of the model domain. It should be stressed that by definition, the fixed temperature profile used for the forcing contains no horizontal variation. Hence, it is only designed to be an interim measure until the Extended UM radiation scheme is coupled to UKCA.

4.3 Photolysis

The standard treatment of photolysis in regular 85-km-lid UM-UKCA simulations is split into two vertical domains. For altitudes below 20 hPa (around 25 km), online photolysis rates calculated through the Fast-JX package (Bian and Prather, 2002; Wild et al., 2000) are used exclusively. Fast-JX is effective down to the lower wavelength limit of 177 nm, which is not suitable to represent all of the important reactions in the upper stratosphere and lower mesosphere. Hence for altitudes above 20 hPa / 25 km, Fast-JX rates are merged with rates generated from offline stratospheric lookup tables

with a lower wavelength limit of 112 nm (Lary and Pyle, 1991; Morgenstern et al., 2009). Unsurprisingly, the Extended UM-UKCA requires photolysis rates to be calculated down to even shorter wavelengths, specifically the EUV and soft x-ray bands (reaching 10 and 0.4 nm respectively) (Jackson et al., 2019). At the time of writing, the Met Office are developing a new unified photolysis and photoionisation scheme for the whole atmosphere that will be effective down to 0.4 nm. However, this scheme was not available during my research period. As an alternative, I was provided with extended offline photolysis and photoionisation rates as a function of pressure and solar zenith angle.

Since the chemistry of the MLT is dominated by O, it is essential to generate realistic concentrations of both the ground state $O(^3P)$ and the first electronic excited state $O(^1D)$. Table 4.1 lists the O production and destruction channels that were either extended or added to the Extended UM-UKCA.

Table 4.1 Oxygen photolysis and photoionisation reactions that were either extended to lower wavelength bands or newly added.

Reaction		Note	
	$O_2 + h\nu \rightarrow O(^3P) + O(^3P)$	Extension	(R4.01)
	$O_2 + h\nu \rightarrow O(^1D) + O(^3P)$	Extension	(R4.02)
	$O(^3P) + h\nu \rightarrow O^+(^4S) + e^-$	New	(R4.03)
	$O(^3P) + h\nu \rightarrow O^+(^2D) + e^-$	New	(R4.04)
	$O(^3P) + h\nu \rightarrow O^+(^2P) + e^-$	New	(R4.05)
	$O(^3P) + h\nu \rightarrow O^+(^4P^e) + e^-$	New	(R4.06)
	$O(^3P) + h\nu \rightarrow O^+(^2P^e) + e^-$	New	(R4.07)

The principal source of O in the MLT is the photolysis of molecular oxygen (O_2) (R4.01 and R4.02), mainly in the Schumann-Runge continuum, the Schumann-Runge bands and at Lyman-α (121.6 nm) (Mlynczak and Hunt, 2015). Both reactions are also important in the stratosphere and were therefore already present in UKCA. Maintaining the existing online Fast-JX treatment of their photolysis was preferable in the stratosphere. However, the extended offline rates would be needed in the MLT. I set the section of the UKCA code that controls photolysis to switch off Fast-JX for reactions R4.01 and R4.02 at model levels above a selected pressure. Instead, it would

calculate new rates based on the extended offline rates via a linear interpolation over pressure and solar zenith angle for each level and horizontal point, every model time-step. This treatment came into effect above 0.01 hPa (around 70 km) to provide a smooth transition into the new regime.

The additional production of O in the MLT needed to be balanced by appropriate destruction mechanisms. I added five O photoionisation channels to UKCA (R4.03-4.07) where, in each, the resulting O ion constitutes a different electronic state. Since I am not developing an ion chemistry scheme, the various new ions needed to be accounted for to avoid an indefinite build up. To achieve this I added a constant volume mixing ratio (VMR) tracer that could be set as the product in place of each O ion. It did not matter that this violated oxygen conservation, as O_2 is not advected and is itself a constant tracer calculated as a function of atmospheric density. In effect, this provides an unlimited excess of O_2. Another O destruction mechanism missing in UKCA is the recombination back to O_2

$$O(^3P) + O(^3P) \rightarrow O_2. \qquad \text{(R4.08)}$$

With the inclusion of reaction R4.08, I had a suitable treatment of atomic oxygen in the MLT.

The second most important constituent to the chemistry of the MLT is H. Table 4.2 lists the H production channels that had their treatment of photolysis developed for the Extended UM-UKCA.

Table 4.2 Water vapour photolysis reactions that were either extended to lower wavelength bands or newly added.

Reaction		Note	
	$H_2O + h\nu \rightarrow OH + H$	Extension	(R4.09)
	$H_2O + h\nu \rightarrow O(^1D) + H_2$	New	(R4.10)
	$H_2O + h\nu \rightarrow O(^3P) + 2H$	New	(R4.11)

The largest source of H is the photolysis of water vapour (H_2O) (R4.09-4.11) at Lyman-α (Mlynczak and Solomon, 1993). Additional destruction mechanisms were not required, as the majority of H loss occurs through reactions with O_2, HO_2, NO_2

and O_3 that all pre-exist in the chemistry scheme. A photolysis extension was applied to reaction R4.09 and reactions R4.10 and R4.11 were newly added, through the same method as used for O.

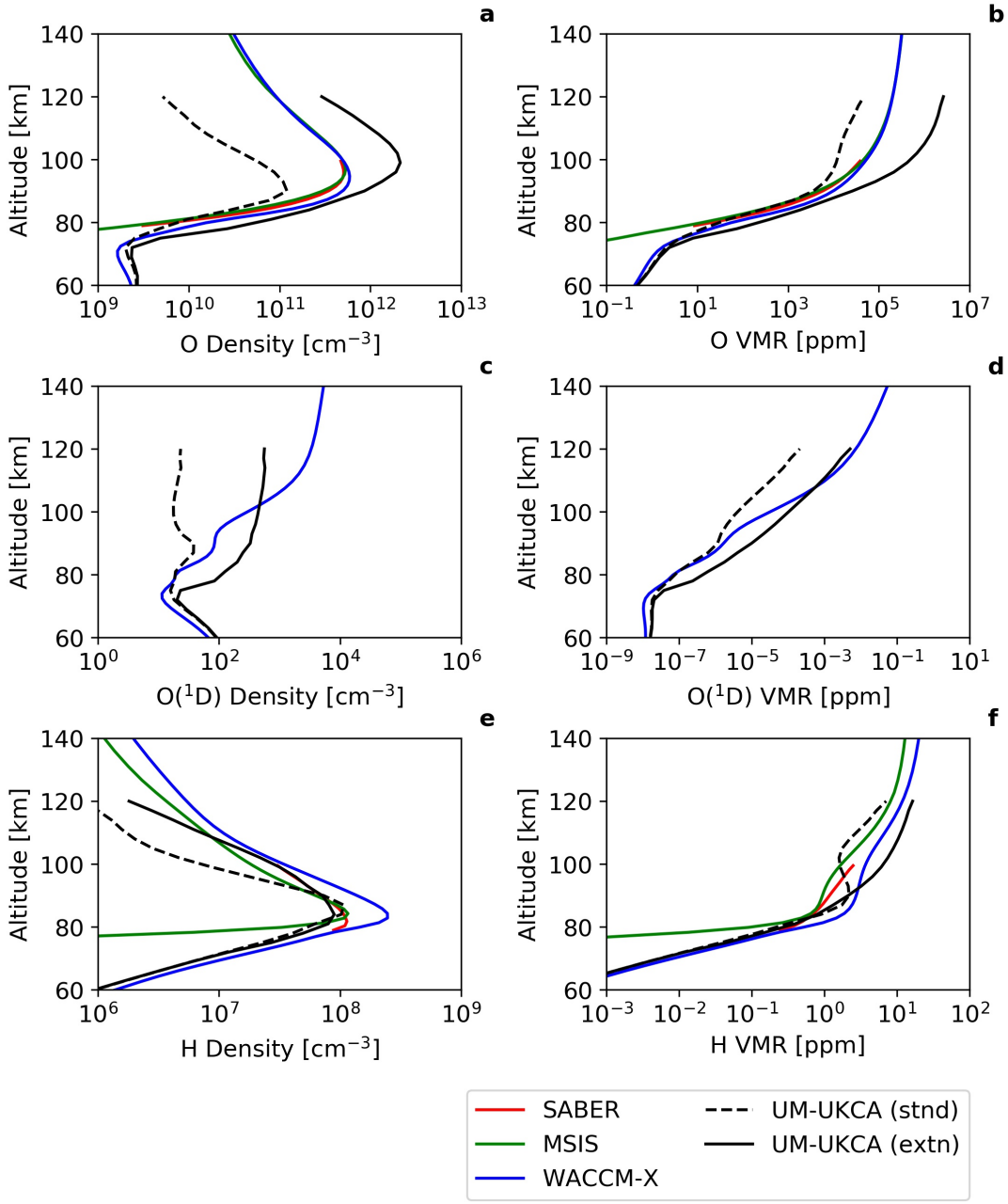

Figure 4.2 Zonal mean, meridional mean for range 80°S-80°N, annual mean altitude profiles of (a, b) ground state atomic oxygen, O, (c, d) first electronic excited state atomic oxygen, O(^{1}D) and (e, f) atomic hydrogen, H, as number densities (cm^{-3}, left) and VMRs (ppm, right). Profiles are (dashed black) UM-UKCA without photolysis extension, (solid black) UM-UKCA with photolysis extension, (solid red) SABER observations, (solid green) MSIS data and (solid blue) WACCM-X data.

Figure 4.2 shows altitude profiles of O, O(^{1}D) and H from simulations with and without the photolysis developments, alongside equivalent profiles from satellite data

and empirical model data (where available) as well as reference model data. Panels (a) and (b) display corroboration between the SABER, MSIS and WACCM-X O reference profiles throughout the MLT, replicated by both Extended UM-UKCA simulations up to the original model lid height (85 km). Above this, the unchanged Extended UM-UKCA simulation (stnd) falls just under a factor of ten short of the reference (×9.2 at 100 km, in VMR); and the Extended UM-UKCA simulation with photolysis developments (extn) falls above the reference by a similar factor (×9.5 at 100 km, in VMR). The O deficit simulated in the UKCA (stnd) run is expected, given the previously explained underrepresentation of O_2 photolysis in the MLT. However, the extent of the O excess in the UKCA (extn) run is perhaps surprising. Conversely, the response of $O(^1D)$ and H to the photolysis developments is generally good over all altitudes. In panel (e), $O(^1D)$ shows a marked improvement in its replication of the equivalent WACCM-X profile in VMR, yielding a near-perfect agreement between the models above 100 km. The UM-UKCA (extn) profile of H in panel (f) also better matches the reference above 85 km, where the UM-UKCA (stnd) profile begins to deviate. However, it should be noted that WACCM-X appears to overestimate the H VMR compared to the observations by a factor of 2-3 between 80 and 100 km. UM-UKCA (extn) overestimates this further, suggesting that both models could have minor issues in the treatment of H in this region.

A particularly noticeable discrepancy in Figure 4.2 is the apparent underestimation of UM-UKCA tracers plotted in number density compared to VMR above about 95 km, most noticeable in panels (c) and (e). I conclude that this is attributable to the temperature offset discussed in Section 4.2, hence the VMR profiles are best suited for assessing the performance of chemistry alone. However, the UM-UKCA (extn) VMR profile in Figure 4.2b highlights a separate model anomaly. Above 100 km, O VMRs are greater than 1, which is unphysical. This result is derived from O mass mixing ratios (MMRs) from the original model output, which are also greater than 1. It is highly likely that this is a feature of O_2 being treated as uniform in UKCA (see Section 3.2.2). This means any O_2 that is removed is effectively immediately restored, while any products of the removal process (e.g. O) are maintained – a violation of mass conservation. Although this is a reasonable approximation in the homosphere, where densities of N_2 and O_2 by far outweigh all other chemical species (see Section 2.2), it is clearly causing issues in the heterosphere.

Based on this analysis of Figure 4.2, it is clear that the next priority is to investigate all other factors that may contribute to the excess of O produced by UM-UKCA (extn) in the MLT. Naturally, evaluating the new O_2 photolysis rates (the key change made) is the logical place start. Monthly mean photolysis rates for UM-UKCA (extn) and WACCM are compared as fixed altitude horizontal slices in Figure 4.3 and as altitude profiles in Figure 4.4. For simplicity, the UM-UKCA rates were calculated offline directly from the list of extended rates for the purpose of these plots. Averaged over each month, solar zenith angle was projected onto a latitude-longitude grid with a 3-hourly time-step, before the corresponding photolysis rates were attached to their relevant locations. The temporal resolution of this method can be seen in panels (a) and (b) of Figure 4.3 as a pattern of eight longitudinal waves.

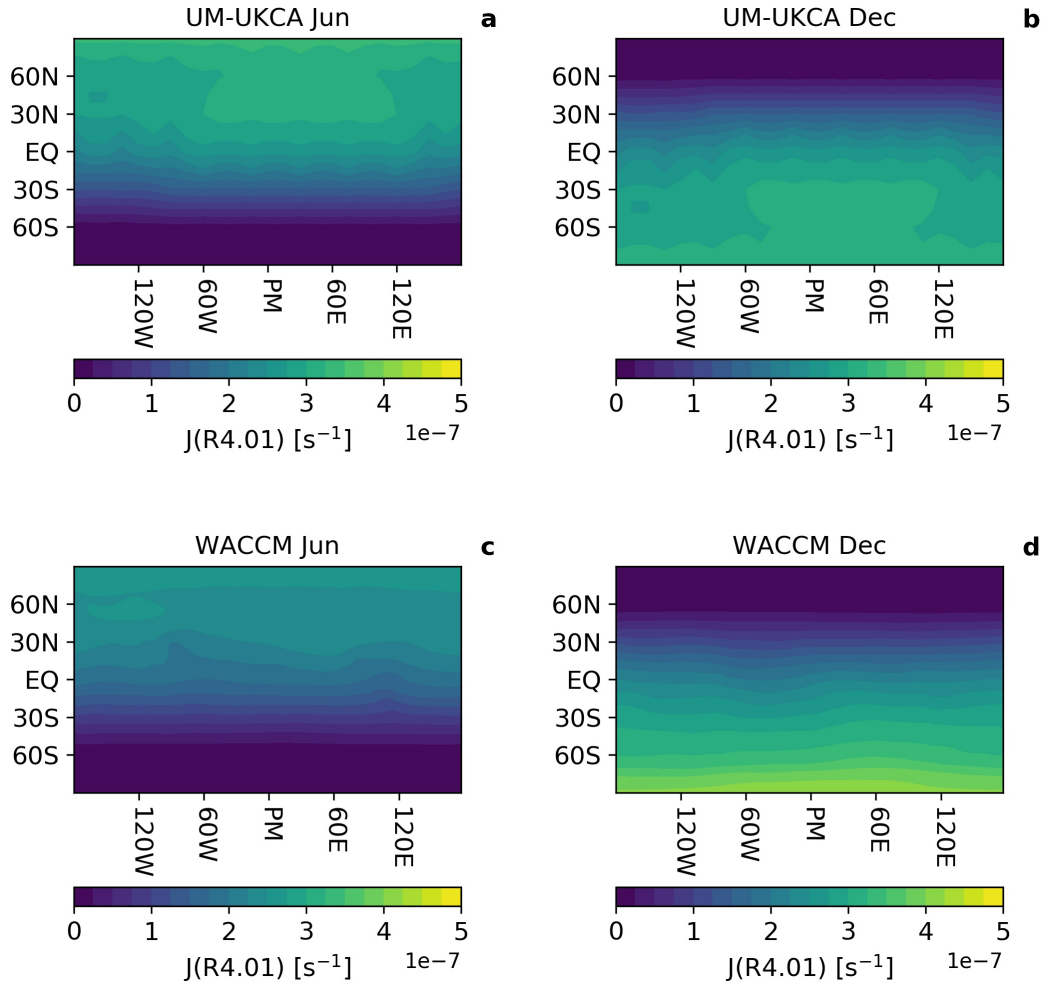

Figure 4.3 Horizontal distributions of monthly mean O_2 photolysis rates (s^{-1}) through channel R4.01 at an altitude slice of 100 km for (a, b) UM-UKCA with photolysis extension (input) and (c, d) WACCM (output). Includes June mean (left) and December mean (right).

It is clear from Figure 4.3 that O_2 photolysis in the Extended UM-UKCA is of a similar magnitude and follows the same seasonal distribution to that of WACCM. Therefore, the relative factor ten VMR enhancement of O in the MLT, seen in Figure 4.2b, is not attributable to a discrepancy in photolysis rates. Nevertheless, there do appear to be smaller differences in the photolysis rates between the models, which should be quantified. Comparing the June rates (Figures 4.3a and 4.3c), UM-UKCA records a greater maximum magnitude than WACCM in the summer hemisphere, with the peak region extending over a larger area. Conversely, the December rates in Figures 4.3b and 4.3d show WACCM to have the highest maximum magnitude. However, such rates are limited to latitudes above about 80°S, suggesting that the overall O_2 photolysis rates in UKCA are still larger than in WACCM.

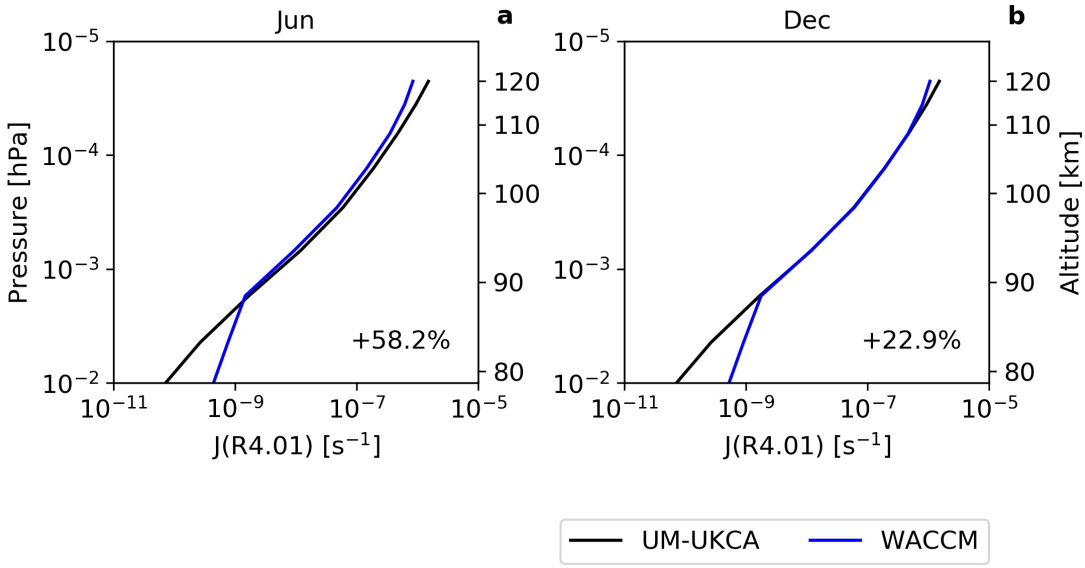

Figure 4.4 Global mean altitude profiles of O_2 photolysis rates (s^{-1}) through channel R4.01 for (a) June mean and (b) December mean. Profiles are (black) UM-UKCA with photolysis extension and (blue) WACCM-X.

The altitude profiles in Figure 4.4 provide a globally averaged picture of the difference in photolysis rates between the Extended UM-UKCA and WACCM. On the log scale, the rates progress very closely between about 90 and 110 km in June (Figure 4.4a) and are virtually indistinguishable in December (Figure 4.4b). The offset seen between the models below this region is large in relative terms, but very small (over 1000 times) in absolute terms compared to the rates seen when approaching 120 km. Therefore, such offset will not make any noticeable impact on the overall rate. Above 110 km, the Extended UM-UKCA rates are up to a factor of two larger than WACCM, so perhaps an O excess of a similar magnitude should be expected here. When the

global mean photolysis rates are averaged over the pressure level range used by the photolysis extension (the y-axis of Figure 4.4), a single figure to represent the overall rate of photolysis in the MLT is generated for each model. As predicted, UKCA yields a higher result than the WACCM, with UKCA-to-WACCM percentage differences of +58.2% and +22.9% for June and December respectively (annotated). From the analysis of Figures 4.3 and 4.4, I conclude that the extended offline photolysis rates provide a reasonable estimate for reaction R4.01 in the MLT, which are on average slightly faster compared to WACCM, weighted towards the highest model levels.

Next, I consider the instantaneous horizontal distribution of O in the Extended UM-UKCA to assess how the global factor ten discrepancy varies spatially at given snapshots. Figure 4.5 shows UT midday snapshots for the summer and winter solstices at 100 km, comparing UKCA to WACCM-X. The most noticeable feature of panels

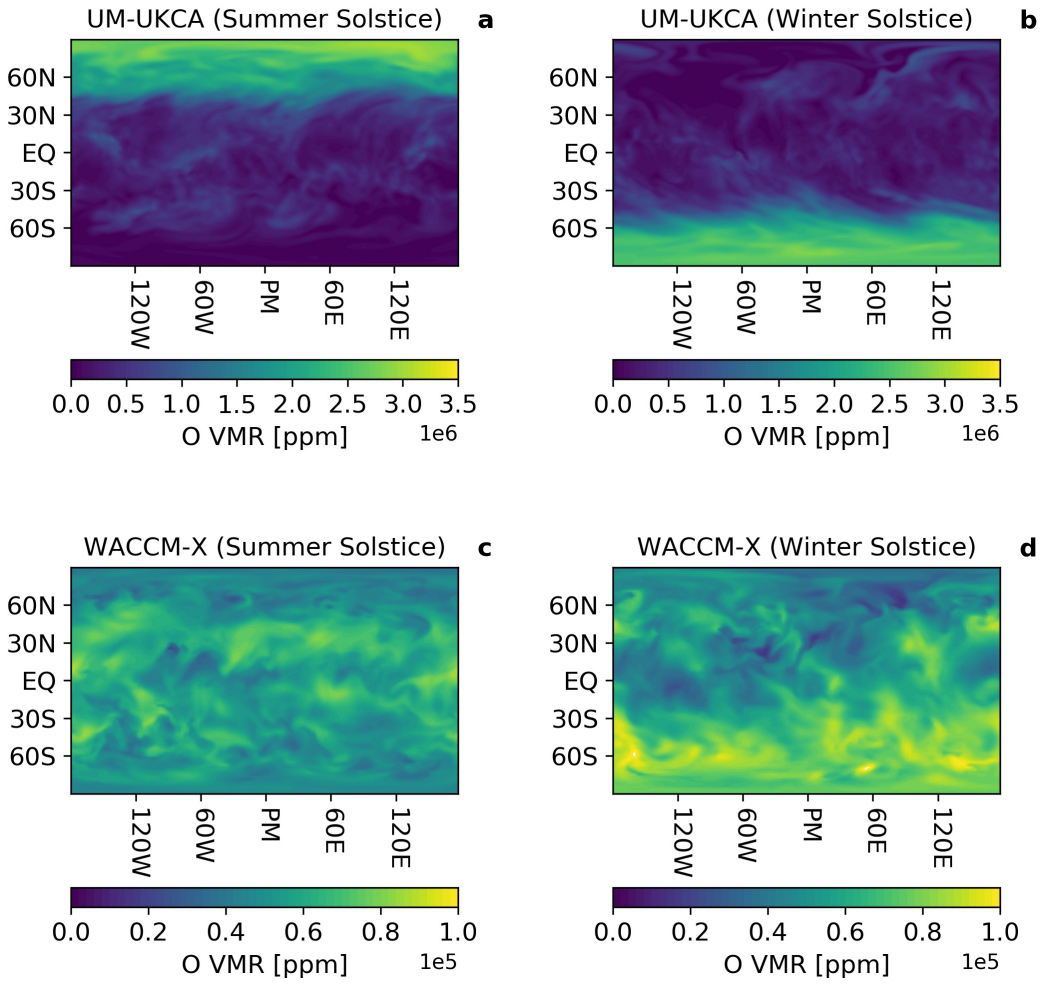

Figure 4.5 Horizontal distributions of instantaneous O VMR (ppm) at an altitude slice of 100 km for (a, b) UM-UKCA with photolysis extension and (c, d) WACCM-X. The panels show 12:00 UT snapshots for the summer solstice (left) and the winter solstice (right).

(a) and (b) is the accumulation of O in the polar regions of the respective summer hemispheres. Poleward of about 75°, UKCA simulated O is on average the most abundant constituent of the atmosphere, once again showing the previously discussed VMR anomaly, while typical ratios simulated outside of these regions are of the order 10^5 ppm. Since O is long-lived at high altitude (typical lifetime of approximately 1 year at 105 km (Friederich et al., 1999)), it is subject to transport through the MLT. A significant build-up over the summer pole is not consistent with typical mesospheric circulation, where downwelling occurs over the winter pole (Smith et al., 2011). This result provides an early warning into the performance of constituent transport in the

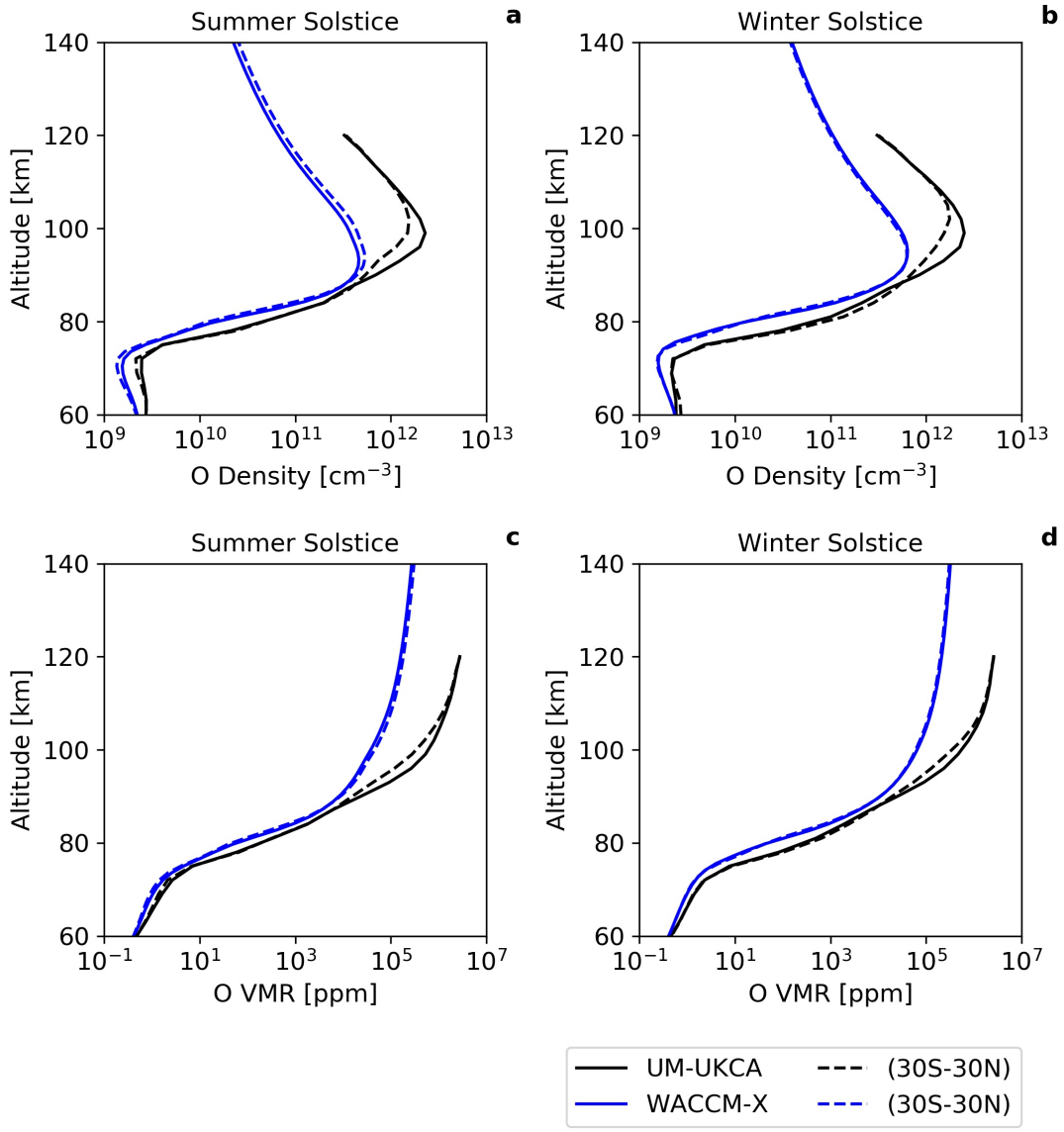

Figure 4.6 Altitude profiles of O in (a, b) number density (cm^{-3}) and (c, d) VMR (ppm) from (black) UM-UKCA with photolysis extension from (solid) global mean and (dashed) 30°S-30°N mean; (blue) WACCM-X from (solid) global mean and (dashed) 30°S-30°N mean. Includes 12:00 UT snapshots for summer solstice (left) and winter solstice (right).

Extended UM-UKCA. No such stark polar variation is simulated by WACCM-X, with panel (c) displaying a well-mixed horizontal O distribution for the June solstice and panel (d) displaying only a slight positive bias to the polar region of the summer hemisphere for the December solstice. It would therefore appear that the polar accumulation in the Extended UM-UKCA is an unphysical artefact. To explore this in a quantitative manner, the data from Figure 4.5 is plotted as O altitude profiles in Figure 4.6.

Figure 4.6 includes instantaneous global means, alongside profiles limited to just the tropics (30°S-30°N) to remove the impact of the polar accumulation seen in UKCA. Inter-model percentage offset calculations reveal a maximum relative improvement in model agreement near 95 km at the reduced latitude range. Here, an improvement of 67.3% is recorded for the summer solstice, while a similar value of 70.2% is recorded for the winter solstice. This means that when the area of O accumulation is excluded from consideration, the relative excess of O simulated in UKCA compared to WACCM-X is cut by over two thirds. Such a significant factor provides a strong case for insufficient Extended UM-UKCA transport in the MLT being a key cause of the simulated O surplus.

Future configurations of the Extended UM will contain physics developments, such as the inclusion of eddy diffusion, molecular viscosity and molecular diffusion. This will enable more realistic chemical transport (Brasseur and Solomon, 2005), hopefully addressing the contribution of dynamics to the O build-up issue. Therefore, given that the extended O_2 photolysis rates appear to be reasonable, it would be inappropriate to artificially lower them to counteract a separate problem. Instead, it seems more reasonable to acknowledge this issue and attempt to validate the performance of O chemistry in the model in relative terms. One way to do this is to analyse the temperature dependence of the given tracer over the region of interest (e.g. Stolarski et al. (2012)). In this case, I measure the correlation of O VMR with temperature near the mesopause and compare the results to WACCM-X. Figure 4.7 displays the resulting correlation plots, produced separately for various latitude ranges. For each plot, I calculate the Pearson correlation coefficient

$$\rho(x, y) = \frac{\mathrm{cov}(x, y)}{\sigma_x \cdot \sigma_y}, \qquad \text{(E4.01)}$$

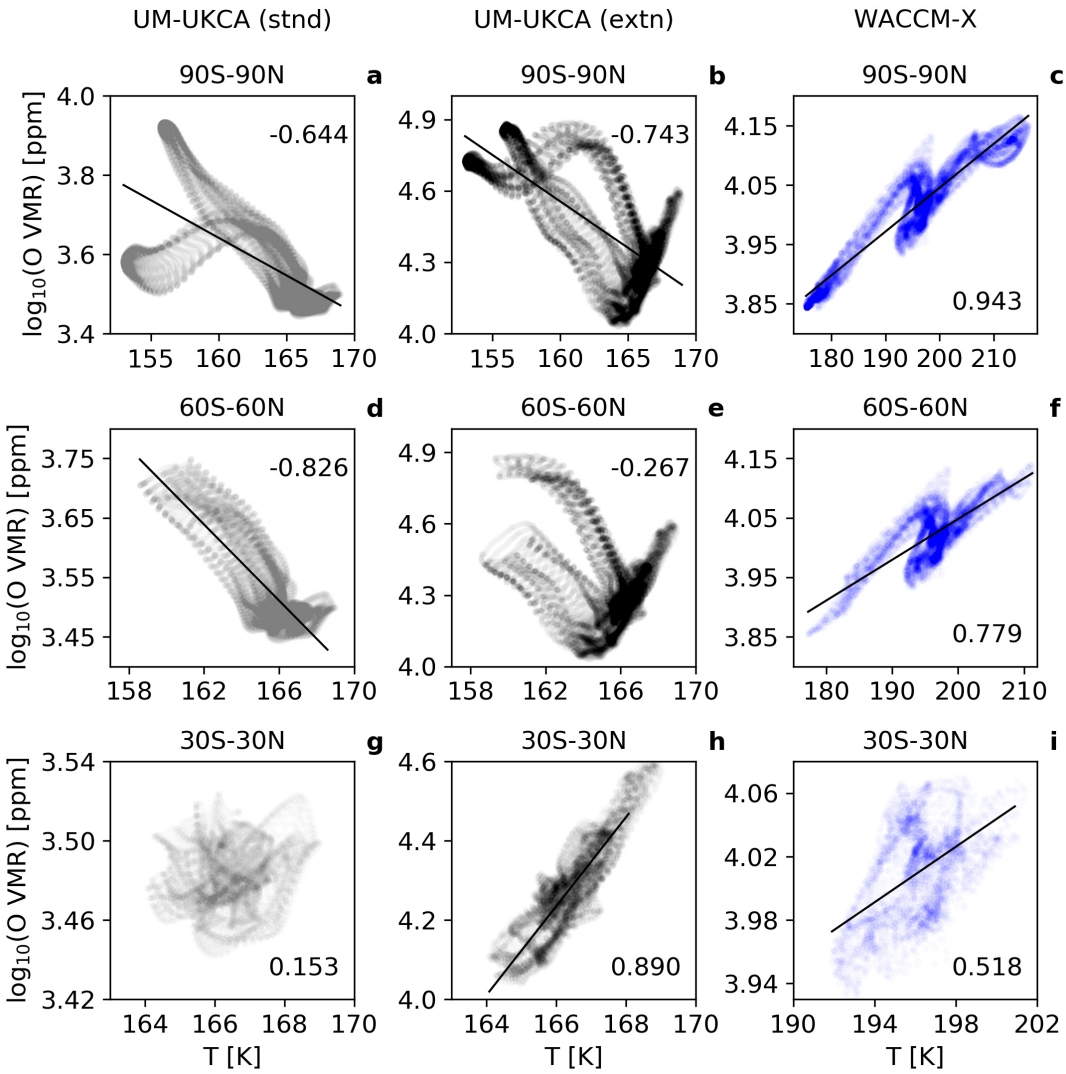

Figure 4.7 Correlation plots of the logarithm of O VMR (ppm) versus temperature (K) made from annual mean horizontal grid data at 90 km for (left column) UM-UKCA without photolysis extension, (middle column) UM-UKCA with photolysis extension and (right column) WACCM-X. Analysis split into latitude bands of (top row) global, (middle row) 60°S-60°N and (bottom row) 30°S-30°N. Pearson correlation coefficients annotated inside subplots. Linear regressions conduced for Pearson correlation coefficients of magnitude greater than 0.5. Note different axis ranges.

where x is temperature, y is $\log_{10}$(O VMR), cov(x, y) is the covariance and σ_x and σ_y are the standard deviations of x and y respectively. For the plots that showed an appreciable correlation, defined by a Pearson coefficient of magnitude greater than 0.5, I calculate a linear regression and include the corresponding line of best fit. WACCM-X (Figures 4.7c, 4.7f and 4.7i) shows a consistent linear positive correlation, with the Pearson coefficient declining as the latitude range is refined, but remaining above 0.5. This suggests that O magnitudes increase with temperature.

Elsewhere, the unchanged Extended UM-UKCA simulation (stnd, Figures 4.7a, 4.7d and 4.7g) shows negative or no correlation through each latitude domain. The Extended UM-UKCA simulation with photolysis developments (extn, Figures 4.7b, 4.7e and 4.7h) presents a similar result in the wider latitude ranges, however a structure with strong positive correlation of 0.890 is resolved between 30°S and 30°N. It is clear that the grid points responsible for the apparent negative correlation in the global domain are all located outside of the tropics. Therefore, such data is subject to the previously identified O accumulation issue. This provides one indication that independent of what is a likely transport deficiency in the Extended UM, Extended UM-UKCA O chemistry appears to perform as expected compared to WACCM-X. However, it should be noted that the temperature ranges of the UM-UKCA plots in Figure 4.7 do not overlap those of the corresponding WACCM-X plots, which are approximately 30 K warmer. Additionally, each positive correlation in the UM-UKCA data is seen at the high-temperature end of the plots. Therefore, any conclusions made about the chemistry contain the caveat that positive correlations may also be a feature of a warmer background atmosphere.

4.4 Upper-Boundary Conditions

The inclusion of an extended photolysis treatment improves the performance of Extended UM-UKCA chemistry in the MLT. However, realistic distributions of O and H cannot necessarily be expected in the top few altitude levels of the model below the 120 km lid. Firstly, tracer accumulation may arise close to the model lid before the atmosphere is truncated. Secondly, the physical and chemical processes occurring

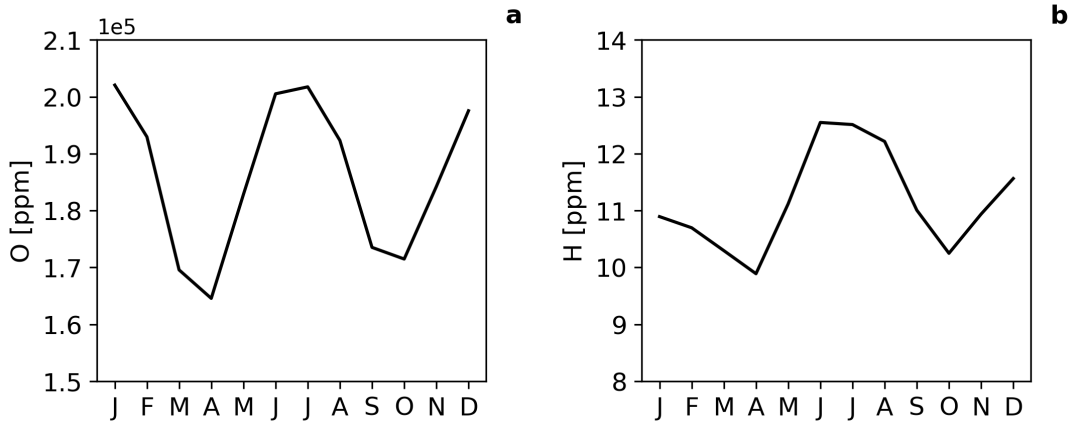

Figure 4.8 2003-2013 (one 11-year solar cycle period) monthly mean time series at 120 km for (a) O and (b) H VMRs (ppm) from WACCM-X data.

above this limit are not accounted for and may have a significant impact lower down in the atmosphere. It is therefore necessary to consider prescribing the top level of the O and H tracer fields to an external source of data. In turn, this should also guide the next few levels below to more realistic values.

Data from both MSIS and WACCM-X are available for upper-boundary conditions. However, it is apparent from Figure 4.2b that the magnitude of the offset between the two data sources at 120 km, for O, is by far outweighed by their collective offset to the Extended UM-UKCA at the same altitude. Here, a very small WACCM-X-to-MSIS VMR offset factor of ×1.01 is yielded, while UKCA is around a factor of 13 larger than both sources. Clearly, the Extended UM-UKCA is not currently in a position to be used to assess whether MSIS or WACCM-X offers the better top-level treatment. At this development stage, the priority is instead to establish the most suitable way to impose upper-boundaries in UKCA from any reasonable source of

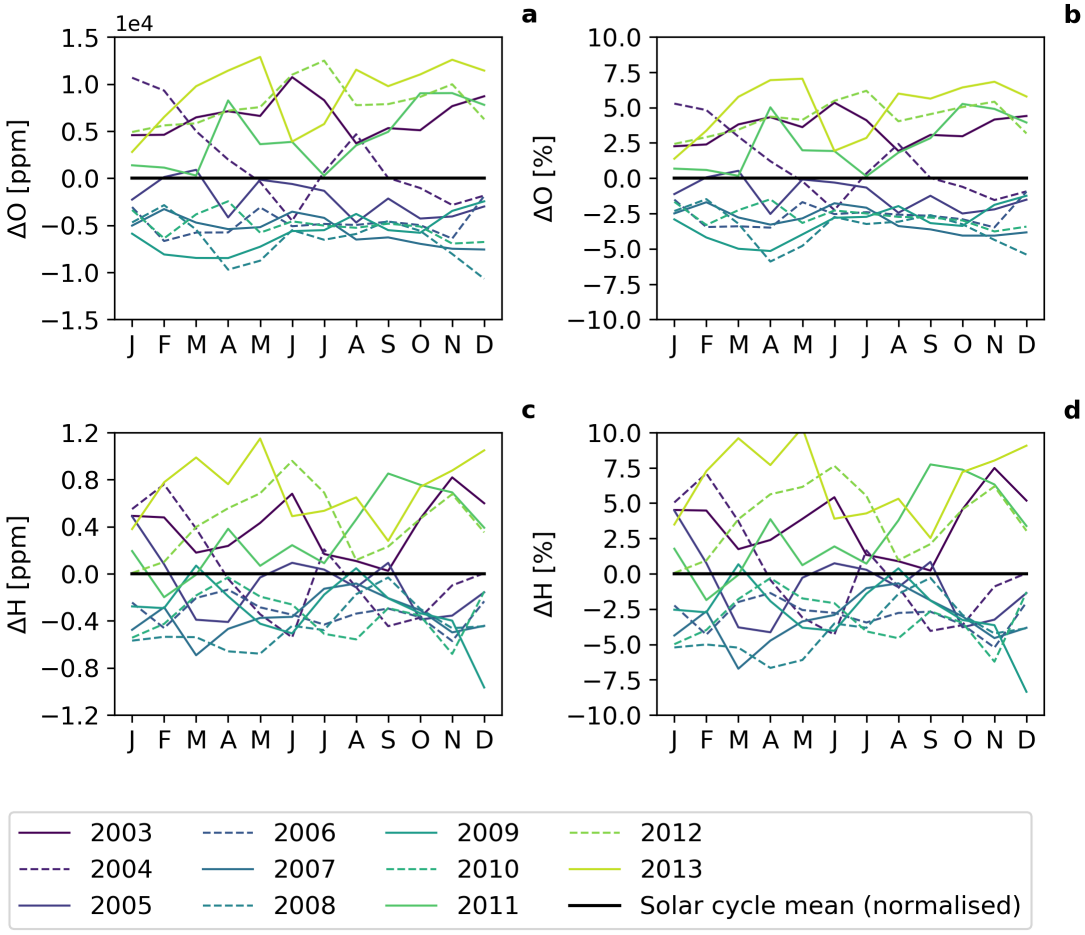

Figure 4.9 Normalised 11-year solar cycle monthly mean time series baseline at 120 km (black) with absolute (ppm, left) and percentage (right) differences plotted for the individual years in the period, for (a, b) O and (c, d) H from WACCM-X data.

data. Hence, in the following discussion, I only evaluate the case for prescribing WACCM-X data as upper-boundary conditions for O and H, independently.

Given the important role that solar activity has in determining the composition of the thermosphere (Solomon and Roble, 2015), it is necessary to consider the variation of O and H over the 11-year solar cycle period. For this purpose, I retrieved data from a long-term WACCM-X simulation (Liu et al., 2018). I used this to analyse the extent to which the data varies seasonally and annually, relative to the offset in the corresponding Extended UM-UKCA fields. Firstly, I calculated the mean O and H VMRs at 120 km for each month, averaged across one solar cycle period in the WACCM-X data. From this, I constructed the time series shown in Figure 4.8. Figure 4.8 extracts the same seasonal variation in both species, with maximum VMRs occurring at each solstice and minimum VMRs occurring at each equinox. This time series can be considered a seasonal baseline for the period. Secondly, I normalised the seasonal baseline, enabling the deviations of individual years from the collective monthly means to be assessed. This was done by subtracting the monthly mean O and H VMRs from the baseline for each year. Figure 4.9 displays the resulting time series in terms of both absolute (ppm) and relative (%) differences. There appears to be no month exhibiting significantly more solar cycle variation than any other for either species. April and May are arguably the most variable months and July and August the least, although this is marginal. Panel (b) shows a typical variation in O of up to ±7.5% and panel (d) shows a typical variation in H of up to ±10%.

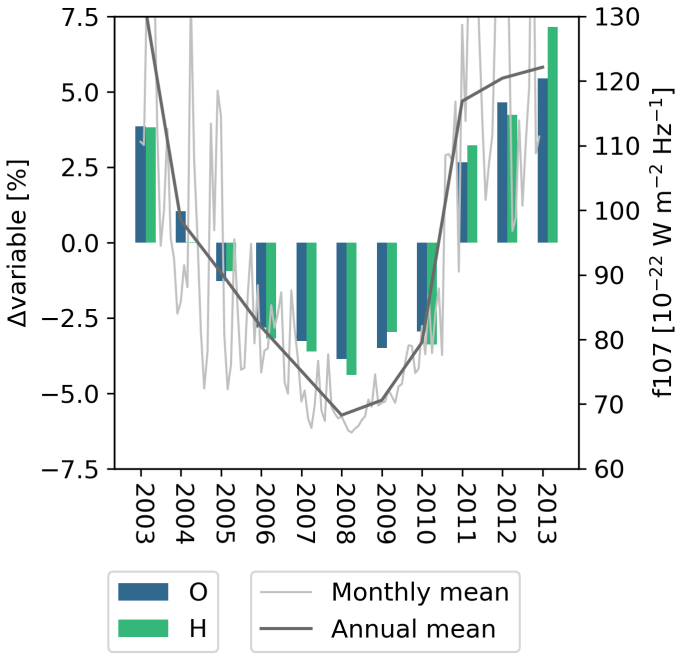

Figure 4.10 (Left axis) annual mean percentage difference from the 11-year solar cycle mean at 120 km plotted for the individual years in the period, for (blue) O and (green) H from WACCM-X data. (Right axis) solar flux at 10.7 cm (10^{-22} W m^{-2} Hz^{-1}) plotted as (light grey) monthy means and (dark grey) annual means.

Therefore, I conclude that the extent of tracer VMR change at 120 km arising across a solar cycle is too large to disregard through the use of just one arbitrary year in prospective upper-boundary conditions.

Figure 4.10 is a bar chart containing the annual mean relative variation in O and H from their respective Figure 4.8 baselines, plotted to qualitatively assess solar cycle correlation. Superimposed on this are lines of monthly and annual mean solar flux at 10.7 cm, recorded over the same period to provide a metric of solar activity. It is clear that the highest VMRs of both tracers are simulated at solar maximum, while the lowest are simulated at solar minimum with a gradual decline in between. Extended

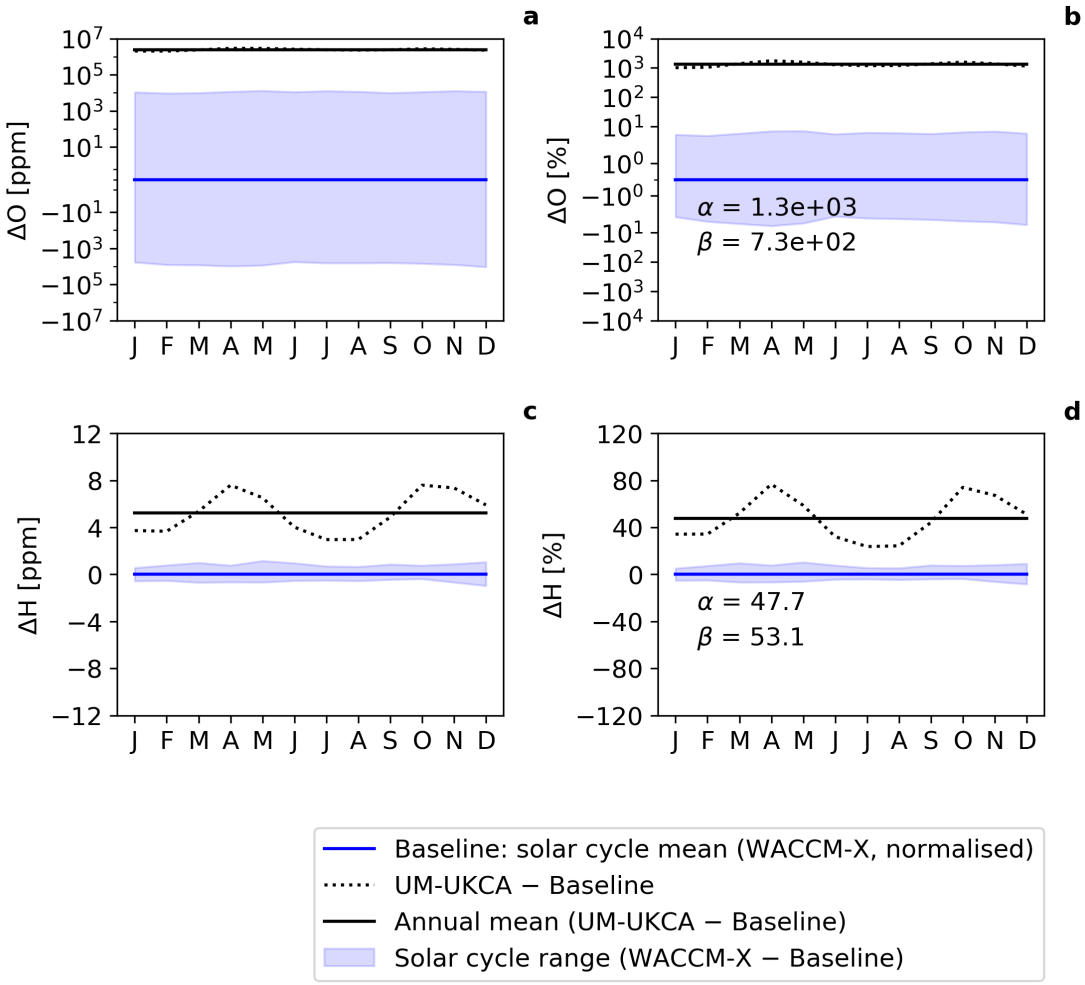

Figure 4.11 Deviation of WACCM-X variables over the 11-year solar cycle (blue fill) versus deviation of UM-UKCA variables over an example year (dotted black line) from the WACCM-X normalised solar cycle monthly mean time series baseline at 120 km (solid blue line). Annual mean UKCA deviations (solid black line) used to calculate mean offset between models (α); UM-UKCA seasonal range (β) also annotated. Absolute deviations (ppm, left) and percentage deviations (right) for (a, b) O and (c, d) H.

UM-UKCA upper-boundary conditions constructed from this data must account for this. For the case of the first model extension phase reported in this chapter, prescribing the solar-cycle-mean time series from Figure 4.8 would be the most suitable treatment for the initial perpetual year simulations.

Next, I assess whether the inherent offsets in the Extended UM-UKCA O and H distributions relative to the WACCM-X solar-cycle-mean distributions are large enough to warrant the implementation of upper-boundary conditions. Top-level treatments are not imposed by default, as merits of such corrections are balanced by the drawback of UKCA-generated seasonal variation being removed from the simulations. My criteria for warranting upper-boundary conditions are: i) if the mean magnitude of the UKCA-to-WACCM-X offset is greater than the UKCA seasonal range; and ii) if the UKCA seasonal variation does not intersect the WACCM-X solar cycle variation.

Figure 4.11 reveals the exact differences between the existing Extended UM-UKCA O and H output and the corresponding solar-cycle-mean WACCM-X output at 120 km. Annotated on each subplot are the terms α and β, representing the magnitudes of the UKCA offsets and seasonal variations respectively. The first criteria for upper-boundary conditions (specified above) can be simplified to where $\alpha > \beta$. Panels (a) and (b), on the log scale, show an obvious void between the two models in their generation of O, indicative of the known order-of-magnitude discrepancy. Here, $\alpha > \beta$ (by nearly a factor of ten) and the UKCA seasonal variation does not come close to the WACCM-X solar cycle variation. Hence, no further case needs to be made for O and the upper-boundary condition should be applied. In contrast, the decision is not so clear-cut for H. Panels (c) and (d) show that α and β are of similar magnitude, but ultimately $\alpha < \beta$. In addition, the UKCA seasonal variation (dotted line) falls very close to the WACCM-X solar cycle range (blue fill) over the summer months, but does not intersect. Regardless, the first criteria for upper-boundary conditions is not met and therefore the WACCM-X data should not be prescribed for H. Here I conclude that the advantage of maintaining the internal Extended UM-UKCA seasonal variation in H outweighs the disadvantage caused by a slight offset from the WACCM-X reference.

To implement an upper-boundary condition for O, I configured a treatment of asymptotic nudging towards the WACCM-X data. Offsets in the values of O recorded in the top-level of the Extended UM-UKCA against those recorded at the equivalent altitude in the WACCM-X data were continually reduced each time-step. This worked by adding or subtracting (as appropriate) a specified factor of the difference between the instantaneous UKCA-generated mixing ratios and solar cycle mean WACCM-X data. I found that a nudging factor of 0.1 was optimal for implementing the upper-boundary condition effectively without inducing further model instabilities. Testing revealed that simulations with more aggressive nudging factors would crash after a few time-steps with errors in the UKCA tracer arrays, caused by a large difference between the first and second uppermost model levels of O.

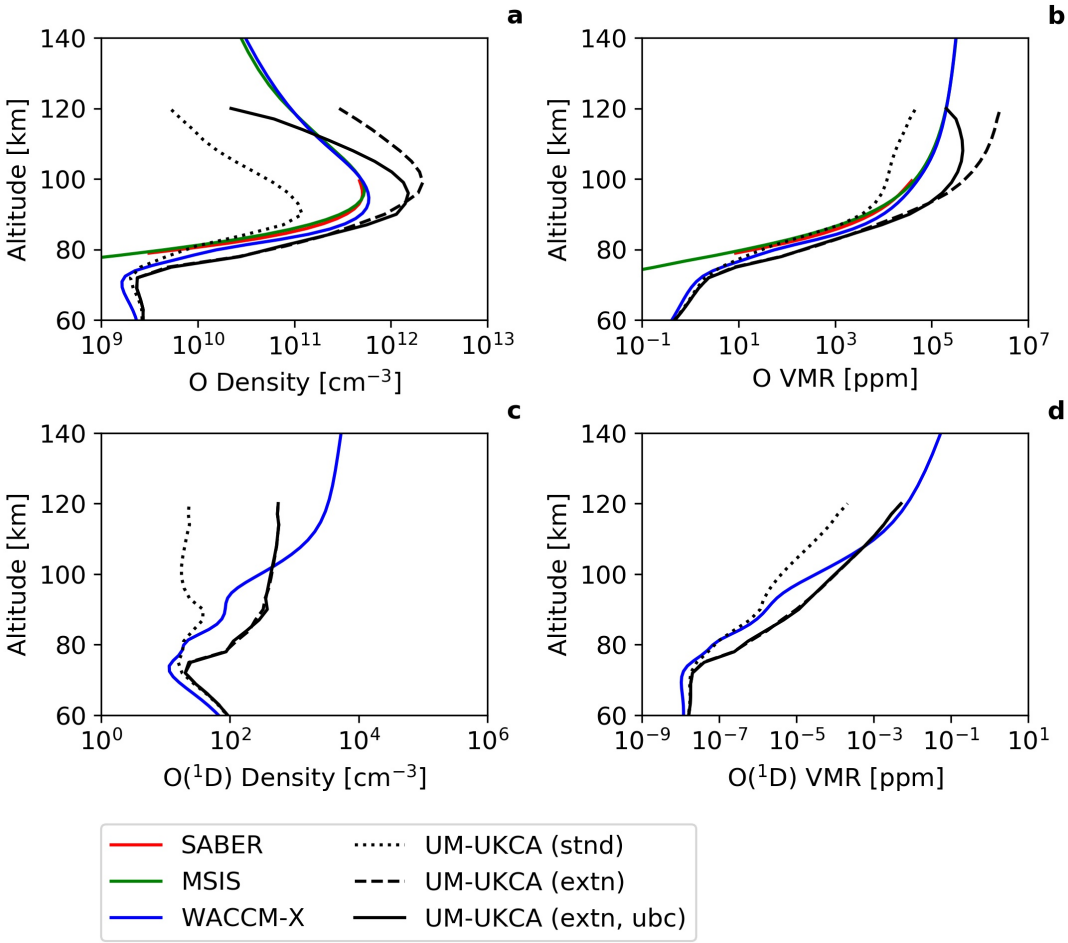

Figure 4.12 Zonal mean, meridional mean for range 80°S-80°N, annual mean altitude profiles of (a, b) ground state atomic oxygen, O and (c, d) first electronic excited state atomic oxygen, O(^{1}D), as number densities (cm^{-3}, left) and VMRs (ppm, right). Profiles include (dotted black) UM-UKCA without photolysis extension, (dashed black) UM-UKCA with photolysis extension, (solid black) UM-UKCA with photolysis extension and upper-boundary condition for O, (solid red) SABER observations, (solid green) MSIS data and (solid blue) WACCM-X data.

Results from an Extended UM-UKCA simulation containing the upper-boundary condition for O (extn, ubc) are included in Figure 4.12. To assess the relative improvement on the previous checkpoints reported in this chapter, profiles from the simulation without photolysis developments (stnd) and the simulation with photolysis developments but no top-level treatment (extn) are replotted from Figure 4.2. Profiles from SABER, MSIS and WACCM-X are also used for reference, as before. I consider O (Figures 4.12a and 4.12b) alongside O(^{1}D) (Figures 4.12c and 4.12d), as O(^{1}D) was deemed the next tracer most susceptible to the new top-level of O. However, it is clear that the O(^{1}D) steady-state calculation is not significantly perturbed by this, as close replication to WACCM-X is maintained. For O itself, the difference between the UKCA profiles with and without the upper-boundary condition is negligible up to an altitude of about 95 km. This confirms that the new treatment causes no adverse impact on the lower levels of the model. Above 95 km, the effect of the upper-boundary condition on O is realised. An exponential decrease in O is seen with increasing altitude, until the UKCA profile intersects with MSIS and WACCM-X at 120 km (in VMR). I conclude that the implementation of an upper-boundary condition for O based on WACCM-X data has undoubtedly improved the agreement between the Extended UM-UKCA and the target reference data. Subsequent simulations should therefore continue to use this treatment.

4.5 Chemical Heating

The second vertical extension phase of the UM-UKCA will require the chemistry and radiation schemes of the model to be coupled for the provision of direct chemical heating in the MLT. As a preparatory step for that, I make an offline estimate for the total daily rate of chemical heating that can be expected from the model in its current state. This estimation is based on simulated annual mean tracer densities, highlighting the individual contributions from each relevant chemical reaction. Mlynczak and Solomon (1993) identified seven particular reactions deemed likely to be responsible for substantial heating in the MLT. Listed in Table 4.3, five are reactions of O (R4.12, R4.13, R4.14, R4.15 and R4.17) and two are reactions of H (R4.16 and R4.18). Also included in the table are three chemical reactions (R4.19-4.21) considered by Marsh et al. (2007) that were not listed by Mlynczak and Solomon (1993). These include the quenching deactivation of O(^{1}D) to the ground state (R4.19). This route was shown

by Marsh et al. (2007) to be the dominant source of chemical heating above about 100 km.

Table 4.3 Important exothermic reactions for chemical heating in the mesosphere-lower thermosphere. R4.12-4.18 from first seven rows of Table 4 in Mlynczak and Solomon (1993), R4.19-4.22 from Figure 5 in Marsh et al. (2007). Molar enthalpies from Mlynczak and Solomon (1993) (R4.12-4.18) and Baulch et al. (2005) (R4.19-4.21), all converted to J mol^{-1}. Rate terms k_0, n and Ea for Arrhenius expression of form $k(T) = k_0(T/298)^n e^{-Ea/RT}$ from Atkinson et al. (2004) (R4.12, R4.14, R4.15), Tsang and Hampson (1986) (R4.13), Turányi et al. (2012) (R4.16), DeMore et al. (1997) (R4.17, R4.18, R4.19, R4.20) and González et al. (2001) (R4.21).

Reaction	Molar Enthalpy ($\Delta H/n$) [J mol^{-1}]	Rate Constant (k_0)	Rate Power (n)	Activation Energy (Ea) [J mol^{-1}]	
$O + O_3 \rightarrow O_2 + O_2$	-3.92e+5	8.00e-12		1.71e+4	(R4.12)
$O + O + M \rightarrow O_2 + M$	-4.50e+5	5.21e-35		-7.48e+3	(R4.13)
$O + OH \rightarrow H + O_2$	-7.02e+4	2.40e-11		-9.15e+2	(R4.14)
$O + HO_2 \rightarrow OH + O_2$	-2.23e+5	2.70e-11		-1.86e+3	(R4.15)
$H + O_2 + M \rightarrow HO_2 + M$	-2.05e+5	4.11e-32	-1.10		(R4.16)
$O + O_2 + M \rightarrow O_3 + M$	-1.07e+5	6.01e-34	-2.30		(R4.17)
$H + O_3 \rightarrow OH + O_2$	-3.22e+5	1.40e-10		3.91e+3	(R4.18)
$O(^1D) + M \rightarrow O + M$	-1.90e+5				(R4.19)
$M = N_2$		1.79e-11		-9.15e+2	*(.19a)*
$M = O_2$		3.20e-11		-5.82e+2	*(.19b)*
$N + NO \rightarrow N_2 + O$	-3.14e+5	2.09e-11		-8.31e+2	(R4.20)
$N(^2D) + O_2 \rightarrow NO + O$	-3.63e+5	1.22e-11		2.64e+3	(R4.21)
Ion reactions	various	various		various	(R4.22)

Into the ionosphere, the heating contribution from ion chemistry reactions (R4.22) must also be considered. This collective contribution was shown by Marsh et al. (2007) to be the second most substantial source of chemical heating above about 105 km. Of course, an efficient Extended UM-UKCA ion chemistry scheme is a prerequisite for this contribution to be realised.

My method for estimating the chemical heating contribution from each reaction in Table 4.3 is as follows. I consider the bimolecular reactions (R4.12, R4.14, R4.18 and R4.20) where the rate of reaction is defined generally as

$$rate_{\mathrm{Ri}}(\text{molecules cm}^{-3}\ \text{s}^{-1}) = k_{\mathrm{i}} \cdot [\mathrm{R}_1] \cdot [\mathrm{R}_2] \qquad \text{(E4.02)}$$

and the termolecular reactions (R4.13, R4.16, R4.17 and R4.19) such that

$$rate_{\mathrm{Ri}}(\text{molecules cm}^{-3}\ \text{s}^{-1}) = k_{\mathrm{i}} \cdot N_{\rho} \cdot [\mathrm{R}_1] \cdot [\mathrm{R}_2] \qquad \text{(E4.03)}$$

where k_{i} is the rate constant, N_{ρ} is the atmospheric number density and $[\mathrm{R}_1]$ and $[\mathrm{R}_2]$ are the number densities of reactant 1 and reactant 2 respectively. Note that reactions R4.15 and R4.21 are omitted from this consideration, as HO_2 was not an available output from a comparative WACCM-X simulation and the $N(^2D)$ tracer does not exist in UKCA.

An equation for the daily heating rate contribution is derived below for the example of reaction R4.12. Starting with an expression for the rate of reaction

$$rate_{\mathrm{R12}}(\text{molecules cm}^{-3}\ \text{s}^{-1}) = k_{12} \cdot [\mathrm{O}] \cdot [\mathrm{O}_3], \qquad \text{(E4.04)}$$

Equation E4.04 is divided by the Avogadro constant, $\mathrm{N_A}(\text{mol}^{-1})$, to generate the molar rate per unit volume

$$rate_{\mathrm{R12}}(\text{mol cm}^{-3}\ \text{s}^{-1}) = \frac{(k_{12} \cdot [\mathrm{O}] \cdot [\mathrm{O}_3])}{\mathrm{N_A}}. \qquad \text{(E4.05)}$$

Next, equation E4.05 is multiplied by enthalpy $\Delta H(\text{J mol}^{-1})$ to convert this to an energy rate per unit volume

$$rate_{\mathrm{R12}}(\text{J cm}^{-3}\ \text{s}^{-1}) = \frac{(k_{12} \cdot [\mathrm{O}] \cdot [\mathrm{O}_3] \cdot \Delta H)}{\mathrm{N_A}}. \qquad \text{(E4.06)}$$

Since atmospheric mass density $\rho(\text{kg cm}^{-3}) = m / V$, where m is atmospheric mass and V is atmospheric volume, the energy rate per unit mass can be constructed as

$$rate_{\mathrm{R12}}\left(\text{J kg}^{-1}\ \text{s}^{-1}\right) = \frac{(k_{12} \cdot [\mathrm{O}] \cdot [\mathrm{O}_3] \cdot \Delta H)}{(\mathrm{N_A} \cdot \rho)}. \qquad \text{(E4.07)}$$

Dividing equation E4.07 by specific heat capacity at constant pressure, C_p(J kg^{-1} K^{-1}) = Q / $m{\cdot}\Delta T$, where Q is energy and T is temperature, generates the heating rate

$$rate_{R12}(\mathrm{K\ s^{-1}}) = \left(\frac{dT}{dt}\right)_{R12} = \frac{(k_{12}\cdot[\mathrm{O}]\cdot[\mathrm{O_3}]\cdot\Delta H)}{(\mathrm{N_A}\cdot\rho\cdot C_p)}. \quad \text{(E4.08)}$$

Integrating equation E4.08 over a day yields the daily heating rate contribution from reaction R4.12,

$$rate_{R12}(\mathrm{K\ day^{-1}}) = \int_{day}\left(\frac{dT}{dt}\right)_{R12}. \quad \text{(E4.09)}$$

This process was repeated for the listed reactions and their respective contributions were summed to generate an expression for the total daily heating rate

$$rate_{TOT}(\mathrm{K\ day^{-1}}) = \sum rate_{Ri}(\mathrm{K\ day^{-1}})\ (i=12,13,14,16,17,18,19,20), \quad \text{(E4.10)}$$

which was used to calculate an offline estimate. Once complete, the whole sequence was repeated with WACCM-X tracer fields to calculate a reference estimate to compare to. The contribution of ion reactions (R4.22) were then added to the WACCM-X total.

Figure 4.13 presents the resultant heating rate estimates as global mean altitude profiles for the MLT. Below 80 km, excellent agreement is seen between the Extended UM-UKCA and WACCM-X, where the leading sources of heating are reactions R4.17 and R4.19 generating rates of approximately 1 K day^{-1} each. This similarity reflects the conformity seen in the O and O(^{1}D) tracers between models in this altitude region (see Figure 4.12). Above 80 km, the UKCA total heating rate increases rapidly largely due to enhanced contributions from reactions R4.18 and R4.19, combined with the introduction of significant heating from reaction R4.13. Close to 90 km, a peak total rate of 65 K day^{-1} is yielded. A rapid increase attributable to the same reactions is also seen in the WACCM-X plot, but the near 90 km peak is just over a factor of six times smaller. A discrepancy of about this size was anticipated as it is principally caused by reaction R4.13, specifically the O density offset between models that is well-documented in this chapter.

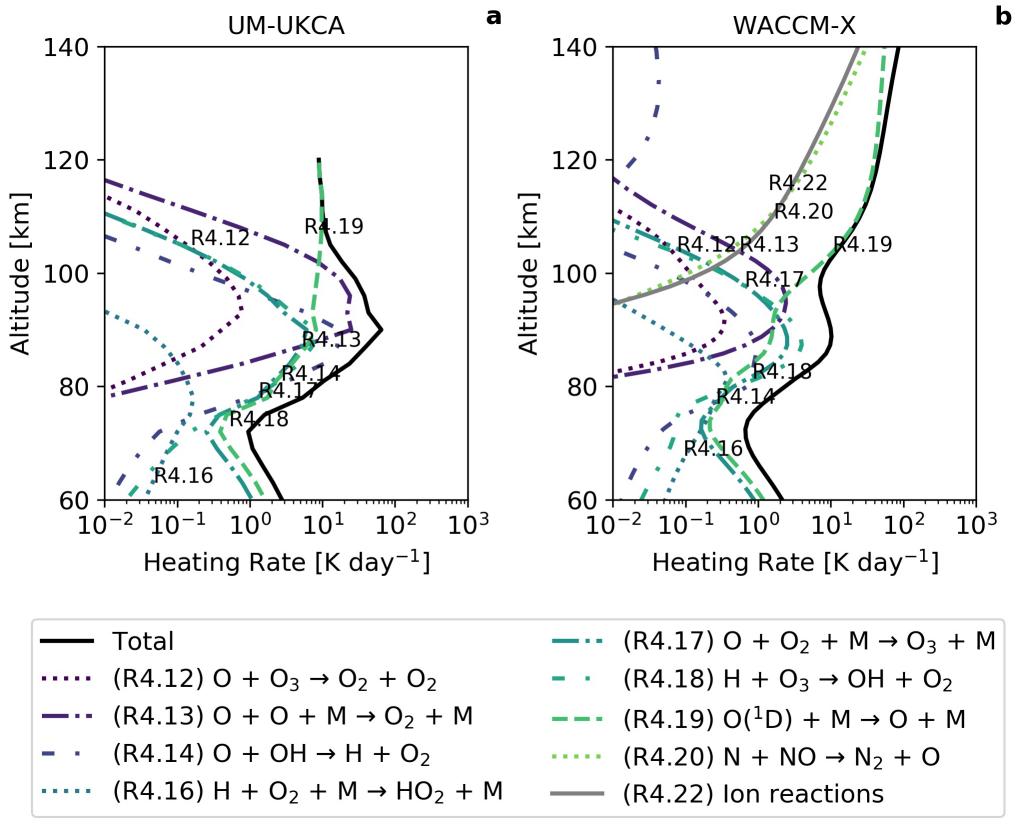

Figure 4.13 Global mean estimated daily chemical heating rate (K day^{-1}) altitude profiles in the MLT for (a) the Extended UM-UKCA and (b) WACCM-X. Includes profiles for the total chemical heating rate (solid black) alongside profiles for the individual contributions from each reaction (various colours and styles – see legend).

Otherwise, generally good agreement is seen between models throughout the MLT, particularly for the reactions involving H. An exception to this is R4.20, the reaction of N and NO. The heating rate contribution from this reaction in UKCA falls short of the x-axis scale used in Figure 4.13, generating a negligible impact compared to that seen in WACCM-X. This was also anticipated to some extent, as the Extended UM-UKCA currently has no representation of Energetic Particle Precipitation (EPP). As discussed in Chapter 2, EPP is a significant source of odd nitrogen (NO_x) in the MLT (Funke et al., 2005). Without this top-down forcing in the model, we cannot expect to simulate realistic amounts of N and NO. Since the provision of EPP representation was not one of the model development objectives within the remit of this thesis, I make no attempt to fill the NO_x deficit. However, the WACCM-X plot shows the increasing relative influence that this reaction has on the total chemical heating rate at altitudes above the current Extended UM-UKCA model lid. EPP NO_x generation is therefore essential for future iterations of the Extended UM-UKCA, particularly those with higher altitude model lids.

Another key difference between panels (a) and (b) in Figure 4.13 is the missing contribution of ion reactions in UKCA. The chemical heating rate profile from ion reactions seen in the WACCM-X plot follows a similar trajectory to that of reaction R4.20. As mentioned previously, an ion chemistry scheme is not being developed in this first phase of the UM-UKCA vertical extension project. Although, the importance of such a scheme for chemical heating upwards through the thermosphere should be noted alongside that of EPP NO_x.

4.6 Summary

The first vertical extension phase of the Extended UM-UKCA up to the intermediate model lid height of 120 km has been completed. I report details of the technical modifications made to couple UKCA to the Extended UM in the Appendix. The results presented in this chapter are directed towards reviewing and improving the basic performance of Extended UM-UKCA neutral chemistry in the MLT. In particular, I focus on air temperature, O and H.

The original temperature profile generated by the model is subject to forcing to a thermospheric climatology above 90 km. I found this forcing to be too weak, with the model unable to replicate the temperatures observed in this region. The addition of a 25 K increment to the forcing provides a better fit. Similarly, a lack of short wavelength photolysis in the default setup gives rise to deficient magnitudes of O and H in the MLT. Through the implementation of extended photolysis treatments for O_2 and H_2O in this work, based on offline rates, production of both species is enhanced. Revised H magnitudes match reference values reasonably well, but revised O magnitudes appear larger than expected, typically exceeding reference VMRs by a factor of ten throughout the extended altitude domain. This can partly be explained by the fact that O_2 is treated as uniform in UKCA, although diagnostic analysis reveals an accumulation of O near the polar region of the summer hemisphere to be a contributing factor, most likely attributable to insufficient model transport in the MLT.

To account for the physical and chemical process occurring above the new model lid, I consider the prescription of upper-boundary conditions for O and H. I utilise data from a long-term WACCM-X run to assess the seasonal and inter-annual variation in

each species. From this, I establish that a solar-cycle-mean of the data would provide the most suitable treatment at the top level. A robust case is made for the implementation of such treatment for O, while I conclude that for H, the existing seasonal variation in the tracer is more valuable than the adjustment offered. Simulations containing this development see an improved representation of O in the lower thermosphere.

The combined effect of exothermic reactions involving O or H constitutes the majority of atmospheric chemical heating, the largest source of heating in the MLT. With both species better characterised in the Extended UM-UKCA, I use model output to estimate a profile for the total rate of chemical heating up to the new model lid. Generally good agreement is seen compared to WACCM-X, aside from two main exceptions. Firstly, the UKCA estimated contribution from the recombination of O reaction is around a factor of six higher than WACCM-X at its peak. This is easily attributable to the known difference in O magnitudes. Secondly, the contribution of the reaction of N and NO is missed entirely by UKCA. Clearly, there is a requirement for EPP driven NO_x generation to be added to the model.

The work completed in this chapter has delivered the Extended UM-UKCA a suitable representation of temperature and neutral chemistry in the MLT, providing a modelling tool for further scientific investigation. The next chapter focuses on testing the chemistry and transport properties of the model, through the addition of the O-controlled and temperature sensitive atomic sodium (Na) chemistry scheme.

5 THE ATOMIC SODIUM LAYER AS A DIAGNOSTIC OF CHEMISTRY AND TRANSPORT IN THE MESOSPHERE-LOWER THERMOSPHERE

5.1 Introduction

I now build on the UK Chemistry and Aerosols coupled Extended Unified Model (Extended UM-UKCA) neutral chemistry developments reported in the previous chapter. The next logical step is to test the chemistry and constituent transport performance of the model through the extended altitude domain. Specifically, through the additional vertical levels in the Mesosphere-Lower Thermosphere (MLT). This chapter reports the inclusion and subsequent analysis of Extended UM-UKCA simulations augmented with an atomic sodium (Na) chemistry diagnostic package. As discussed in Chapter 2, the Na layer originates from material that is released by meteoroids as they ablate in the MLT (Plane, 2015). It provides an excellent tool for chemical and dynamical studies of the MLT due to its relatively long chemical lifetime (Xu and Smith, 2003) and strong sensitivity to temperature (Plane, 2003). Furthermore, the Na chemistry scheme comprises a concise set of largely atomic oxygen (O)- and hydrogen (H)-controlled chemical reactions, providing a robust test of minor constituent chemistry. The Extended UM-UKCA is only the second fully interactive chemistry-climate model to contain such a scheme and the first to do so with a non-hydrostatic dynamical core. Marsh et al. (2013) reported the first of such Na layer simulations completed with the hydrostatic Whole Atmosphere Community Climate Model (WACCM). In this chapter, I compare output from Extended UM-UKCA simulations to updated WACCM simulations (Li et al., 2018) and observational data (Casadio et al., 2007; Fussen et al., 2010; Hedin and Gumbel, 2011; Kopp, 1997). The results aim to offer the first insight into the performance of chemistry and transport in the Extended UM-UKCA, focusing on the MLT. It is intended that the current physical and chemical deficiencies of the model may be quantitatively attributed to imprints in specified diagnostics of the Na layer, including

its spatial and seasonal variation, its overall magnitude and the relative magnitudes of associated Na compounds.

Section 5.2 describes the method used to include an injection of meteoric Na into the Extended UM-UKCA. Section 5.3 reports the addition of an atomic Na chemistry scheme in the model, notably detailing the method used to generate a parametrised ionosphere. Section 5.4 compares the Extended UM-UKCA Na layer simulations completed for the study to a reference WACCM Na chemistry configuration. Section 5.5 presents the results from the Extended UM-UKCA Na layer simulations, with specific attention to the spatial and seasonal variations of Na compounds, as well as the calculation of constituent transport metrics. The main findings from this investigation are summarised in Section 5.6.

5.2 Meteoric Input Function

A Meteoric Input Function (MIF) provides the injection of Na into a model. As reviewed in Chapter 2, the best estimate for the rate of this input function was from Carrillo-Sánchez et al. (2016) at the time of the developments. This MIF specifies the Na injection rate as a particle flux per unit volume, for the altitude range of 50 to 150 km, every 100 m. I adapted this MIF for compatibility with the Extended UM-UKCA. This treatment involved adding meteoric Na as a 3D UKCA chemical emission field.

Firstly, I transformed the vertical profile of the MIF from its original levels onto the Extended UM-UKCA model levels. This involved a mass conserving interpolation, as the UM has a coarse vertical resolution compared to the MIF. Secondly, I converted the units of the MIF to a mass flux for each level, as required by UKCA. This interpolation and conversion yielded the MIF shown in Figure

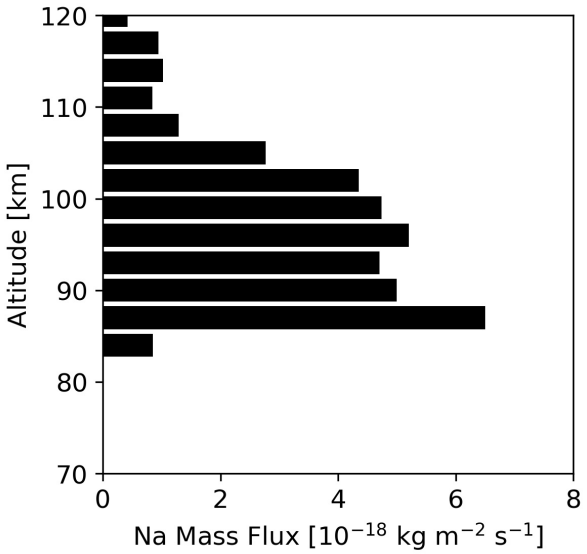

Figure 5.1 Meteoric Na input function based on Carrillo-Sánchez et al. (2016), on Extended UM-UKCA model levels, in mass flux units.

5.1. I used a MIF of single vertical profile to allow results to be attributed clearly to the performance of chemistry and dynamics within the model, removing any uncertainty that could be caused by an input time series. In reality, the rate of Na injection will contain some seasonal and latitudinal variation to reflect changes in the amount and distribution of incoming meteoric material (Janches et al., 2006). It should be noted that the vertical structure of the MIF in Figure 5.1 is attributable to the way in which the estimate is constructed. As discussed in Chapter 2, the main sources of meteoroids are cometary trails and asteroid belt fragments. Naturally, there is considerable variation in the size, velocity and entry angle of meteoroids from both sources. Carrillo-Sánchez et al. (2016) ran an astronomical model to estimate mass and velocity distributions of meteoroids, which were used to drive a chemical ablation model to solve the momentum and energy balance. As a result, some deviation from a completely smooth vertical MIF distribution is to be expected.

Recent WACCM Na scheme simulations, reported in Li et al. (2018), were driven by the Carrillo-Sánchez et al. (2016) MIF. However, Li et al. (2018) found that the Na MIF required a factor of five reduction in order to correctly simulate the observed *absolute* Na density (see Chapter 2). Since the Extended UM-UKCA is also subject to the above limitations and still requires physics developments in the MLT (Griffith et al., 2020), the initial MIF that is used in this study maintains the inferred factor of five reduction. This approach has the benefit of enabling Extended UM-UKCA simulations to be directly compared to the WACCM simulations from Li et al. (2018).

5.3 Atomic Sodium Chemistry Scheme

In total, 11 new chemical tracers were added to the Extended UM-UKCA: five neutral Na compounds (Na, NaO, NaO_2, NaOH and $NaHCO_3$), five ionised Na compounds (Na^+, $Na.O^+$, $Na.N_2^+$, $Na.CO_2^+$, $Na.H_2O^+$) and the dimer $(NaHCO_3)_2$. The chemical reactions and rate equations used in this Na chemistry scheme were taken from Plane et al. (2015). This includes 12 reactions of exclusively neutral compounds (R5.01-5.12) and 11 reactions involving ions (R5.13-5.23), as listed in Table 5.1. I converted the rate equations to satisfy the form of Arrhenius expression for rate of reaction used in UKCA

Table 5.1 Chemical reactions added to the Extended UM-UKCA for the Na chemistry scheme, as listed in Plane et al. (2015), but with rate coefficients converted to the UKCA format.

Reaction	Rate Coefficient	
	Neutral Chemistry	
$Na + O_3 \rightarrow NaO + O_2$	$1.10 \times 10^{-9} \exp(-116/T)$	(R5.01)
$NaO + O \rightarrow Na + O_2$	$(2.69 \times 10^{-10}) (T/300)^{0.50}$	(R5.02)
$NaO + O_3 \rightarrow Na + 2O_2$	$3.20 \times 10^{-10} \exp(-550/T)$	(R5.03)
$NaO + H_2 \rightarrow NaOH + H$	$1.10 \times 10^{-9} \exp(-1100/T)$	(R5.04)
$NaO + H_2 \rightarrow Na + H_2O$	$1.10 \times 10^{-9} \exp(-1400/T)$	(R5.05)
$NaO + H_2O \rightarrow NaOH + OH$	$4.40 \times 10^{-10} \exp(-507/T)$	(R5.06)
$NaOH + H \rightarrow Na + H_2O$	$4.00 \times 10^{-11} \exp(-550/T)$	(R5.07)
$NaOH + CO_2 + M \rightarrow NaHCO_3 + M$	$(1.27 \times 10^{-28}) (T/300)^{-1.00}$	(R5.08)
$NaHCO_3 + H \rightarrow Na + H_2CO_3$	$1.57 \times 10^{-11} (T/300)^{0.78} \exp(-1014/T)$	(R5.09)
$Na + O_2 + M \rightarrow NaO_2 + M$	$(3.05 \times 10^{-30}) (T/300)^{-1.22}$	(R5.10)
$NaO_2 + O \rightarrow NaO + O_2$	$5.00 \times 10^{-10} \exp(-940/T)$	(R5.11)
$2NaHCO_3 + M \rightarrow dimer + M$	$(4.01 \times 10^{-9}) (T/300)^{-0.23}$	(R5.12)
	Ion-Molecule Chemistry	
$Na + O_2^+ \rightarrow Na^+ + O_2$	2.70×10^{-9}	(R5.13)
$Na + NO^+ \rightarrow Na^+ + NO$	8.00×10^{-9}	(R5.14)
$Na^+ + N_2 + M \rightarrow Na.N_2^+ + M$	$(1.97 \times 10^{-30}) (T/300)^{-2.20}$	(R5.15)
$Na^+ + CO_2 + M \rightarrow Na.CO_2^+ + M$	$(1.14 \times 10^{-29}) (T/300)^{-2.90}$	(R5.16)
$Na.N_2^+ + X \rightarrow Na.X^+ + N_2$ ($X = CO_2, H_2O$)	6.00×10^{-10}	(R5.17)
$Na.N_2^+ + O \rightarrow Na.O^+ + N_2$	4.00×10^{-10}	(R5.18)
$Na.O^+ + O \rightarrow Na^+ + O_2$	1.00×10^{-11}	(R5.19)
$Na.O^+ + N_2 \rightarrow Na.N_2^+ + O$	1.00×10^{-12}	(R5.20)
$Na.O^+ + O_2 \rightarrow Na^+ + O_3$	5.00×10^{-12}	(R5.21)
$Na.Y^+ + e^- \rightarrow Na + Y$ ($Y = N_2, CO_2, H_2O, O$)	$(8.16 \times 10^{-7}) (T/300)^{-0.5}$	(R5.22)
$Na^+ + e^- \rightarrow Na + h\nu$	$(2.89 \times 10^{-12}) (T/300)^{-0.74}$	(R5.23)

$$k = k_0 \left(\frac{T}{300}\right)^{\alpha} \exp\left(\frac{-\beta}{T}\right) \quad \text{(E5.01)}$$

where T is temperature and k_0, α and β are coefficients to be determined for each reaction.

Note that the five Na photochemical reactions listed by Plane et al. (2015) were not transferred to the UKCA scheme, as no suitable treatment was available. The omitted reactions were: the photolysis of NaO, NaO_2, NaOH and $NaHCO_3$, and the photoionisation of Na. As a destruction channel of Na, NaO or NaO_2, photolysis/photoionisation is largely inconsequential compared to removal via reaction with O (Self and Plane, 2002). However, a small imbalance of the scheme, caused by insufficient daytime removal of NaOH and $NaHCO_3$, compounds that are instead chemically removed via reaction with the less abundant species, H, should be anticipated in simulations.

5.3.1 Atomic Sodium Ion Production Parametrisation

Unlike WACCM, UKCA did not contain an existing treatment of ions. Therefore, additional work was required before the ion-molecule chemistry could be introduced. The reactions involving the background ions O_2^+ and NO^+ (R5.13 and R5.14) and electrons (R5.22 and R5.23) needed to be accounted for. It would have been both exorbitant and a divergence from the scientific purpose of this study to develop a full description of ion chemistry in UKCA. Instead, the aim was to find the simplest-but-still-realistic representation achievable. I therefore developed a parametrisation for calculating the number density of NO^+, O_2^+ and electrons at any given time or location. This was based on offline photoionisation rates, dissociative recombination rates and a relative ionospheric composition approximation.

Central to the parametrisation are two photoionisation processes to produce molecular ions. That of molecular nitrogen (N_2)

$$N_2 + h\nu \rightarrow N_2^+ + e^- \quad \text{(R5.24)}$$

and that of molecular oxygen (O_2)

$$O_2 + h\nu \rightarrow O_2^+ + e^-. \quad \text{(R5.25)}$$

Between them, reactions R5.24 and R5.25 represent the total input of ions and electrons into the model. Ion production is dependent on sunlight, so in order to capture the diurnal variation across the globe, offline photoionisation rates were provided for reactions R5.24 and R5.25 as a function of pressure and solar zenith angle. Within the parametrisation, these rates were interpolated linearly during simulations for each level and horizontal point, every model time-step (similar to the treatment of photolysis reported in Chapter 4).

The parametrisation was incorporated into the online rate calculation for the relevant reactions via special rate code following the method outlined below (example shown for reaction R5.13).

The overall rate for the bimolecular reaction R5.13 is given by

$$rate = k_{13} \cdot [\mathrm{Na}] \cdot [O_2^+], \quad \text{(E5.02)}$$

where k_{13} is the listed rate coefficient and [Na] and $[O_2^+]$ are the number densities of Na and molecular oxygen (O_2), respectively.

By defining

$$k_{13}' = k_{13} \cdot [O_2^+], \quad \text{(E5.03)}$$

that means $rate = k_{13}' \cdot [\mathrm{Na}]$. The model has an explicit Na number density, so the variable to be determined is k_{13}'. Consider the overall ionisation rate

$$I = k_{\mathrm{DR}} \cdot [M^+] \cdot [e^-] \quad \text{(E5.04)}$$

where k_{DR} is the rate of dissociative recombination, $[M^+]$ is the total ion number density and $[e^-]$ is the total electron number density. Assuming charge neutrality: $[M^+] = [e^-]$, this yields $I = k_{\mathrm{DR}} \cdot [M^+]^2$ which can be rearranged to

$$[M^+] = \sqrt{\frac{I}{k_{\mathrm{DR}}}}. \quad \text{(E5.05)}$$

Introducing a relative ionospheric composition approximation of 80% NO^+ and 20% O_2^+ in the MLT solves for $[O_2^+]$ with

$$\left[O_2^+\right] = 0.2 \cdot \sqrt{\frac{I}{k_{DR}}}. \tag{E5.06}$$

The overall ionisation rate can also be expressed as

$$I = \left(J_{N_2 \rightarrow N_2^+} \cdot [N_2]\right) + \left(J_{O_2 \rightarrow O_2^+} \cdot [O_2]\right), \tag{E5.07}$$

where $J_{N_2 \rightarrow N_2^+}$ and $J_{O_2 \rightarrow O_2^+}$ are the offline photoionisation rates for the production of N_2^+ from N_2 and O_2^+ from O_2, respectively; and $[N_2]$ and $[O_2]$ are the number densities of N_2 and O_2, respectively.

The composition partition used in equation E5.06 can also be applied to the rate of dissociative recombination. Hence,

$$k_{DR} = \left(0.8 \cdot k_{DR(NO^+)}\right) + \left(0.2 \cdot k_{DR(O_2^+)}\right). \tag{E5.08}$$

Therefore, a parametrised rate equation of known quantities may be constructed by substituting equation E5.06 into equation E5.02. This gives

$$rate = k_{13} \cdot 0.2 \cdot \sqrt{\frac{I}{k_{DR}}} \cdot [Na]. \tag{E5.09}$$

This process was repeated to suit reactions R5.14, R5.22 and R5.23 accordingly.

It was necessary to check the validity of this parametrisation before using it in Extended UM-UKCA Na scheme simulations. I made an offline estimate for the electron density of the ionosphere derived from this parametrisation. This was done by calculating $[M^+]$ (hence, charge neutrality) through equation E5.05, but with $[N_2]$ and $[O_2]$ (as required for I, equation E5.07) replaced by values from annual mean Extended UM-UKCA output. Since neither N_2 nor O_2 are advected in UKCA, I calculated their number densities based on their respective, near constant, fractions of the total atmospheric volume density throughout the homosphere (0.78 and 0.21). The same treatment is applied during model simulations inside the UKCA code. In order

to generate an offline global mean electron density profile, I sampled a range of solar zenith angles at frequency intervals of 5° to estimate the electron density of the day-side. I then countered this by factoring in an equal number of zero rates for the photo-inactive night-side, before taking the mean of the samples. Figure 5.2 shows the resulting electron density profile estimate.

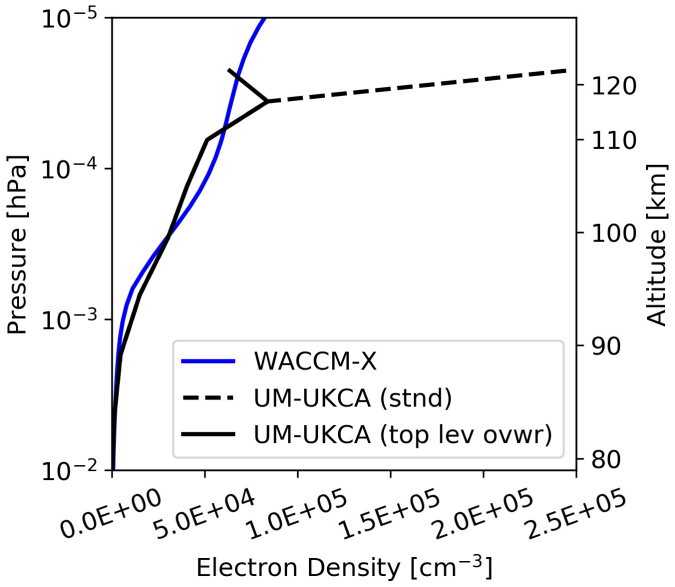

Figure 5.2 Inferred UM-UKCA global mean electron density altitude profiles from the atomic Na ion production parametrisation, compared against the profile from an interactive ionosphere. Profiles are (dashed black) UM-UKCA parametrisation without changes, (solid black) UM-UKCA parametrisation with uppermost photoionisation rate overwritten by second highest rate and (solid blue) WACCM-X output.

It is clear from Figure 5.2 that the ionosphere derived from the Extended UM-UKCA atomic Na ion production parametrisation (stnd) well replicates the global mean electron density generated by WACCM-X, a model with an interactive ionosphere, up to an altitude of about 110 km. However, in the top 10 km of UM-UKCA (which is also the top 10 km of the offline photoionisation rates), the parametrisation yields a significantly higher electron density than that of WACCM-X. At the UM-UKCA model lid (120 km), the magnitude of this discrepancy approaches a factor of five. This sharp rise is solely attributable to the uppermost pressure level of the parametrisation, specifically the associated photoionisation rates $J_{N_2 \rightarrow N_2^+}$ and $J_{O_2 \rightarrow O_2^+}$ (see equation E5.07). The offline photoionisation rates are overestimated at the top pressure level, as their calculation represents the column of the atmosphere from 2.25×10^{-5} hPa up to space. To address this, I derive a second electron density profile that has the top levels of $J_{N_2 \rightarrow N_2^+}$ and $J_{O_2 \rightarrow O_2^+}$ overwritten by the rates from their respective second highest levels. The global mean electron density profile inferred from this calculation is shown in Figure

5.2 as UM-UKCA (top lev ovwr). This revised profile is always inside a factor of 0.3 above or below the WACCM-X profile, a significant improvement on UM-UKCA (stnd). Therefore, this treatment was used in Extended UM-UKCA Na scheme simulations. Note that this top-level issue will be resolved in future versions of the model that are equipped with the new unified photolysis and photoionisation scheme for the whole atmosphere, as mentioned in Chapter 4.

5.4 Extended UM-UKCA Set-up

Model simulations were performed using a revision of the Extended UM-UKCA that contains the neutral chemistry developments from Chapter 4, augmented with the atomic Na chemistry scheme described in Section 5.3. Simulations were for year-2000 lower atmospheric conditions, but since the initialisation atmosphere contained no Na, simulations were started one year before to provide sufficient time for constituent spin-up. I ran two separate configurations of the Extended UM-UKCA, as detailed in

Table 5.2 Configurations of the Extended UM-UKCA simulations and the reference WACCM simulation used in this study. Simulations UKCA and UKCA_10 are identical aside from Na MIF magnitude.

Configuration/ simulation	UKCA	UKCA_10	WACCM
Year	2000	2000	2000
Model lid height	120 km	120 km	~140 km
Number of levels	100	100	70
Horizontal resolution	1.25° × 1.875°	1.25° × 1.875°	1.875° × 2.5°
Vertical resolution (MLT)	3 km	3 km	½ scale height (3-4 km)
Dynamical core	Non-hydrostatic	Non-hydrostatic	Hydrostatic
Na MIF:			
Magnitude	0.06 t d^{-1}	0.006 t d^{-1}	0.06 t d^{-1}
Horizontal variation	None	None	Latitudinal
Time variation	None	None	Monthly

Table 5.2. The first, denoted 'UKCA', contains the Na MIF exactly as described in Section 5.2. The second, denoted 'UKCA_10', contains the Na MIF scaled down by a further factor of ten. Otherwise, the two Extended UM-UKCA simulations are identical to each other.

Also included in Table 5.2 are details of the WACCM configuration used by Li et al. (2018) in their study. In this chapter, I take the WACCM results as the best available model reference of the Na layer. Importantly, WACCM generates a spatial and temporal representation of every Na compound that is involved in the scheme – something that cannot be done via direct observations (as mentioned in Chapter 2). The WACCM results were taken from a 13-year simulation of perpetual year-2000 conditions. To ensure equal model-spin up compared to the Extended UM-UKCA, only the second year of the dataset is used in my analysis. Note that Marsh et al. (2013) also excluded the first year of their simulations from analysis. As discussed in Chapter 3, WACCM is of a different dynamical formulation to the Extended UM-UKCA. Notably, its dynamical core adopts the hydrostatic approximation, putting the model levels on pressure levels. However, the Na MIF used by WACCM is of identical magnitude to that used in simulation UKCA.

5.5 Atomic Sodium Layer Simulations

5.5.1 Magnitude and Distribution

Figure 5.3 presents altitude profiles of Na from the two Extended UM-UKCA simulations (UKCA and UKCA_10), the reference WACCM simulation from Li et al. (2018) and three sets of satellite observations (GOMOS, OSIRIS and SCIAMACHY, see Chapter 3). Starting with the observations, the profiles of GOMOS and SCIAMACHY align very closely, where the magnitude of SCIAMACHY is within 15% of the slightly larger GOMOS at its 92 km annual mean, near global mean peak height. Conversely, OSIRIS is about a factor of two below the mean of GOMOS and SCIAMACHY, vertically throughout the Na layer. The offset of OSIRIS can be explained by its lack of spatial coverage through polar night, overlapping with the horizontal location of observed Na maxima (see Figure 5.15). Considering the models, UKCA simulates Na magnitudes that are at least a factor of ten larger than each of the observations at 92 km. This offset provided the motivation

for completing simulation UKCA_10. UKCA_10 generates a vertical Na profile that appears to scale approximately with the size of the MIF, which well replicates the observed Na densities at 92 km. Therefore, as an initial metric of model performance, it can be concluded that for reasons to be established, the Extended UM-UKCA requires a scaling factor of 50 to simulate the observed *absolute* Na density (an order of magnitude increase on the scaling factor of 5 used by WACCM in Li et al. (2018)). Both UKCA simulations do, however, produce a lower-than-observed peak layer height. WACCM generates more realistic Na magnitudes than UKCA above 80 km, but like UKCA, also simulates a peak layer height below the observations.

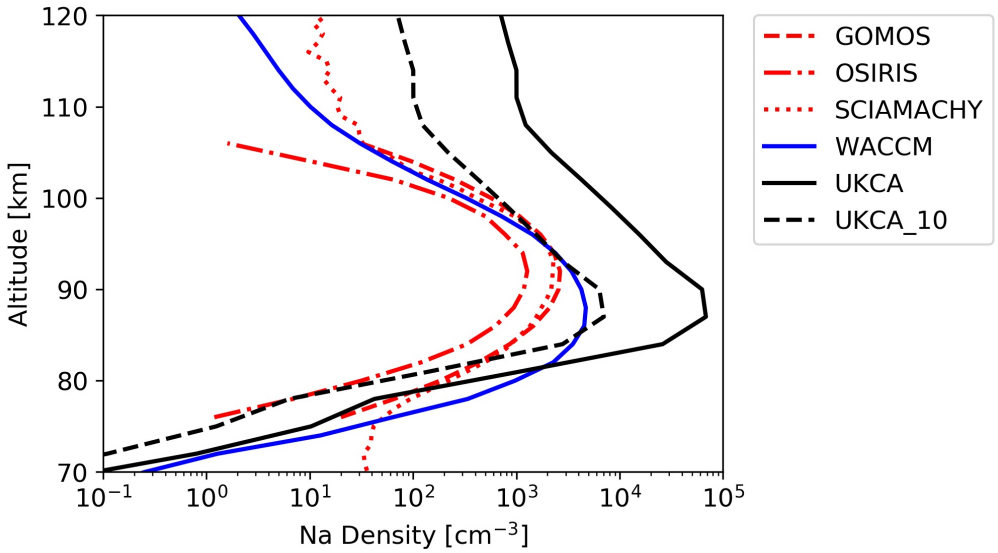

Figure 5.3 Model versus satellite zonal mean, meridional mean for range 80ºS-80ºN, annual mean altitude profiles of Na. Model profiles are (solid black) UM-UKCA, (dashed black) UM-UKCA with scaled down MIF and (solid blue) WACCM. Satellite profiles are (dashed red) GOMOS, (dash-dot red) OSIRIS and (dotted red) SCIAMACHY.

The peak layer height discrepancy that exists between both models and the observations is investigated in Section 5.5.2. A portion of the subsequent analysis in this section investigates the magnitude discrepancy of UKCA compared to WACCM and the observations. However, I first consider the equivalent plot for the atomic Na ion, Na^+. Figure 5.4 shows Na^+ altitude profiles from the Extended UM-UKCA and WACCM simulations, compared to vertical distributions of Na^+ measurements from various rocket sounding campaigns, as described in Chapter 3. Three different statistical averages are plotted from the rocket data: the arithmetic mean, the geometric mean and the median. Simulation UKCA exceeds the upper limit of the

observed density range by at least a factor of 10 throughout the altitude domain. As with the Na profile, the Na^+ profile from simulation UKCA_10 scales linearly with the MIF, resulting in a profile that is just inside the observed range at most altitudes. Excessive Na^+ is also generated by WACCM relative to the observations, albeit to a lesser extent, with the largest magnitude of the disagreement occurring around 95 km. However, reasonable agreement between WACCM and the arithmetic mean of the rocket data is seen above 100 km.

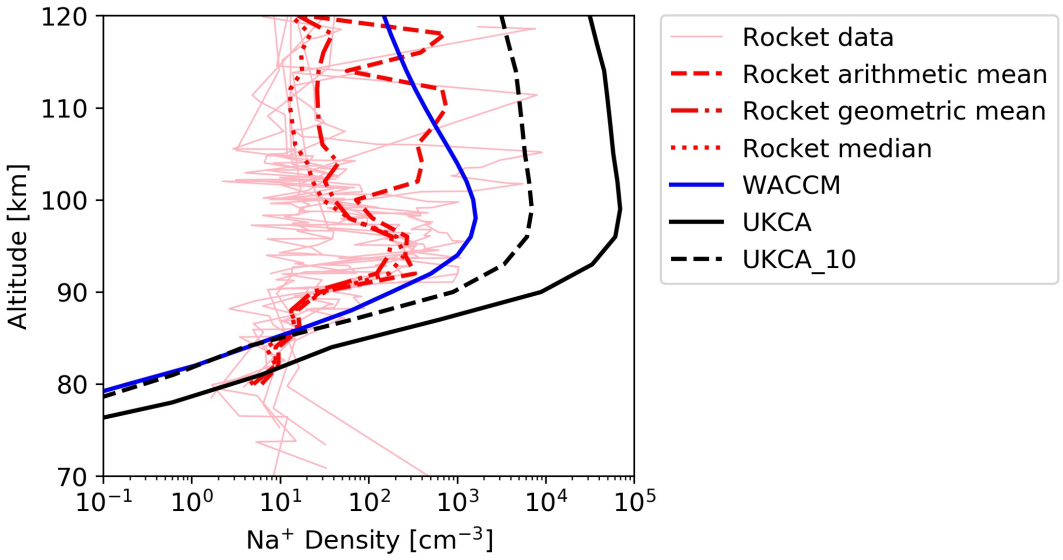

Figure 5.4 Model versus rocket data global mean, annual mean altitude profiles of Na^+. Model profiles are (solid black) UM-UKCA, (dashed black) UM-UKCA with scaled down MIF, (solid blue) WACCM. Rocket profiles are (pale red) the original data, consisting of historical launches from a myriad of dates, times and geographical locations; and three statistical averages: arithmetic mean (dashed red), geometric mean (dash-dot red) and median (dotted red).

From Figure 5.4, it is clear that the overestimation in Na^+ from both Extended UM-UKCA simulations, relative to WACCM and the observational averages, increases with height. At the 120 km model lid, simulation UKCA (UKCA_10) is around 200 (20) times larger than WACCM. Related to this, a particularly noticeable feature from both Figures 5.3 and 5.4 is that the high densities of Na and Na^+ are maintained upwards into the lower thermosphere. Firstly, it is almost certain that both excesses are to some extent attributable to the absence of eddy diffusion in the model. This highlights the importance of vertical transport in determining the Na layer distribution. Hence, a detailed investigation into the transport properties of the model is conducted in Section 5.5.3. Secondly, another plausible contributing factor to the lower-thermospheric excess may be the accumulation of Na and Na^+ in the top levels

of the model, due to the model lid of the Extended UM-UKCA occurring around 20 km lower than that of WACCM. However, there is unfortunately little that can be done about this, as the 120 km vertical limit is an inherent property of this current model version. Finally, the known physical and chemical biases present in the current configuration of the Extended UM-UKCA (as reviewed in Chapter 4) will have impacts of their own on the balance of Na chemistry. It is possible that the conditions resulting from such biases favour the generation of the atomic forms of Na over the heavier metallic compounds. Therefore, an investigation into the distribution of each Na compound among which the remaining original content of the MIF is divided will enable the importance of each bias to be assessed.

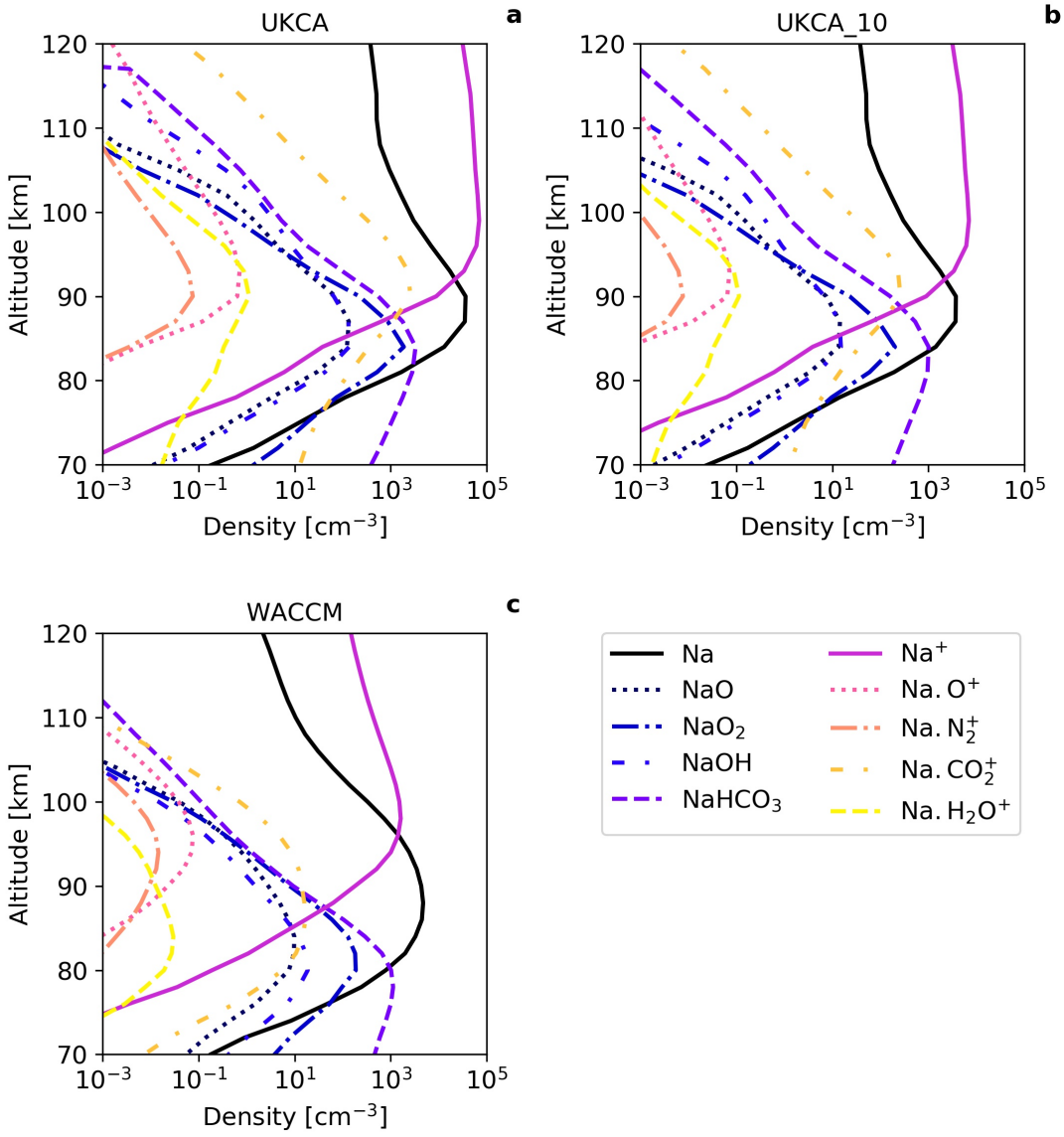

Figure 5.5 Global mean, annual mean altitude profiles of Na and each Na compound (see legend). (a) UM-UKCA, (b) UM-UKCA with scaled down MIF and (c) WACCM, for reference.

Figure 5.5 presents altitude profiles of every Na compound included in the scheme (aside from the $(NaHCO_3)_2$ reservoir), plotted for each model. The results generated by WACCM are of course not real-world measurements, but they do provide the best available indication of how the various Na compounds behave, based on interactions with an extensively tested, detailed model atmosphere. Attention is drawn to the similarities between models in the vertical distribution of the most abundant species. WACCM and both Extended UM-UKCA configurations simulate a larger density of $NaHCO_3$ than any other compound in the lower altitude domain (up to ~80 km). Above this, Na becomes the leading component, through to an altitude of at least 90 km. The upper altitude domain in each simulation is subsequently dominated by Na^+. Considering just this order of significance, there is one key difference between UKCA and WACCM. That is, the vertical extent of the Na-dominated region. In WACCM, Na is the dominant species up to an altitude of above 95 km. However, in UKCA, Na^+ takes over from just above 90 km. Although it is acknowledged that both Na and Na^+ are overestimated by UKCA (Figures 5.3 and 5.4), it is clear from Figure 5.5 that there is consistently a larger Na^+ to Na ratio in UKCA compared to WACCM above 90 km. Hence, one likely explanation for the UKCA Na layer being thinner than the corresponding layer in WACCM is excessive Na^+ generation. Later in the section, in Figures 5.9 and 5.10, Na-normalised profiles of each compound are plotted to investigate this particular observation and highlight any similar cases.

I now review the altitude profiles of the other, minor Na compounds from the scheme. The compounds: NaO, NaO_2, NaOH, $Na.O^+$, $Na.N_2^+$, $Na.CO_2^+$ and $Na.H_2O^+$ are all short-lived intermediates (Plane, 2004), with chemical lifetimes of just a few seconds (Self and Plane, 2002). For their analysis, I focus on comparing UKCA_10 in Figure 5.5b to WACCM in Figure 5.5c, as UKCA_10 contains more realistic magnitudes of Na and Na^+ than the standard UKCA simulation. On first inspection, there appears to be a reasonably good agreement between the simulations in terms of the magnitude and distribution of each species. This indicates that i) the background neutral MLT of the Extended UM-UKCA, developed in Chapter 4, is capable of producing an Na compound partitioning similar to that of WACCM and ii) the Na ion production parametrisation developed in Section 5.3.1 is working satisfactorily. There are, however, a couple of discrepancies above 100 km that should be noted.

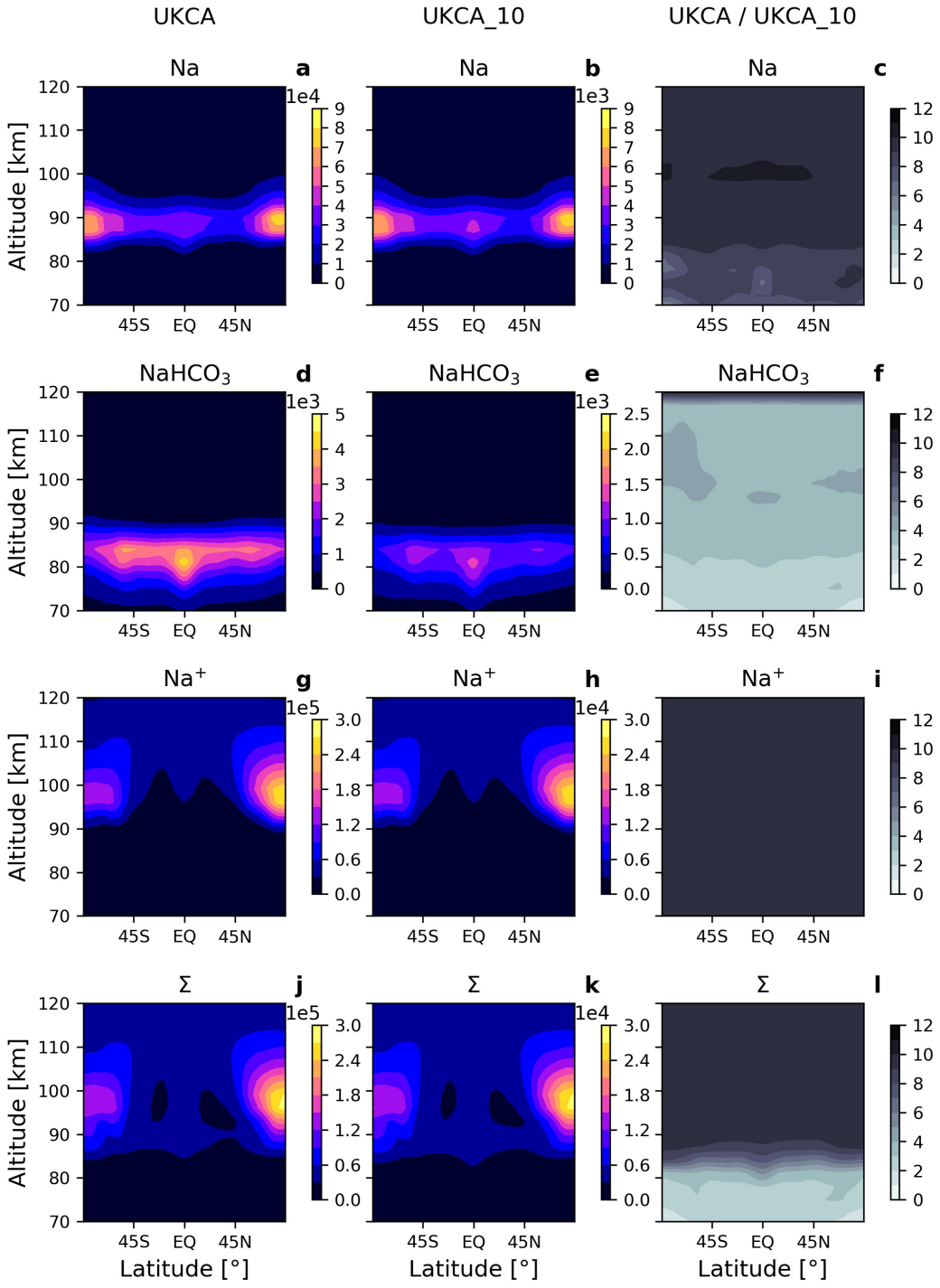

Figure 5.6 Latitude-height zonal mean, annual mean cross-section number densities (cm^{-3}) of (a, b) Na, (d, e) $NaHCO_3$, (g, h) Na^+ and (j, k) their sum. Shown are simulations from (left column) UM-UKCA and (middle column) UM-UKCA with scaled down MIF. Note different colour scales (factor of 10) between the left and middle columns, aside from (d) and (e) (factor of 2). Right column shows the ratio between simulations, calculated for (c) Na, (f) $NaHCO_3$, (i) Na^+ and (l) their sum.

There is a large relative difference in the UKCA_10 simulated magnitude of $Na.CO_2^+$ compared to the corresponding WACCM magnitude, most significant near the Extended UM-UKCA model lid. A significant overestimate of each Na ion-molecule would be expected due to the factor 20 relative excess of Na^+, however UKCA_10 generates $Na.CO_2^+$ magnitudes that are over 1000 times greater than WACCM. $Na.CO_2^+$ is produced by either reaction R5.16 or R5.17, which both involve CO_2. A small part of the UKCA_10 excess can be explained by the breakdown of the assumption that CO_2 has a uniform volume mixing ratio (VMR) throughout the atmosphere (see Chapter 3). This causes there to be around twice as much CO_2 at 120 km in the Extended UM-UKCA than in WACCM. In reality, the mixing ratio of CO_2 decreases above about 80 km due to photolysis, as well as diffusive separation, since CO_2 has a molecular mass greater than that of air (Chabrillat et al., 2002). However, the combined offsets of Na^+ and CO_2 only account for a maximum 4% of the simulated $Na.CO_2^+$ excess. Clearly, there are some imbalances of Na ion-molecule partitioning in the Extended UM-UKCA. Conversely, the CO_2 offset does have a proportionately larger impact on the second notable discrepancy. Above 100 km, where $NaHCO_3$ may also be considered a minor constituent of the scheme, the UKCA_10 profile of $NaHCO_3$ is typically a factor of ten greater than WACCM. CO_2 is involved in reaction R5.08, the only $NaHCO_3$ production

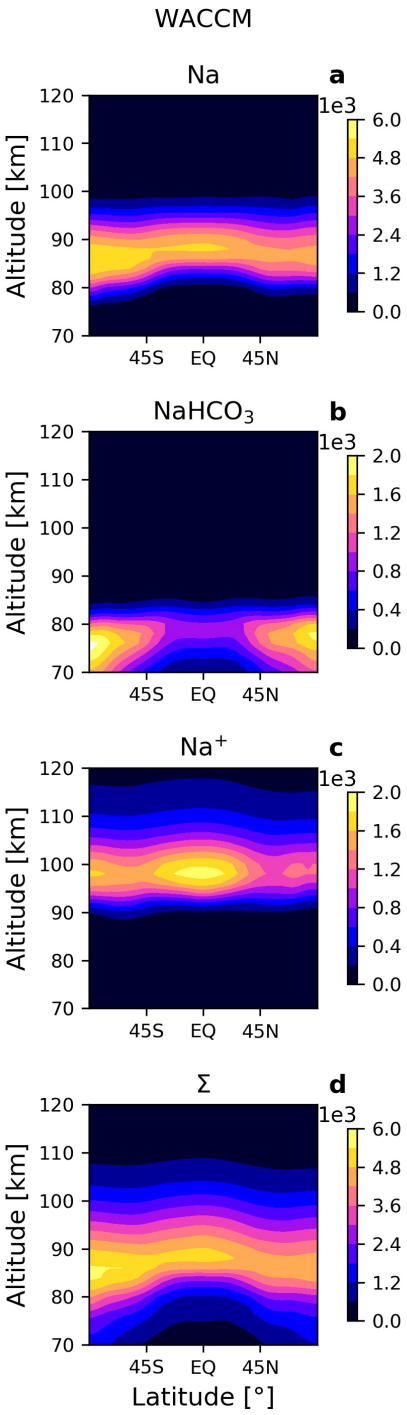

Figure 5.7 Latitude-height zonal mean, annual mean cross-section number densities (cm^{-3}) of (a) Na, (b) $NaHCO_3$, (c) Na^+ and (d) their sum from WACCM simulation. Note different colour scales.

mechanism. Therefore, up to 20% of the lower-thermospheric $NaHCO_3$ excess can be attributed to the approximation of uniform CO_2 in the MLT. Clearly, it is necessary (in future work) to explicitly solve for CO_2 in the MLT in order to accurately simulate the minor chemistry of the Na layer. However, it appears that on average, the Extended UM-UKCA handles the partitioning of neutral Na compounds better than the ion-molecules.

The major layers of the scheme that were identified from Figure 5.5: Na, $NaHCO_3$ and Na^+, as well as their sum, are plotted as latitude-height cross-sections for the Extended UM-UKCA and WACCM simulations in Figures 5.6 and 5.7, respectively. From this, the meridional distribution of each layer can be analysed, and the overall most influential Na compound from each simulation can be inferred. Also included, in panels (c), (f), (i) and (l) of Figure 5.6, are plots of the ratio between simulations UKCA and UKCA_10 for each species, in the same projection.

From a qualitative comparison of the left and middle columns of Figure 5.6, it appears that the factor of ten reduction in the size of the Na MIF has no noticeable impact on the relative spatial distribution of Na, $NaHCO_3$ or Na^+. Regarding magnitude, firstly of Na and Na^+, Figures 5.6c and 5.6i show that the linear scaling of Na and Na^+ with the size of the MIF, concluded from the near-global means of Figures 5.3 and 5.4, is also valid for any given latitude region. It is clear from Figure 5.6f that this near-perfect scaling is not, however, applicable to $NaHCO_3$. Since $NaHCO_3$ removal occurs through the second-order dimerization reaction R5.12 (Plane, 2004), $NaHCO_3$ is proportional to Na by a factor smaller than ten. This factor is quantified for the Extended UM-UKCA by the Na-normalised profile in Figure 5.9d.

Figure 5.7a reveals a key difference in the latitudinal distribution of Na between the Extended UM-UKCA and WACCM simulations. UKCA and UKCA_10 simulate a well-defined pole-to-equator Na density gradient, with peak densities over the polar regions that are more than four times larger than the tropical lows. WACCM, on the other hand, simulates a distribution of Na that is largely homogeneous across all latitudes. This polar bias of Na in UKCA can be explained at least in part by the excess O generated by the Extended UM-UKCA over the summer polar region, as established in Chapter 4 (see Figures 4.5 and 4.6). To substantiate this, Figure 5.8 shows a latitude-height cross-section of O from simulation UKCA, equivalent to the

panels in Figure 5.6. The latitudinal distribution of O in Figure 5.8 is similar to the distribution of Na in Figure 5.6a, albeit with a smaller pole-to-equator relative density gradient. This result supports the well-established notion that a greater density of O will preferentially maintain Na in its atomic form, over the formation of heavier compounds (Plane, 2015). In the UKCA scheme, this occurs through an increased efficiency of reactions R5.02, R5.11, R5.18 and R5.19. It should be noted that insufficient meridional transport is also likely to contribute to the polar bias, which is investigated in Section 5.5.3.

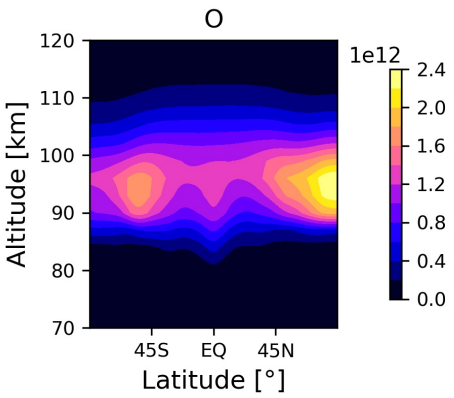

Figure 5.8 Latitude-height zonal mean, annual mean cross-section number density (cm^{-3}) of O from simulation UKCA.

Another difference between models is highlighted by Figure 5.7b. WACCM simulates peak $NaHCO_3$ over the polar regions, while UKCA and UKCA_10 simulate peak $NaHCO_3$ over the equatorial region. In the UKCA scheme, the rate of $NaHCO_3$ generation via reaction R5.08 should vary little with latitude, due to the previously mentioned treatment of uniform CO_2 and the fact that NaOH is short-lived. Furthermore, aside from the dimerization reaction R5.12, the only other removal mechanism of $NaHCO_3$ in the model is through reaction with H (R5.09). In Chapter 4, Extended UM-UKCA H densities were found to be consistent with the observed values and WACCM-X. Therefore, the only chemical explanation for this disagreement between models is again linked to O, via enhanced removal of NaO, hence NaOH and $NaHCO_3$, over the high latitudes. Evidently, much of the difference in distribution can be attributed to meridional transport once again (Section 5.5.3).

Figure 5.7c shows that maximum WACCM Na^+ densities are simulated over the tropical region. This would be anticipated, as the charge transfer of Na to Na^+ through reactions R5.13 and R5.14 is most efficient in the sunlit regions where there is a greater background ion density. UKCA and UKCA_10 generate the opposite result, with maximum Na^+ densities occurring over the high latitudes, as seen in panels (g) and (h) of Figure 5.6. This can be largely attributed to the ion density enhancements

over the tropics being outweighed by the discussed Na density excess over the polar regions. As a result, reactions R5.13 and R5.14 are in fact more efficient closer to the poles than they are over the tropics in the Extended UM-UKCA. The excess of O generated over the summer pole is also likely to contribute to this, by enhanced removal of $Na.N_2^+$ via reaction R5.18 followed by reaction R5.19, inhibiting dissociative recombination of Na^+ back to Na (R5.23). The nature of this contribution is reviewed in more detail in Figure 5.10. Indeed, the Na^+ distribution dominates the Extended UM-UKCA cumulative tracer panels (j) and (k), making it the most abundant component of the Na layer in the model. This contrasts the equivalent WACCM plot in Figure 5.7d, which is dominated by the Na distribution.

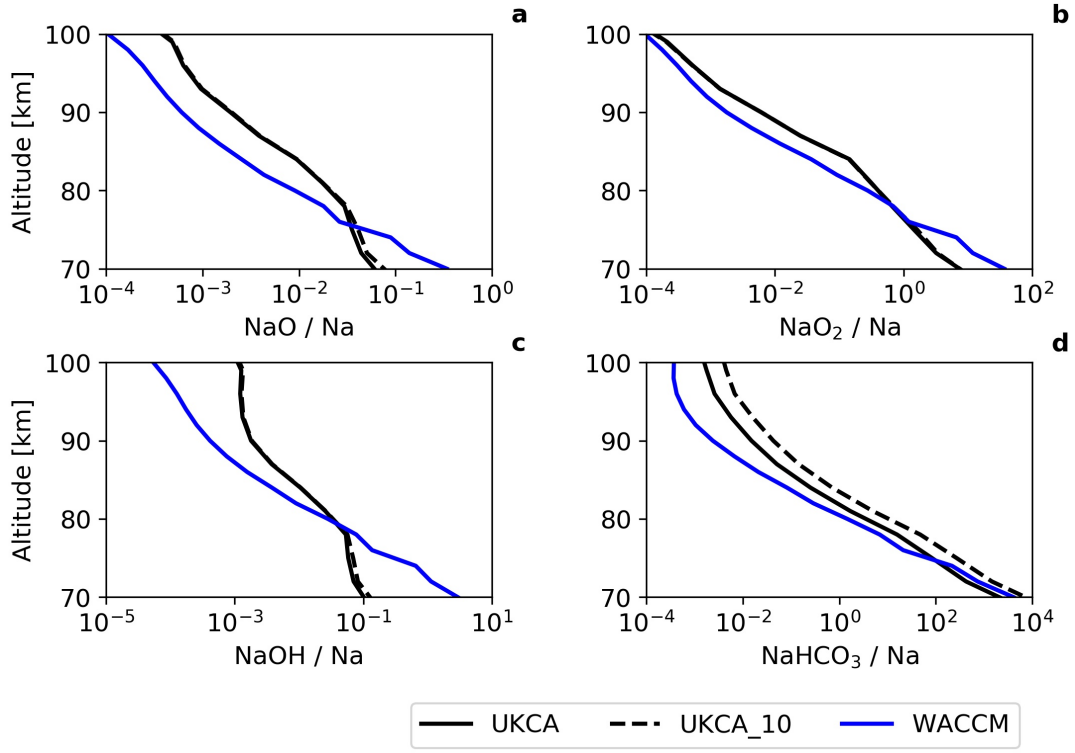

Figure 5.9 Relative magnitude of neutral Na compounds: (a) NaO, (b) NaO_2, (c) NaOH and (d) $NaHCO_3$ after division by atomic Na profile. Profiles are (solid black) UM-UKCA, (dashed black) UM-UKCA with scaled down MIF and (solid blue) WACCM.

Next, I take the focus back to the global mean magnitude of the Na layer. There is motivation generated by the discussion of Figures 5.5 and 5.6 to analyse the relative size of each compound in each simulation, after division by the corresponding Na profile. Figure 5.9 presents Na-normalised profiles for the neutral compounds of the scheme, while Figure 5.10 presents this for the ion-molecules. It is evident from the

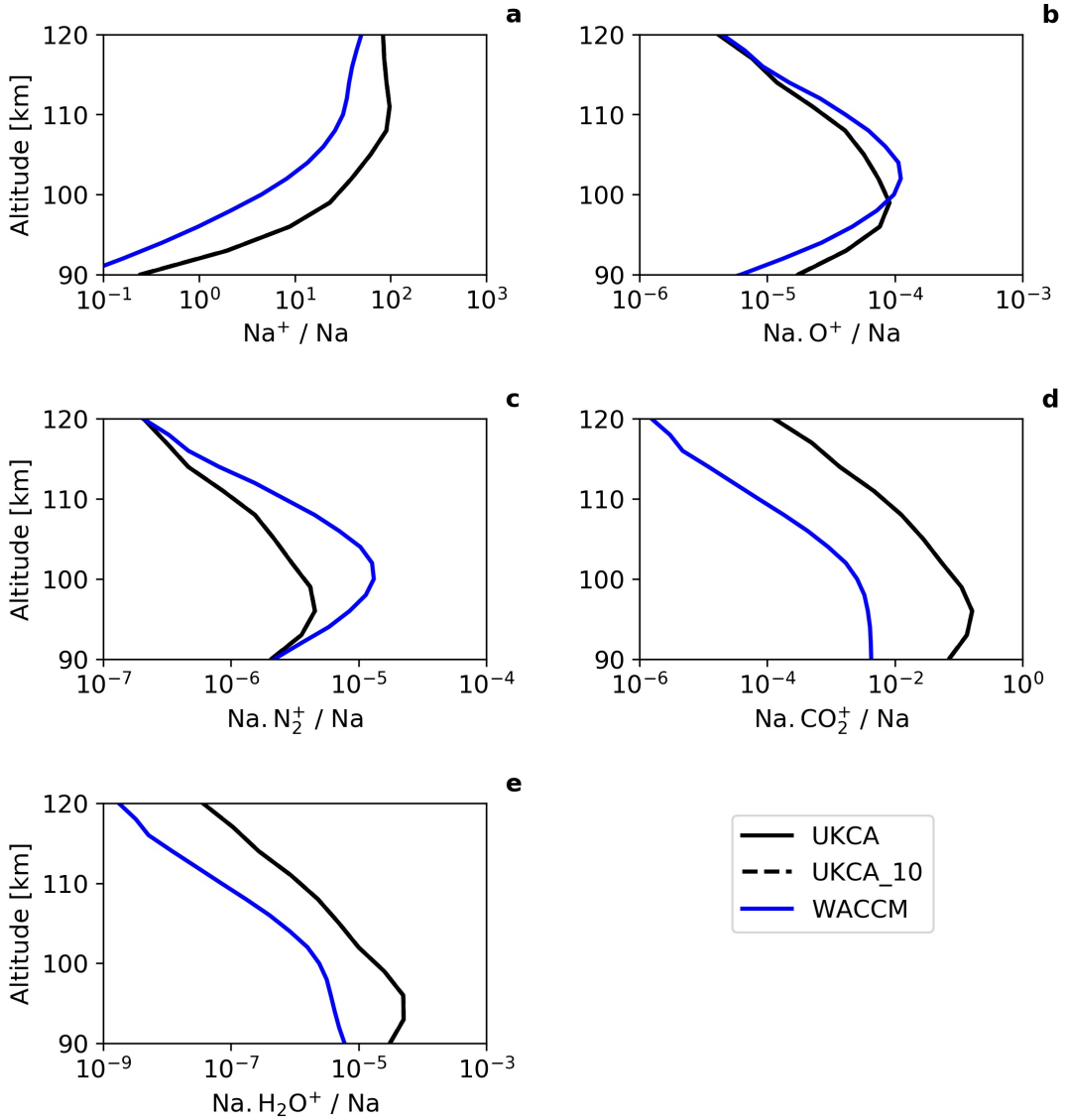

Figure 5.10 Relative magnitude of ionised Na compounds: (a) Na^+, (b) $Na.O^+$, (c) $Na.N_2^+$, (d) $Na.CO_2^+$ and (e) $Na.H_2O^+$ after division by atomic Na profile. Profiles are (solid black) UM-UKCA, (dashed black) UM-UKCA with scaled down MIF and (solid blue) WACCM.

displacement between the profiles of UKCA and UKCA_10, in panel (d) of Figure 5.9, that $NaHCO_3$ is in fact the only compound with a magnitude not directly proportional to the size of the Na MIF. In every other panel of Figures 5.9 and 5.10, the two Extended UM-UKCA simulations are nearly identical. A factor of ten reduction in the injection rate of Na atoms corresponds to just a factor 3-4 reduction in the density of $NaHCO_3$. This disproportionality can be attributed to the removal of $NaHCO_3$ via reaction R5.12. Through this channel, the loss rate of $NaHCO_3$, L, is proportional to the concentration of $NaHCO_3$ squared. That is:

$$L \propto [NaHCO_3]^2. \quad \text{(E5.10)}$$

Therefore, a factor of ten reduction in the rate of $NaHCO_3$ production through reaction R5.08 (caused by a factor of ten reduction in the density of the reactant NaOH) will actually cause a factor of 100 reduction in L. Hence, the density of $NaHCO_3$ approximately scales with the square root of the MIF.

Panels (a), (b) and (c) of Figure 5.9 show that the minor neutral compounds of the scheme have slightly smaller relative densities in the Extended UM-UKCA, compared to WACCM, below about 80 km. However, for the altitudes above the intersection point of the model profiles, slightly larger relative densities are simulated in UKCA. Given the considerably smaller limits of the x-axis scales that are used by these panels, compared to panel (d), I attribute such model offsets to minor variations in the respective background atmospheres of the Extended UM-UKCA and WACCM. The same conclusion can be made for model differences in the relative densities of the minor ion-molecules, in panels (b), (c), (d) and (e) of Figure 5.10.

As pointed out during the analysis of Figure 5.5, it can be seen in Figure 5.10a that above 90 km, the Na^+ to Na ratio is larger in the Extended UM-UKCA than it is in WACCM. Above 100 km, the UKCA ratio is typically 2-4 times the WACCM ratio. The maximum offset is seen at approximately 95 km, where this difference is ×9. There could be a chemical explanation for the component partitioning of the Na layer being weighted so firmly towards Na^+. Specifically, the high level of O contained in the MLT of Extended UM-UKCA simulations. Through a balance of the Na^+ production and loss channels, a greater background density of O is likely to result in an enhanced rate of Na^+ generation via reaction R5.19. Referring back to panels (a) and (b) of Figure 4.12 in Chapter 4, it can be seen that with the upper-boundary condition for O applied (as is the case for simulations UKCA and UKCA_10 in this chapter), the maximum offset between UKCA and WACCM-X O profiles also occurs near 95 km. Around 95 km, the UKCA simulated magnitude of O is approximately ×3 (×5) that of WACCM-X in cm^{-3} (ppm). Hence, I conclude that a disproportionately large level of Na^+ is a signature of a background atmosphere with high levels of O.

There are also likely to be other factors contributing to the high Na^+:Na ratio in the Extended UM-UKCA. Figure 4.1 of Chapter 4 shows that the background atmosphere

of UKCA has a lower temperature than WACCM-X throughout the MLT. At around 95 km, the difference is about 15 K. The principal mechanism for the removal of Na^+ is through the three-body reaction R5.15. Additional Na^+ removal occurs through reactions R5.16 and R5.23. All three destruction channels have temperature-dependent rate coefficients, which are faster at lower temperatures. This implies that the removal of Na^+ via chemistry is in fact more efficient in UKCA than it is in WACCM. Therefore, at least some of the high weighting to Na^+ is probably transport related.

5.5.2 Seasonal Evolution

I now assess the seasonal evolution of the Na layer. First, I analyse how the altitude at which maximum Na occurs varies through the year. The simulated peak height of the Na layer may be used as a model performance metric in the MLT. It also provides an indication into the reliability of the vertical distribution of the associated MIF. The altitude location of peak Na cannot be reliably inferred from a single annual mean, global mean profile (similar to that in Figure 5.3), as it is known to vary with latitude across the seasons (Marsh et al., 2013). Furthermore, models are severely limited by their vertical resolution in the MLT, which is typically of order kilometres (see Table

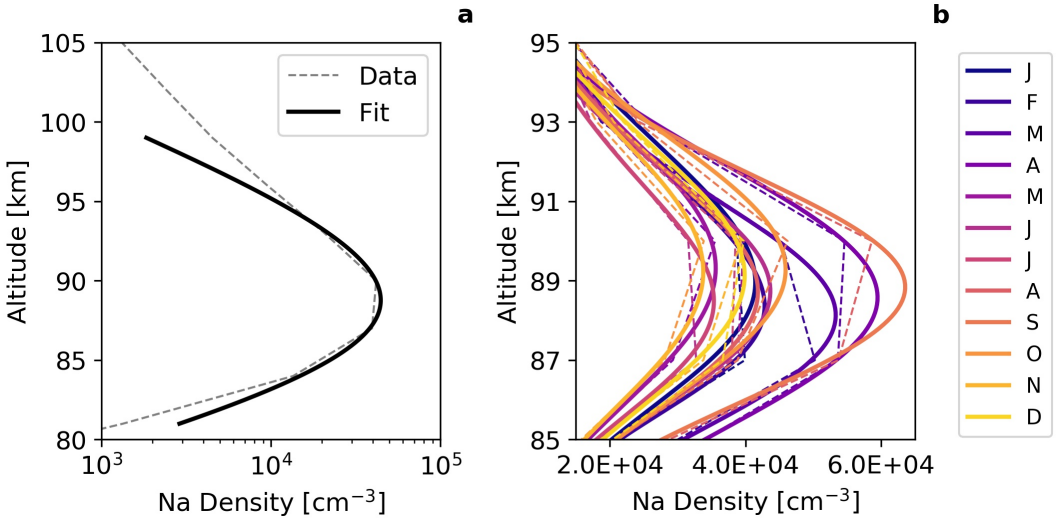

Figure 5.11 Illustration of technique used to calculate Na layer peak height time series in Figure 5.12. (a) A Gaussian fit (solid black) is applied to the data (dashed grey line) over the altitude range of 81-99 km (fully encompassing the Na layer peak). (b) The process is repeated for each monthly mean (see legend) and then latitude point (not shown).

5.2 for Extended UM-UKCA and WACCM values). It is therefore necessary to adopt a more sophisticated approach to represent the simulated peak height.

Figure 5.11 depicts the method used to calculate a latitude-time series for the Na layer peak height. This was based on the curve-fitting method used by Marsh et al. (2013) for the same purpose. However, instead of calculating a quadratic fit to the Na layer profile, a Gaussian fit was applied, as this has previously been shown to offer a better match (Plane, 2004). Individual consideration of each month and latitude point allows the seasonality to be captured, while the application of a continuous function provides a smooth interpolation over the constraints of the angular peak. The resulting plots are

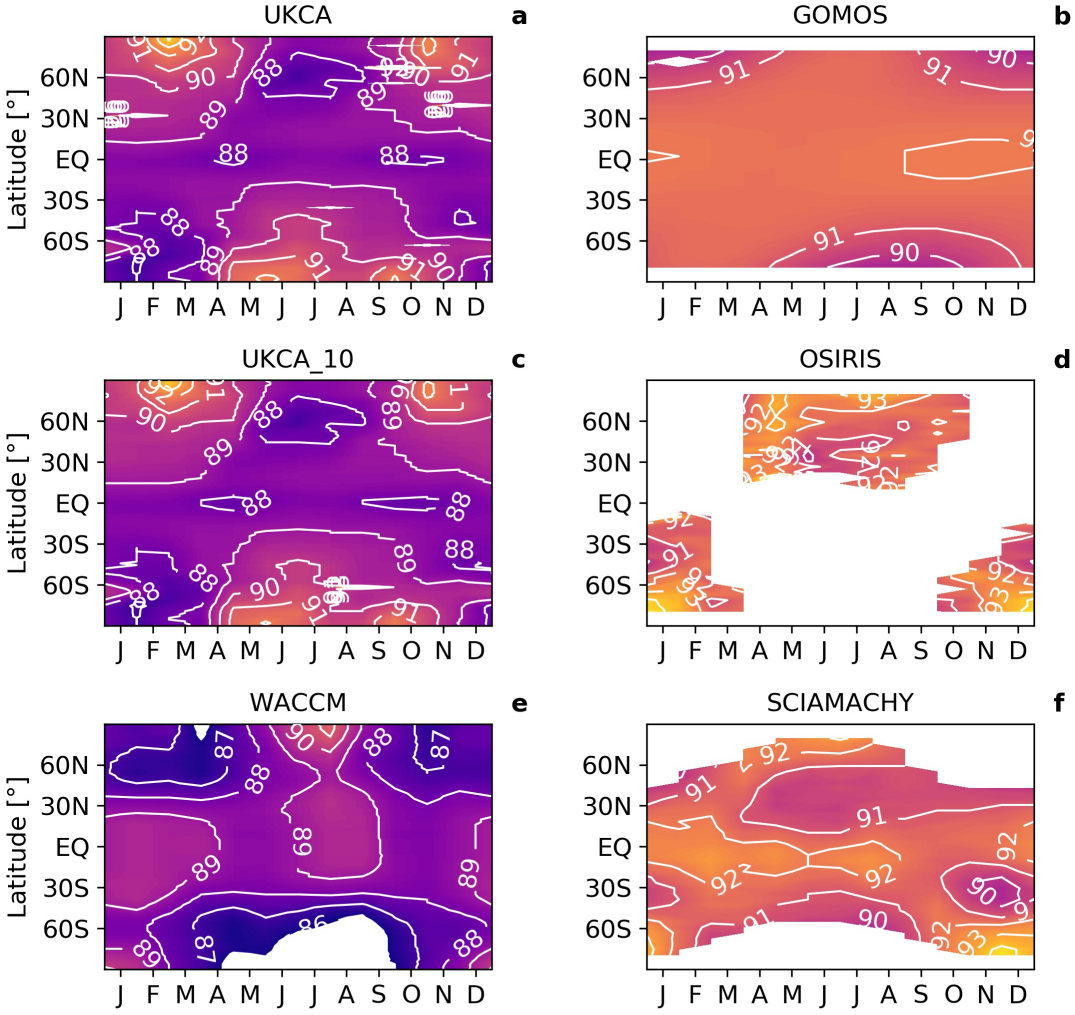

Figure 5.12 Seasonal evolution of zonal mean Na layer peak height (km) from (a) UM-UKCA simulation, (b) GOMOS satellite data, (c) UM-UKCA simulation with scaled down MIF, (d) OSIRIS satellite data, (e) WACCM simulation and (f) SCIAMACHY satellite data. White regions indicate either where measurements were unavailable (satellites), or where a suitable Gaussian fit could not be achieved (models and satellites).

shown in Figure 5.12. The Extended UM-UKCA and WACCM panels in the left column are generated from output sampled at the full horizontal resolution of their model (see Chapter 3), for every time-step. It should be noted that this comprehensive sampling is not replicated by the GOMOS, OSIRIS and SCIAMACHY panels in the right column, which are limited by the availability of satellite measurements. Panels (a) and (c) appear to be virtually identical, which suggests that the size of the MIF has no bearing on the peak height. By comparing the model panels to the satellite panels, it is clear that on average, both the Extended UM-UKCA and WACCM underestimate the observed peak height of the Na layer. Typically, UKCA generates peak heights in the range 88-91 km, while in WACCM, this range is about 2 km lower. GOMOS, OSIRIS and SCIAMACHY corroborate a peak height range of 91-93 km. The largest rate of Na injection from the MIF (used in both models) occurs around 87 km (Carrillo-Sánchez et al., 2016). The precise height of this injection is less important in WACCM than it is in UKCA, as in WACCM, fast vertical transport by eddy diffusion quickly adjusts the vertical distribution of the Na layer. Since the Extended UM-UKCA currently contains no treatment of eddy diffusion, its comparatively better observational agreement than WACCM is likely to be partly attributable to the MIF. There is evidence to suggest that the simulated background atmosphere may also be an important factor in governing the peak height. Marsh et al. (2013) originally highlighted the discrepancy between WACCM and the observed peak height, albeit to a lesser extent, based on simulations with maximum Na injection at a much higher altitude of 102 km (Li et al., 2018). The authors suggested errors in the background density, caused by a warmer-than-observed mesopause temperature as an explanation (Marsh et al., 2013). Following this, the fact that UKCA is able to more closely recreate the observed peak height than WACCM could also be partly attributable to the colder mesopause generated by the Extended UM-UKCA (recall Figure 4.1, Chapter 4). WACCM does, however, more accurately recreate the observed latitudinal variation seen in the Na layer peak height.

Next, I focus on the seasonal evolution of the Na layer component composition. Figure 5.13 presents latitude-time series from simulations UKCA and UKCA_10 for the columns of Na, $NaHCO_3$, Na^+ and their sum, in the MLT. Figure 5.14 shows the equivalent plots from the WACCM simulation, while Figure 5.15 shows only the Na columns, as observed by the GOMOS, OSIRIS and SCIAMACHY satellite

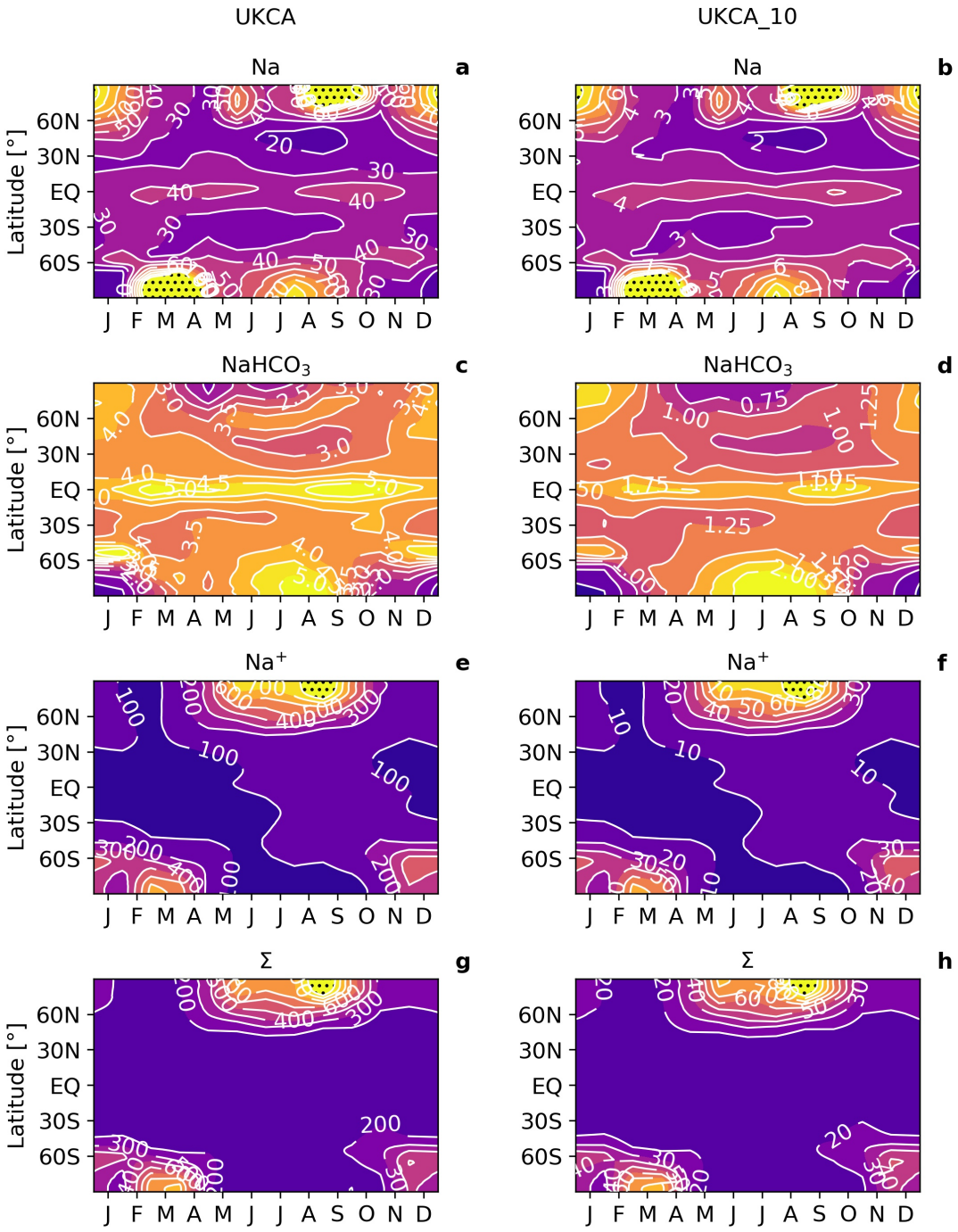

Figure 5.13 50-120 km column (10^9 cm^{-2}) monthly means of (a, b) Na, (c, d) $NaHCO_3$, (e, f) Na^+ and (g, h) their sum from (left column) UM-UKCA and (right column) UM-UKCA with scaled down MIF. Note different contour scales. Excessive values saturated at 100 (left)/10 (right) cm^{-2} for Na, 900/90 cm^{-2} for Na^+ and 1000/100 cm^{-2} for $\sum$ and shown by dotted regions.

instruments. Starting with the Na in panels (a) and (b) of Figure 5.13, very similar seasonal evolutions are seen in each, separated only by a factor of 10 in magnitude, as expected from the analysis of the equivalent panels in Figure 5.6. Undoubtedly, a distinct pattern has formed, with peak Na column occurring over the winter polar

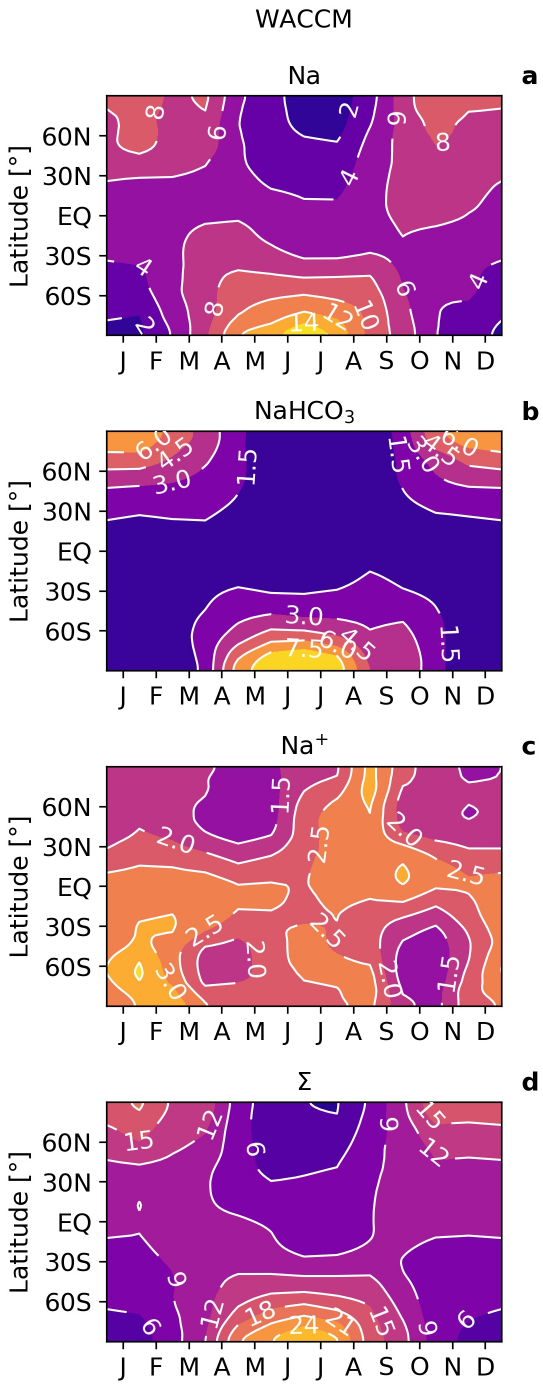

Figure 5.14 Reference 50-120 km column (10^9 cm^{-2}) monthly means of (a) Na, (b) $NaHCO_3$, (c) Na^+ and (d) their sum from WACCM simulation.

regions. This pattern is exclusively attributable to chemistry and transport within the Extended UM-UKCA, as the injection of Na is provided though a time-invariant, single profile MIF. In contrast, the MIF used in the WACCM simulation does contain some seasonal variation (Table 5.2). However, the annual variation of Na simulated by UKCA and UKCA_10 is consistent with the WACCM simulation in Figure 5.14a, with the exception of autumn at high latitudes, where the model shows very high results. This also replicates the findings of Marsh et al. (2013) (generated using a previous WACCM version driven by a MIF based on an older estimate). Importantly, the satellite plots of Figure 5.15 provide observational support to the modelled seasonal evolution of Na. GOMOS (panel a), which offers the largest global coverage out of the three instruments, observes over five-fold enhancements of Na over the peak seasons. OSIRIS (panel b) and SCIAMACHY (panel c) appear to converge towards even greater relative enhancements, but verification of that is inhibited by a lack of measurements over the winter polar regions. However, peak seasonal Na column enhancements of over 7 × 10^9 cm^{-2} have previously been reported from lidar observations at the South Pole (Gardner et al., 2005).

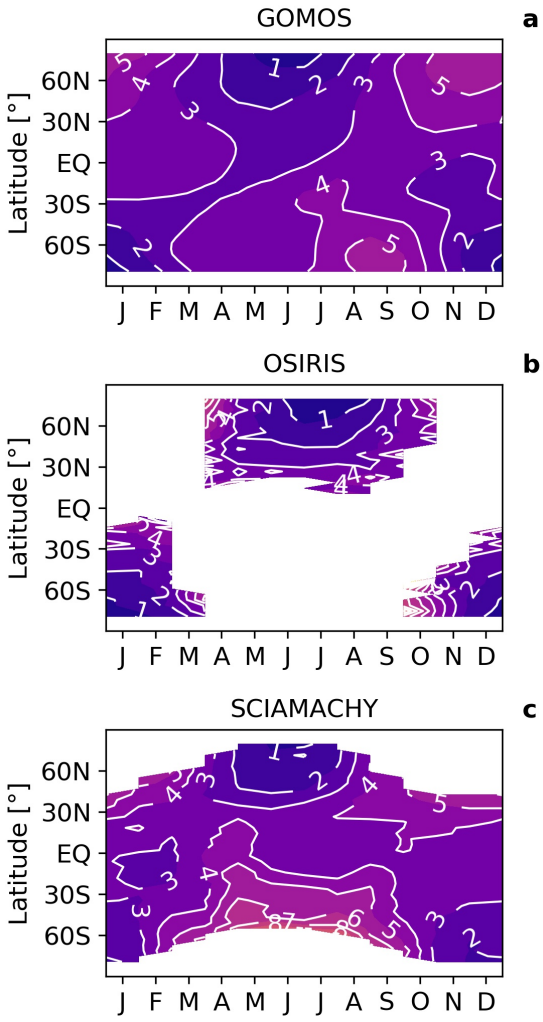

Figure 5.15 Satellite data total column (10^9 cm^{-2}) monthly means of Na from (a) GOMOS, (b) OSIRIS and (c) SCIAMACHY. Colour scale shared with the equivalent WACCM plot in Figure 5.14a for direct comparisons.

The observed and simulated seasonal evolution of Na follows the typical transport circulation pattern of the MLT, whereby mesospheric air is lifted over the summer pole, before being taken across to the winter pole where it descends (see Chapter 2). The fact that the Extended UM-UKCA is clearly able to represent this circulation marks a successful first test of constituent transport through the MLT. There are, however, a couple of features in Figures 5.13a and 5.13b that are not replicated by WACCM nor by the observations. Firstly, as previously mentioned, areas of extremely high Na column (exceeding 100 × 10^9 cm^{-2}) are simulated during autumn in UKCA/UKCA_10, centred over March in the Southern Hemisphere (SH) and September in the Northern Hemisphere (NH). These are indeed peculiar model artefacts, which have no obvious explanation. Whether or not this issue reoccurs in tests using future developments of the Extended UM-UKCA, with more comprehensive descriptions of model dynamics, would provide valuable insight into the nature of the cause. Secondly, column enhancements of over 40 × 10^9 cm^{-2} (4 × 10^9 cm^{-2}) are simulated throughout the year over the equatorial latitudes in UKCA (UKCA_10). Enhancements in this region are not a signature of the known circulation pattern in the MLT. Therefore, they are most likely a symptom of meridional transport deficiencies.

I now consider the seasonal evolution of the other two major compounds of the Na layer: $NaHCO_3$ and Na^+. By comparing panels (c) and (d) of Figure 5.13 to Figure 5.14b, it can be seen that in both models, the key driver of the seasonal evolution in the $NaHCO_3$ column is transport circulation, as was concluded for Na. Interestingly, $NaHCO_3$ is subject to equatorial accumulation in UKCA and UKCA_10, to an even greater relative extent than was seen in the Na column. The $NaHCO_3$ enhancements here are in fact of a similar magnitude to those generated over the winter polar regions in the same simulation. Since the $NaHCO_3$ component of the layer peaks below 80 km (Figure 5.5), this result suggests that the previously postulated Extended UM-UKCA meridional transport deficiencies could extend to lower altitudes than previously thought. Next, comparing panels (e) and (f) of Figure 5.13 to Figure 5.14c shows that, in both models, the seasonal evolution of the Na^+ column anti-correlates with the seasonal evolutions of both the Na and the $NaHCO_3$ columns. It appears that the Na^+ distribution in UKCA has an annual variation controlled by solar zenith angle, as the maximum column occurs over the summer, focused towards the pole. Marsh et al. (2013) simulated a very similar seasonal evolution to that in Figure 5.14c, but attributed the variations to meridional transport. Therefore, it is concluded that any meridional transport of Na^+ in the Extended UM-UKCA is masked by its excessive production via photoionisation, making it a poor tracer of transport.

Lastly, in panels (g) and (h) of Figure 5.13, the latitude-time series for the cumulative column of the three compounds from simulations UKCA and UKCA_10 are dominated by the variations of the Na^+ column. Figure 5.14d shows that in WACCM, the overall seasonal evolution of the layer is dominated by Na. Based on the discussion in Section 5.5.1, an excessive column of Na^+ is to be expected in the Extended UM-UKCA, attributable to high levels of O in the MLT.

5.5.3 Transformed Eulerian Mean Diagnostics

Andrews and Mcintyre (1976) pioneered the use of Transformed Eulerian Mean (TEM) diagnostics as a tool to study the large-scale net motion of air. TEM circulation is an approximation of the overall zonal mean Lagrangian motion of wind driven air parcels in the latitude-pressure plane (Smith et al., 2011). Here, TEM flow velocities are calculated to provide a quantitative measure of simulated net transport circulation through the stratosphere and the MLT. Central to the determination of TEM velocities

is the air temperature diagnostic of the model. It therefore makes sense to evaluate this first. Figure 5.16 shows the seasonal temperature gradient at 90 km for simulations UKCA (panel a) and WACCM (panel b). This was constructed by subtracting the monthly latitudinal temperature variations from the global mean, annual mean value. It provides an indication of temperature perturbations close to the peak of the Na layer.

Good agreement is seen between the models in Figure 5.16 at high latitudes. Here, both UKCA and WACCM simulate positive temperature perturbations of over 15 K during the NH (SH) winter (summer), and negative temperature perturbations of over 30 K during the NH (SH) summer (winter). This supports the notion that the Na and $NaHCO_3$ seasonal evolution patterns in panels a-d of Figure 5.13 are driven by transport circulation and temperature. It also suggests that many of the transport deficiencies apparent from the previous subsections are caused by missing dynamical processes, rather than unrealistic temperatures. UKCA does not, however, replicate the extent to which the negative temperature perturbations in WACCM extend through to the opposing hemisphere. For example, the WACCM NH summertime low in Figure 5.16b remains below -10K up to the equator, while the corresponding UM low in Figure 5.16a dissipates north of the tropics. This would suggest weaker meridional winds, which could explain the equatorial 'trapping' of Na and $NaHCO_3$ seen in panels a-d of Figure 5.13.

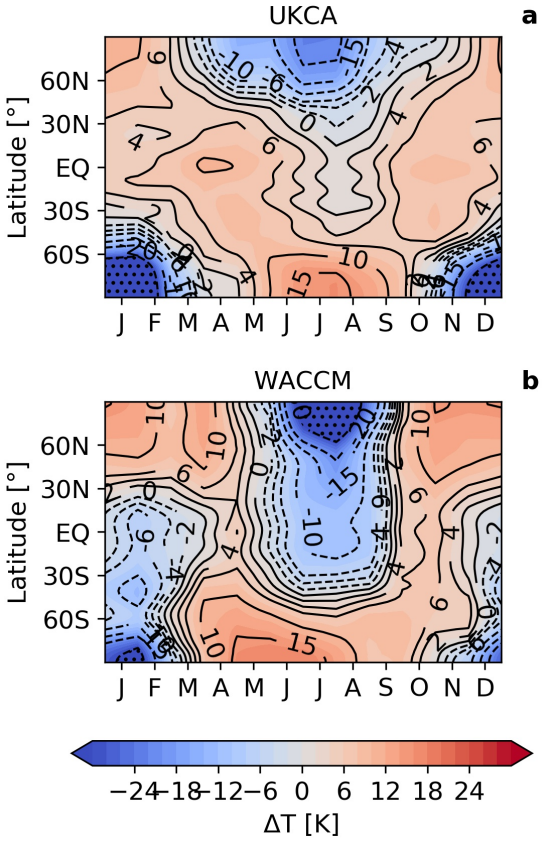

Figure 5.16 Air temperature difference (K) at 90 km from global mean, annual mean value at the same height calculated for (a) UM-UKCA and (b) WACCM as a monthly mean time series. Dotted regions indicate a difference of over -30 K.

Figure 5.17 presents the TEM flow velocities through the MLT for simulations UKCA (panels a and b) and WACCM (panels c and d), calculated based on the method of Smith et al. (2011). Corresponding latitude-pressure cross-sections of air temperature are included in the background of each panel, for reference. As anticipated from the seasonal evolution of the UKCA Na layer, the correct direction of circulation is indeed simulated by UKCA. The models simulate similar magnitudes of downwelling over the winter polar region in both June (strong) and December (weak). Although, the typical upwelling simulated by UKCA over the summer polar regions is

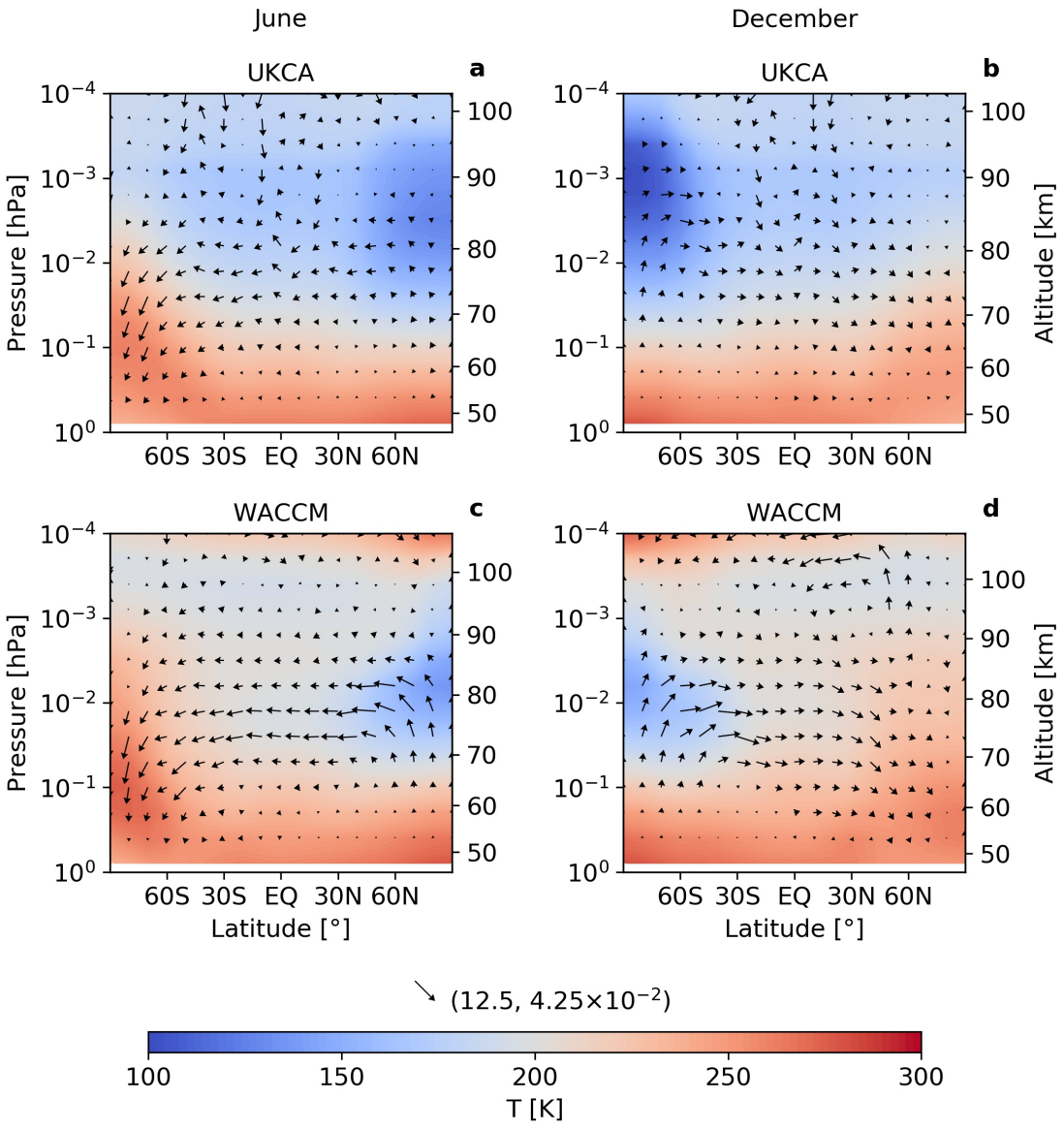

Figure 5.17 Net modelled Transformed Eulerian Mean (TEM) $\bar{v}^*$ and $\bar{w}^*$ wind vectors for (left) June mean and (right) December mean in m s^{-1}, scaled by (x, y) ratio (12.5, 4.25 × 10^{-2}). The background in each panel shows corresponding monthly mean air temperature contours. (a, b) UM-UKCA, (c, d) WACCM.

approximately half the magnitude of WACCM. Similarly, the maximum horizontal component of transport is smaller in UKCA compared to WACCM, by the same factor. This result supports the suggestion of weak meridional winds in UKCA, from the analysis of Figure 5.16.

A striking feature from the TEM flow in UKCA is the strong tropical downwelling above 90 km, simulated in both June and December. This feature is not replicated by WACCM to any extent. It may be explained by the downward reflection of propagating atmospheric waves off the model lid. Large vertical motions in this region are likely to be problematic for the transport of Na through the MLT, as meridional transport will be inhibited. This provides reasoning for why it was necessary to scale down the Na MIF in Extended UM-UKCA simulations by a further factor of ten in order to replicate the observed magnitude of the Na layer. As such, this analysis provides quantitative support for the requirement of Extended UM-UKCA dynamical developments. In particular, the inclusion of eddy diffusion will provide a much-needed source of wave dissipation above the mesopause (Schuchardt and Blum, 1981). Furthermore, this analysis provides evidence that a 120 km altitude limit is not sufficient to avoid the impact of wave reflection from off the model lid. A vertical extension that covers a greater proportion of the MLT, such as the near-140 km model lid height that is used by WACCM, is likely to produce a more suitable model.

5.6 Summary

Meteoric metal layer chemistry has, for the first time, been successfully implemented into UKCA. This was done through the development of an atomic Na diagnostic package, designed to test model performance of chemistry and transport in the MLT. It is expected that a model with an accurate background atmosphere would produce the predicted magnitude and partitioning of each component Na compound. Both the scientific methods devised to create this tool and the analysis of its use on the Extended UM-UKCA configuration developed in Chapter 4 are reported in this chapter.

The efficient Na chemistry scheme available for WACCM simulations (Marsh et al., 2013) was used as a template for the UKCA scheme. However, without an existing mechanism for *in situ* atmospheric particle injection or any representation of

background ion chemistry, UKCA required additional model development work. I configured a mass injection of Na through a 3D chemical emission field, via the adaptation of a recent estimate of the Na particle flux altitude profile. To account for the missing ion chemistry, I developed an Na^+ production parametrisation based on the assumption of 80% NO^+ and 20% O_2^+ relative ionospheric composition in the MLT.

Two Na-augmented Extended UM-UKCA simulations were completed. The first (simulation UKCA), contained an Na injection rate magnitude equivalent to that used in a recent WACCM study that replicated observed peak Na densities (Li et al., 2018). UKCA generates peak Na and Na^+ densities around a factor of ten greater than what is simulated by the WACCM study. The second (simulation UKCA_10), with a tenth of the Na input, shows good agreement with WACCM, displaying near-perfect linear input-to-output scaling for Na and Na^+. Hence, as an initial metric of model performance, it is concluded that the Extended UM-UKCA requires a scaling factor of 50 (ten times larger than the factor of 5 used by WACCM in Li et al. (2018)) in order to simulate the observed *absolute* Na density. Meanwhile, the resulting magnitude of UKCA simulated $NaHCO_3$ was found to approximately scale with the square root of the Na input rate, in agreement with previous studies. Extended UM-UKCA lower-thermospheric densities of $NaHCO_3$ and $Na.CO_2^+$ are disproportionately large compared to other compounds, exceeding the corresponding WACCM densities by factors of up to ten and 1000, respectively. This is largely a signature of imbalances in the partitioning of Na compounds, although the breakdown of the assumption that CO_2 is uniform throughout the atmosphere is a contributing factor in both cases (up to 20% for $NaHCO_3$ and 4% for $Na.CO_2^+$). Hence, highlighting the need to treat CO_2 as a separate tracer in the MLT. Latitude-height cross-sections of UKCA simulated Na reveal a pole-to-equator density gradient, with peak Na densities over the polar regions, while the corresponding WACCM distribution is largely invariant with latitude. This is primarily attributable to O accumulation in the polar regions of UKCA, causing an excessive dissociation of Na compounds back to atomic Na. Above 100 km, UKCA simulates a global mean Na^+:Na ratio typically 2-4 times larger than WACCM. Enhancements of Na^+ are chemically consistent with high levels of O, but a greater rate of Na^+ removal through

chemistry would be expected in the colder UKCA MLT. Transport deficiencies are therefore also likely to contribute to the relative discrepancy.

The altitude at which the Na layer peak occurs is in UKCA, on average, around 3 km below the observed height, but around 2 km above the WACCM generated height. Although the injection of Na into both models is based on the same MIF, the precise height of maximum Na injection is more important in UKCA than it is in WACCM. Unlike UKCA, WACCM contains eddy diffusion, which provides fast vertical transport to adjust the vertical distribution of the Na layer. Therefore, the comparatively better observational agreement of UKCA than WACCM is likely to be partly attributable to the MIF. The fact that UKCA simulates a colder mesopause than WACCM is also likely to be a contributing factor. The observed seasonal evolution of the Na layer is recreated by UKCA to some extent, although limitations in the meridional circulation of the model are exposed. Near the peak of the layer, the UKCA temperature field shows the expected seasonal perturbations over the polar regions, declining towards the tropics. TEM diagnostics reveal that the correct direction of circulation is simulated by UKCA through the MLT, but highlight deficiencies in mesospheric upwelling and meridional transport. Furthermore, UKCA is shown to suffer from the downward reflection of propagating atmospheric waves off the model lid, emphasising both the limitation of a 120 km ceiling and the requirement of eddy diffusion for wave dissipation. An extension of the model lid to at least 140 km, similar to WACCM, is recommended to negate this problem. Finally, the extent of the identified transport deficiencies of the Extended UM-UKCA mean that it is too early in the development program to accurately assess the impact of the model's non-hydrostatic dynamical core on transport in the MLT. However, once the recommended physics have been included, this atomic Na chemistry diagnostic package is available to provide a comprehensive range of tests.

6 AN EXPLANATION FOR THE NITROUS OXIDE LAYER OBSERVED IN THE MESOPAUSE REGION

6.1 Introduction

Observations of atmospheric chemistry are relatively sparse for altitudes above the mesopause (Jackson et al., 2019). Therefore, not all chemical phenomena of the mesosphere-lower thermosphere (MLT) are as well-observed as the atomic sodium layer studied in the previous chapter. Notably, the community is lacking a complete picture of the impact of space weather on the chemistry of the MLT. Motivated by recent satellite measurements from the Atmospheric Chemistry Experiment - Fourier Transform Spectrometer (ACE-FTS), this chapter aims to provide a model explanation for an unexpected layer of enhanced nitrous oxide (N_2O) in the MLT. As discussed in Chapter 2, N_2O was previously assumed to only be produced at the Earth's surface, primarily through bacterial processes in soil (Brasseur and Solomon, 2005). N_2O is an important constituent of the Earth's atmosphere as it is a greenhouse gas and leads to the production of odd nitrogen and other reactive nitrogen compounds (NO_y) that can deplete the ozone (O_3) layer (Ravishankara et al., 2009). The new MLT observations suggest a minor high altitude N_2O production source, most likely attributable to space weather (Sheese et al., 2016). Hence, this study requires a model with a treatment of Energetic Electron Precipitation (EEP). A suitable choice for this is a configuration of the previously mentioned Whole Atmosphere Community Climate Model (WACCM), containing forcing from both auroral and medium-energy electrons (MEE). This chapter describes the development of a novel mechanism and the first model simulations which can explain the formation of this MLT N_2O layer, and was published during the course of my PhD in Geophysical Research Letters (Kelly et al., 2018).

Section 6.2 details the excited molecular nitrogen (N_2) chemistry scheme added to WACCM, highlighting the incorporated N_2O production parametrisation. Section 6.3 describes the WACCM N_2O layer simulations completed for the study. Section 6.4

presents the results from the simulations, with a focus on comparing the magnitude and distribution of the simulated layer to that of the ACE-FTS observations. Control and sensitivity runs are also used in this section to attribute the relative production contributions to specific mechanisms. Section 6.5 summarises my explanation for the source of the observed N_2O layer.

6.2 Excited Nitrogen Chemistry Scheme

As reviewed in Chapter 2, the likely source of N_2O production in the MLT is reaction R2.24a ($N_2(A^3\Sigma_u^+) + O_2 \rightarrow N_2O + O$), where $N_2(A^3\Sigma_u^+)$ is the excited triplet state of N_2. Literature suggests that secondary electron impact from EEP is the leading driver of the required N_2 excitation: reaction R2.23 ($N_2(X^1\Sigma_g^+) + e^- \rightarrow N_2(A^3\Sigma_u^+) + e^-$) (Zipf and Prasad, 1982). By default, WACCM does not contain the $N_2(A^3\Sigma_u^+)$ tracer, hence nor any excitation rate. For this work, I augmented WACCM with the $N_2(A^3\Sigma_u^+)$ tracer, reaction R2.24a (R6.01a) and the other accompanying $N_2(A^3\Sigma_u^+)$ removal reactions (R6.01b-6.05). Each of these is listed in Table 6.1. Rate constants were sourced from Herron (1999) (reactions R6.02-6.04) and Shemansky (1969) (reaction R6.05). The other potential *in situ* atmospheric N_2O production source identified in Chapter 2, reaction R2.25 ($N(^4S) + NO_2 \rightarrow N_2O + O$), was already included in the default configuration of WACCM. The key challenge of this study was to develop a method to parametrise the impact of reaction R6.01a on the N_2O budget in the MLT.

Table 6.1 Chemical reactions added to WACCM for $N_2(A^3\Sigma_u^+)$ chemistry scheme.

Reaction	
$N_2(A^3\Sigma_u^+) + O_2 \rightarrow N_2O + O$	(R6.01a)
$N_2(A^3\Sigma_u^+) + O_2 \rightarrow N_2(X^1\Sigma_g^+) + 2O$	(R6.01b)
$N_2(A^3\Sigma_u^+) + O \rightarrow N_2(X^1\Sigma_g^+) + O$	(R6.02)
$N_2(A^3\Sigma_u^+) + N_2(X^1\Sigma_g^+) \rightarrow 2N_2(X^1\Sigma_g^+)$	(R6.03)
$N_2(A^3\Sigma_u^+) + N(^4S) \rightarrow N_2(X^1\Sigma_g^+) + N(^2P)$	(R6.04)
$N_2(A^3\Sigma_u^+) \rightarrow N_2(X^1\Sigma_g^+) + h\nu$	(R6.05)

6.2.1 Nitrous Oxide Production Parametrisation

Central to this parametrisation is the assumption that in the MLT, the rate of *in situ* N_2O production balances the local chemical loss over a 24-hour period, since N_2O is short-lived (lifetime ~10 days at 95 km) (Brasseur and Solomon, 2005). This means that N_2O is in steady-state on a timescale of days and its production rate P can be set equal to the product of its first-order loss rate L and the observed concentration $[N_2O]_{obs}$

$$\frac{d[N_2O]}{dt} = P - L \cdot [N_2O]_{obs} = 0, \tag{E6.01}$$

where loss occurs through photolysis and reaction with $O(^1D)$. For production, I consider EEP over the polar caps and photoelectrons at all latitudes. Hence,

$$\left(P_{photo} \cdot \alpha\right) + \left(P_{EEP} \cdot \alpha\right) = \left(\left(k_0 \cdot \left[O(^1D)\right]\right) + J_{N_2O}\right) \cdot [N_2O]_{obs}, \tag{E6.02}$$

where P_{photo} is the production rate of $N_2(A^3\Sigma_u^+)$ via photoelectrons, α is the probability that $N_2(A^3\Sigma_u^+)$ reacts with O_2 and makes N_2O via reaction R6.01a, P_{EEP} is the production rate of $N_2(A^3\Sigma_u^+)$ via EEP, k_0 is the rate constant for the reaction between N_2O and $O(^1D)$ (Burkholder et al., 2015), and J_{N_2O} is the photolysis rate of N_2O.

The next task was to estimate the production rates of $N_2(A^3\Sigma_u^+)$ via both photoelectrons (P_{photo}) and EEP (P_{EEP}). The NCAR Global Airglow (GLOW) model (Solomon, 2017) (described in Chapter 3) was used to give a direct estimate for P_{photo} over 2013. The required input parameters for GLOW include the Ap index and F10.7 (solar flux at 10.7 cm), which were taken from the National Oceanic and Atmospheric Administration (NOAA) database. The resulting GLOW model output for the $N_2(A^3\Sigma_u^+)$ production rate was then taken at three-hourly intervals and interpolated onto the WACCM model grid.

P_{EEP} is estimated from EEP ion-pair production rates from both MEE and auroral electrons. The MEE ionisation rate profile is based on measurements from the Medium Energy Proton and Electron Detector (MEPED) instrument, on-board the Polar Orbiting Environmental Satellites (POES) (Lam et al., 2010; Newnham et al., 2018; Orsolini et al., 2018). The auroral electron ionisation rate profile is based on the

parametrisation of Roble and Ridley (1987). Their sum is multiplied by an $N_2(A^3\Sigma_u^+)$ production efficiency factor, β (treated here as independent of altitude in the MLT). That is:

$$P_{EEP} = (I_{MEE} + I_{aur}) \cdot \beta, \tag{E6.03}$$

where I_{MEE} and I_{aur} are the ionisation rates due to MEE and auroral electrons, respectively.

Substituting equation E6.03 into equation E6.02 yields an expression for β

$$\beta = \frac{\left(\left(k_0 \cdot [O(^1D)]\right) + J_{N_2O}\right) \cdot [N_2O]_{obs} - \left(P_{photo} \cdot \alpha\right)}{(I_{MEE} + I_{aur}) \cdot \alpha}. \tag{E6.04}$$

The branching ratio contained inside α is uncertain, with literature estimates ranging from <0.2% (Fraser and Piper, 1989) to 30% (Prasad and Zipf, 2000). To determine an optimal value of this in WACCM-GLOW, I performed test WACCM simulations with only the photoelectron contribution to $N_2(A^3\Sigma_u^+)$ production. Comparison with the observed N_2O in the MLT at low latitudes, where there is no impact from EEP, showed that a branching ratio of 0.5% was consistent with observations around 94.5 km. This value is within the literature range quoted above, and was treated as a constant given that it should be independent of pressure and probably has a weak temperature dependence, since R6.01a and R6.01b are both fast reactions (Zipf and Prasad, 1982). The efficiency factor, β, was estimated using the 100-130 km zonal mean of each variable over the polar regions, as the auroral electron regime is considerably more regular than the MEE regime (a fixed value extrapolation was applied to $[N_2O]_{obs}$ above the satellite retrieval limit). This gave a value of 0.5 (rounded to one decimal place).

Given the importance of I_{MEE} on β, the reliability of the MEE ionisation rate profile calculations are assessed. Firstly, large measurement uncertainty arises from proton contamination during geomagnetic storms and solar proton events (SPEs). However, uncertainty from geomagnetic storms is corrected via the algorithm of Lam et al. (2010) and SPE phases are excluded (Orsolini et al., 2018). However, measurements made over the South Atlantic Magnetic Anomaly (SAA) region contain additional uncertainty due to electron flux enhancements caused by the drift loss cone region

(Newnham et al., 2018). The SAA region is estimated to cause an underestimation in MEE ionisation rates by a factor of ~2-3 in simulations of the Southern Hemisphere (SH) mesosphere. Therefore, since the combined EEP production rate of $N_2(A^3\Sigma_u^+)$ is given by $P_{EEP} = (I_{MEE} + I_{aur})\cdot\beta$, a potential factor 1.5-2 underestimation of the overall EEP induced $N_2(A^3\Sigma_u^+)$ could be anticipated here. However, given that the method used to implement $N_2(A^3\Sigma_u^+)$ production in WACCM for this study was based on a steady-state assumption in the mesosphere, the value for P_{EEP} must be maintained.

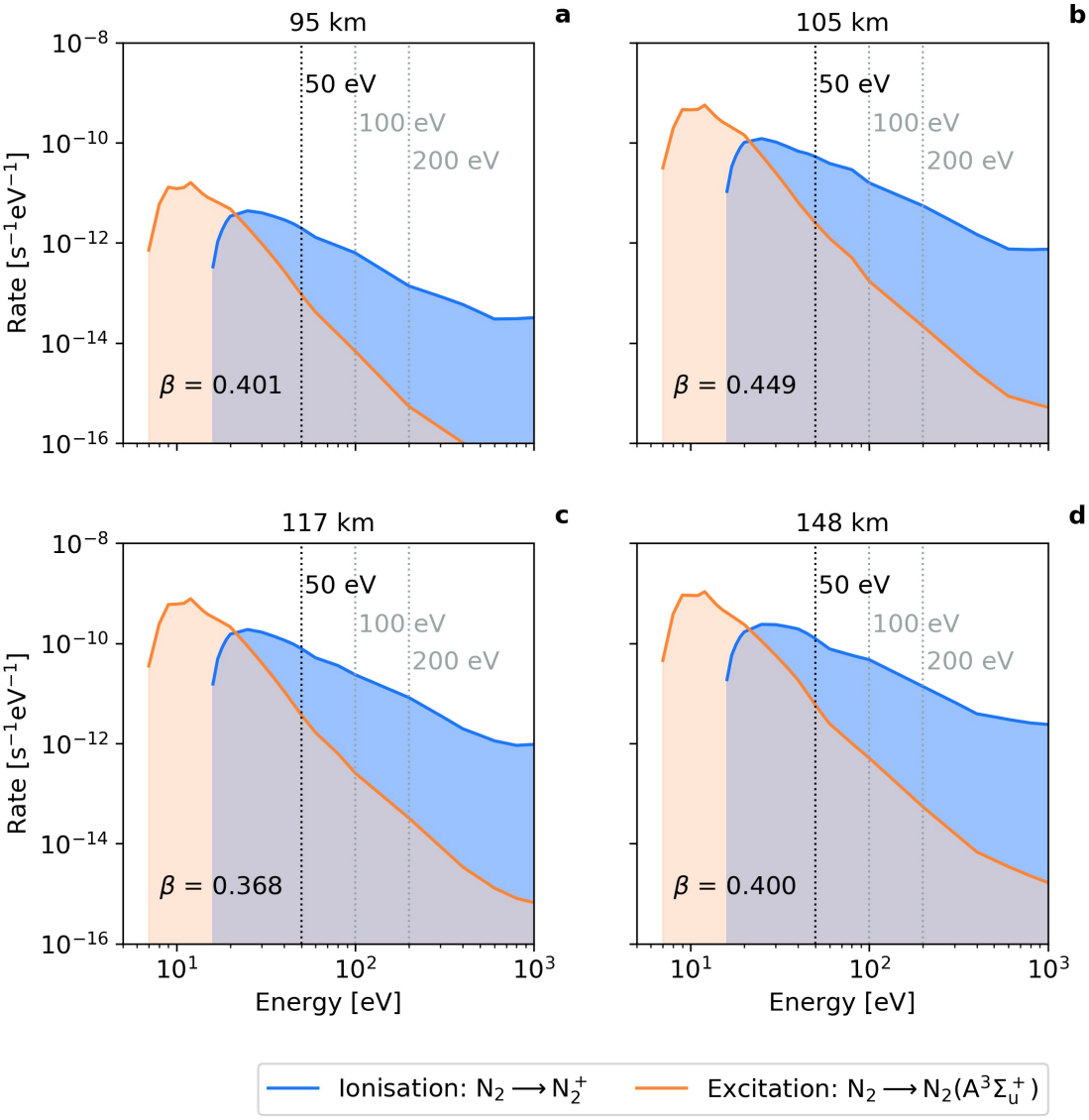

Figure 6.1 First-order energy-dependent rates for the excitation of N_2 to $N_2(A^3\Sigma_u^+)$, and ionisation of N_2 to N_2^+, as a function of electron energy. Panels (a), (b), (c) and (d) show altitudes 95 km, 105 km, 117 km and 148 km, respectively. The efficiency factor β for the proportion of ion-pair production from EEP that leads to $N_2(A^3\Sigma_u^+)$ production was inferred from the ratio of excitation to ionisation + excitations. The values of β for the integration up to 50 eV are given in each panel.

Therefore, a revised calculation of the production efficiency factor β for this I_{MEE} underestimation scenario would yield a smaller value of ~0.25-0.33 (still between 0.1 and 1) to compensate. Hence, there would be no impact on the amount of N_2O produced in model simulations, and conclusions about the relative importance of EEP against photoelectrons would remain the same.

A second estimate of β was carried out through a process based on first principles. This allowed me to compare the two estimates, to i) examine whether the N_2O mixing ratios measured by the ACE-FTS satellite above 90 km seemed physically viable, and to ii) then justify the assumptions made in the original efficiency factor estimate. Data and reasoning from Itikawa (2006), Cartwright et al. (1977), and Banks et al. (1974) were used to make this second estimate. β was estimated here using the integrated cross-section (ICS) for the excitation of N_2 to $N_2(A^3\Sigma_u^+)$, and ionisation to N_2^+, as a function of electron energy (Itikawa, 2006). The excitation ICS was increased by a factor of 3 to account for cascade contributions, as reported by Cartwright et al. (1977). To factor in the electron flux at each energy, the ICS was multiplied by the auroral electron energy distribution spectrum measured by Banks et al. (1974) at various altitudes in the MLT. This gives the electron energy-dependent first-order rates for both excitation and ionisation, shown in Figure 6.1 (a-d) for altitudes of 95, 105, 117 and 148 km, respectively.

Integrating over electron energy up to the limit of typical secondary electron energies (50 eV) provides the fraction of N_2 excitation compared to ionisation + excitation at each altitude, yielding a mean efficiency factor of 0.4 (rounded to 1 decimal place). This compares well to the first estimate of 0.5. To test the sensitivity of the calculation performed in this estimate, I increased the energy limit to 100 eV or 200 eV. Increasing the energy limit lowers the resulting β, as ionisation becomes the increasingly dominant regime above about 20 eV. However, in both of these tests β remained between 0.1 and 1. This indicates that my use of the steady-state assumption to determine β is robust.

6.3 WACCM Set-up

Model simulations were performed using a specified dynamics version of WACCM, as described in Chapter 3. I adapted this WACCM configuration by adding the

$N_2(A^3\Sigma_u^+)$ chemistry scheme based on the reasoning of the previous section. For the study, I completed six separate WACCM simulations with various combinations of N_2O reactions and mechanisms included (see Table 6.2).

Table 6.2 Configurations for WACCM simulations used in this study. Includes simulation with all N_2O production sources switched on (Standard), three control simulations, and two sensitivity runs. All six model simulations were for the whole of 2013.

Simulation/ configuration	$N_2(A^3\Sigma_u^+)$ production via EEP	$N_2(A^3\Sigma_u^+)$ production via photoelectrons	$N_2(A^3\Sigma_u^+) + O_2 \rightarrow N_2O + O$	$N(^4S) + NO_2 \rightarrow N_2O + O$
Standard	On	On	On	On
Control_0	Off	Off	Off	Off
Control_1	On	On	On	Off
Control_2	Off	Off	Off	On
Sensitivity_E	On	Off	On	On
Sensitivity_P	Off	On	On	On

Meteorological variables (wind speed, temperature and surface fluxes) in each simulation were nudged from surface to 50 km, to the NASA Modern-Era Retrospective Analysis for Research and Applications (MERRA) reanalysis data with a 30-minute time-step, as described in Rienecker et al. (2011) and Garcia et al. (2017). Variables were output as monthly means for all of 2013; a solar maximum and a major Sudden Stratospheric Warming (SSW) year. Auroral electrons precipitate almost continuously, however MEE levels are more sporadic as they are associated with geomagnetic storms, which were more frequent in 2013 compared to 2014 (the other year considered in the electron precipitation model of Newnham et al. (2018)). Simulations were run for one year before results were taken to allow for model spin-up. Control simulations 0, 1 and 2 were performed to compare the relative importance of reaction R6.01a against reaction R2.25 on the overall N_2O budget in the MLT. Sensitivity simulations E and P compare the altitude and latitude-dependent contributions of EEP and photoelectrons.

6.4 Nitrous Oxide Layer Simulations

6.4.1 Magnitude and Distribution

Figure 6.2 shows latitude-height plots of the mean N_2O volume mixing ratio (VMR) for 2013, comparing the v3.6 ACE-FTS observations with WACCM simulation Standard (containing all sources), and three selected control and sensitivity simulations: Control_0 (the baseline for other simulations), Sensitivity_E, and Sensitivity_P (see Table 6.2). Plots extend from the stratosphere around 30 km to 140 km in the thermosphere, though the ACE-FTS data only extends up to the satellite retrieval limit around 94.5 km. The WACCM panels are generated from output sampled each time-step at full horizontal resolution (see Chapter 3). It should be noted that this comprehensive sampling is not replicated by ACE-FTS, which is limited by the availability of occultations. The N_2O VMRs for the ACE-FTS plots were calculated using the 5° running mean for each altitude level, as described by Sheese et al. (2016). The white spots and vertical bands in Figures 6.2a and 6.2b indicate where reliable means could not be calculated due to there being no or only one valid occultation in that location and time interval.

Comparing the Standard run (Figures 6.2c and 6.2d) to ACE-FTS (Figures 6.2a and 6.2b) demonstrates firstly that a similar magnitude of N_2O to that observed is simulated near 94.5 km for both seasons (of order 10 ppb), which supports the assumptions made when parametrising the production of $N_2(A^3\Sigma_u^+)$ from EEP and photoelectrons (Section 6.2.1). Secondly, good similarity in the vertical, latitudinal, and seasonal profiles is generally seen between model and satellite. There are two focal points of high N_2O VMRs: the upper stratosphere especially at low latitudes, and the winter poles of the lower thermosphere. Clearly, the majority of stratospheric enhancements can be attributed to surface sources distributed via the Brewer-Dobson circulation (Brewer, 1949; Dobson, 1956) (as described in Chapter 2). In contrast, N_2O above the stratopause is produced *in situ* via reactions R2.25 and R6.01a. The seasonal changes of N_2O in the polar MLT can be explained by the efficiency of N_2O photolysis, the dominant route of removal. The model simulates larger VMRs (up to 40 ppb) with a greater descent over the winter poles, as the lack of sunlight enables N_2O to persist during descent in the polar vortex. Conversely, lower values (around 10 ppb) are found with much less descent over the summer pole where N_2O is readily

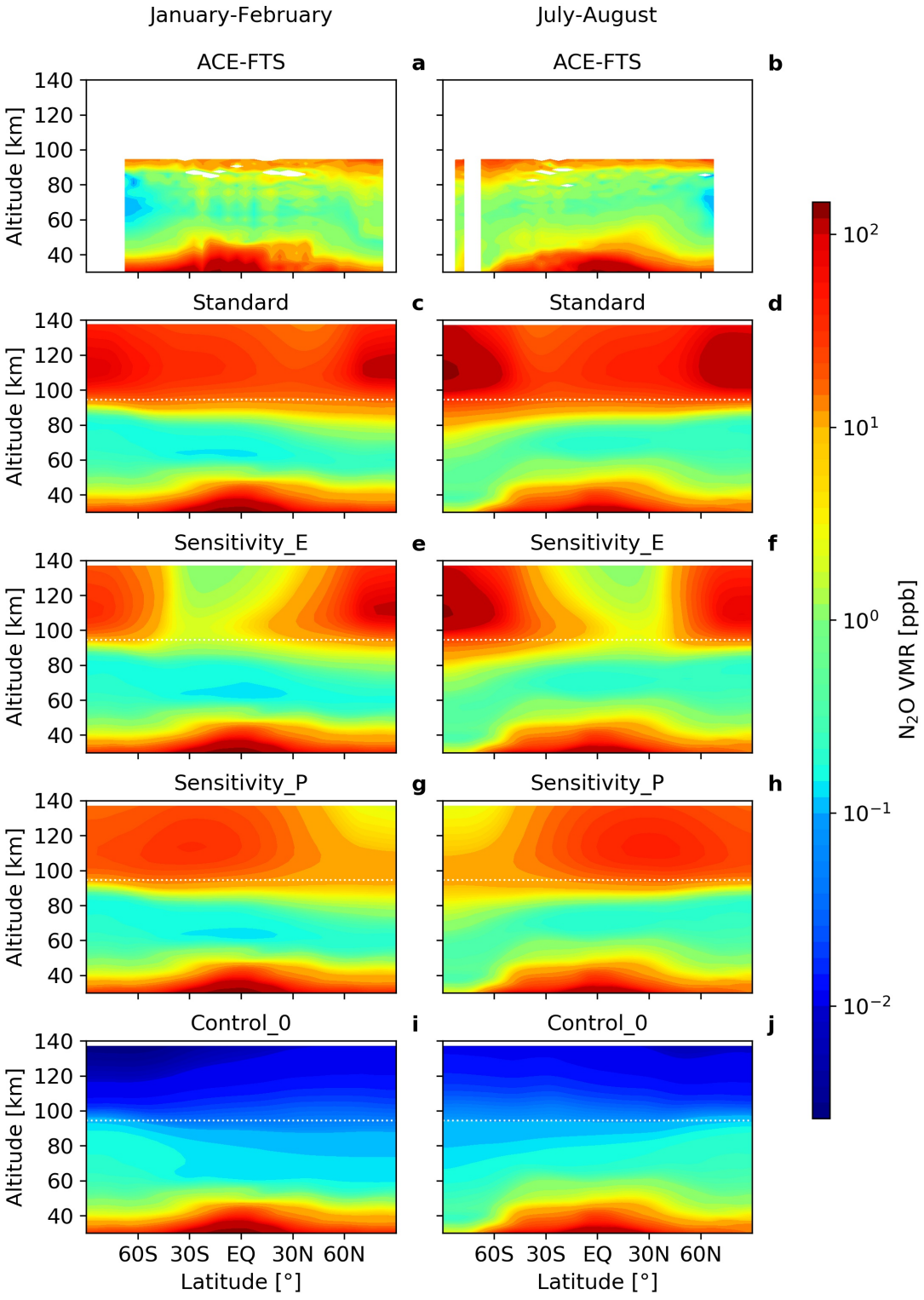

Figure 6.2 Latitude-height zonal mean cross-sections of N_2O VMR (ppb) averaged for (left column) January-February and (right column) July-August. Panels (a) and (b) show ACE-FTS satellite data for 2013 which extends up to 94.5 km. Panels (c)-(j) show four corresponding WACCM simulations (Table 6.2), where each y-axis uses the simulated geopotential height for direct model comparisons. The horizontal dashed white line indicates 94.5 km.

photolysed. Further model-satellite agreement is seen over the extra-polar latitudes of the lower thermosphere, where simulations match the largely uniform N_2O VMRs of 10-20 ppb. The only region showing obvious disagreement is the mesosphere between 60-80 km, particularly over mid-low latitudes, where less N_2O is simulated than observed.

Careful inspection of the ACE-FTS N_2O data (Figures 6.2a and 6.2b) reveals patchy regions of N_2O throughout the mid-low latitude mesosphere, which are not reproduced by WACCM. Instead, a smooth N_2O distribution is simulated across all latitudes over the whole year (Figures 6.2c and 6.2d). Figure 6.3 presents the VMR climatology (2004-2016) of the v3.6 ACE-FTS N_2O data, for the same seasons shown in Figure 6.2. As the climatology is calculated from a much larger dataset than that limited to 2013, the sampling coverage is much improved. In turn, the patchy regions of Figures 6.2a and 6.2b are smoothed out, suggesting that the patchiness can be attributed to sampling frequency. This is supported by the fact that there are typically over a factor of 10 fewer occultations at lower latitudes (as the majority of ACE-FTS measurements are made at high latitudes), combined with a weaker signal at high altitude (Boone et al., 2013). Figure 6.3 provides an update of Figure 2.8 from Chapter 2 (taken from Sheese et al. (2016)), where the v3.5 ACE-FTS climatology (2004-2013) was shown in the same format.

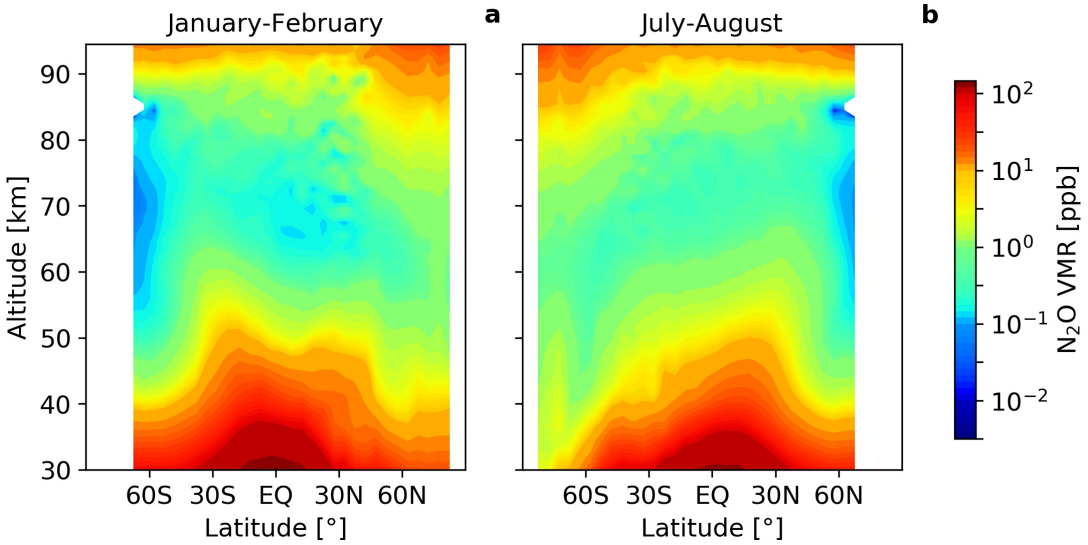

Figure 6.3 Latitude-height zonal mean cross section of ACE-FTS N_2O VMR climatology (2004-2016) for (a) January-February and (b) July-August. The N_2O climatology provides a smoother comparison to model simulations than the limited 2013-only dataset shown in Figure 6.2.

6.4.2 Source Attribution

For a more quantitative comparison of the features discussed above, I compare N_2O VMR profiles averaged over different latitude bands for two seasons (Figure 6.4). From about 80 km upwards, simulation Standard follows the ACE-FTS profile closely for both seasons over all latitude bands. Given that the changes to the model primarily impact the MLT, this indicates that it now successfully captures the observed N_2O enhancements in this region. Interestingly, Control_1 is almost indistinguishable to Standard, meaning that in this altitude range, at least 99% of the N_2O production can be attributed to reaction R6.01a. Reaction R2.25 appears to be largely unimportant outside of mesospheric altitudes below 80 km. However, this mechanism is most prevalent in the Southern Hemisphere (SH) winter pole (Figure 6.4b). Here, a maximum contribution of ~20% is seen from Control_2 close to 60 km. Nevertheless, the remaining N_2O (~80%) is from reaction R6.01a, yielding twice the upper limit suggested by Funke et al. (2008). From the similarity between 2013 and the N_2O VMR climatology (panels (a) and (b) of Figures 6.2 and 6.3), it is likely that these results would be closely replicated in simulations for different years.

Figures 6.4a and 6.4b highlight some apparent systematic differences between the model and satellite measurements. Firstly, at around 60-80 km and 40-60 km for the north and south winter polar vortices, respectively, it appears that the model has a slower N_2O descent rate. This is most severe in the Northern Hemisphere (NH) where the N_2O VMR difference is up to a factor of 4, while it is only up to a factor of 2 in the SH. As this region appears challenging to simulate, it could be used as a future test for assessing model performance. Secondly, larger than measured (~5 times) N_2O VMRs are simulated below about 50 km in the NH. If this is a model problem, it may point to issues in the meridional stratospheric Brewer-Dobson circulation.

As expected from Figure 6.2, in Figures 6.4c-f (which include the mid-low latitudes), simulation Standard typically underestimates the ACE-FTS N_2O by a factor of ~2 between 60-80 km. At this altitude, Semeniuk et al. (2008) suggest that the dominant N_2O production mechanism is reaction R2.25. Therefore, a possible explanation for the shortfall could be that N_2O production via reaction R2.25 is underestimated in the model because the simulated concentration of NO_2 (the source of N_2O in reaction R2.25) is too low. Unfortunately, v3.6 ACE-FTS retrievals of NO_2 do not extend into

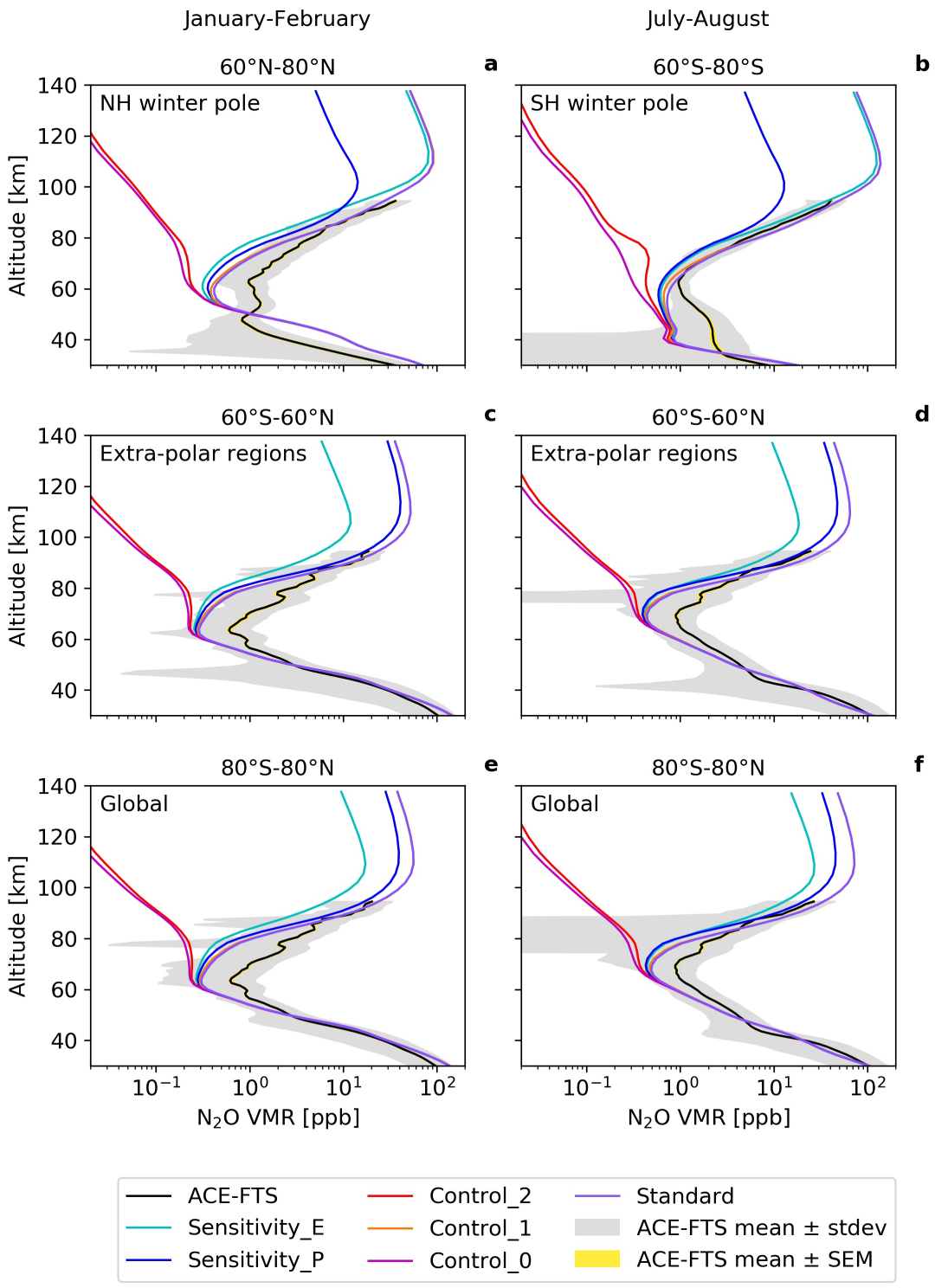

Figure 6.4 Altitude profiles of mean N_2O VMR (ppb) from ACE-FTS observations compared with all six WACCM simulations (Table 6.2) averaged for (left column) January-February and (right column) July-August. The winter poles are shown in panels (a) and (b), the extra-polar regions in (c) and (d), and the global means in (e) and (f). Shaded regions indicate the ACE-FTS uncertainty with standard deviation (grey), and standard error of the mean (SEM) (yellow). Note that the average of the individual profile errors can be on the order 50-200% in the MLT.

the mesosphere, so no direct comparison to the simulation can be made. A deficiency of NO_2 in the mesosphere could arise in WACCM either through underestimated vertical transport of NO_y from the thermosphere or the simplified ion chemistry in the ionospheric *D* region. This could be tested in future work using the very detailed *D* region ion chemistry that is included in recent versions of WACCM (Kovács et al., 2016). Longer simulations with such models could also provide quantification of the impact of upper atmospheric N_2O production on total stratospheric ozone destruction. Based on typical conversion efficiencies of N_2O to NO_y around an SSW event, Sheese et al. (2016) estimate the upper limit of this to be around 2%.

I compare the relative importance of contributions from EEP and photoelectrons to overall N_2O production via reaction R6.01a using the sensitivity simulations. In the polar regions, Figures 6.4a and 6.4b show that above ~90 km Sensitivity_E follows closely to Standard, whereas Sensitivity_P produces a VMR profile that is nearly a factor of 10 lower. This result indicates that almost all N_2O enhancements in the lower thermosphere during polar winter are caused by EEP, which is to be expected since there is very little sunlight to induce photoelectron production. However, there is significant MEE and auroral activity, resulting in large EEP rates. The conclusion that EEP is the principal driver of polar MLT N_2O can also be drawn by comparing Figures 6.2e (6.2f) and 6.2g (6.2h). Figures 6.4c and 6.4d show that the situation in the extra-polar regions above about 90 km is the opposite. Here, the majority of N_2O is produced via photoelectrons, as sunlight is present at mid-low latitudes throughout the year, but there is little incident EEP away from the polar caps (see again the relevant panels in Figure 6.2). The sensitivity simulations thus indicate the importance of including both EEP and photoelectrons in the model. However, photoelectrons appear to be about twice as influential as EEP on the global N_2O budget in the lower thermosphere. This is evidenced most clearly by Figures 6.4e and 6.4f, which show the global mean altitude profiles; VMRs above 90 km from Sensitivity_P are roughly a factor of 2 larger than those from Sensitivity_E.

6.4.3 Solar Cycle Impact

Figure 6.5 shows variations in the ACE-FTS data over the 11-year solar cycle. N_2O retrievals are plotted as annual means for 2008, near solar minimum (Figure 6.5a) and 2014, near solar maximum (Figure 6.5b). These years were selected to avoid the

conflicting dynamical impact that would be found in major SSW years (e.g. 2009 and 2013). Figure 6.5c shows the magnitude of this variation as a percentage difference at solar maximum relative to solar minimum. Below 70 km, the deviations are most likely caused by varying N_2O transport by the Brewer-Dobson circulation over the solar cycle period, rather than the solar cycle itself. However, there is clearly more N_2O observed in the mid-low latitude MLT during solar maximum. Above 70 km there is a typical enhancement of ~10-100%, with values over 100% in some isolated areas. At solar maximum, solar irradiance intensity more than doubles at wavelengths required for photoionisation (<100 nm) (Brasseur and Solomon, 2005). Therefore, such increases could be anticipated from heightened photoelectron fluxes generating additional $N_2(A^3\Sigma_u^+)$ through reaction R2.23. This supports the concept that photoelectrons have an important role in upper atmospheric N_2O production. In contrast, little difference is seen over the polar regions. A slightly

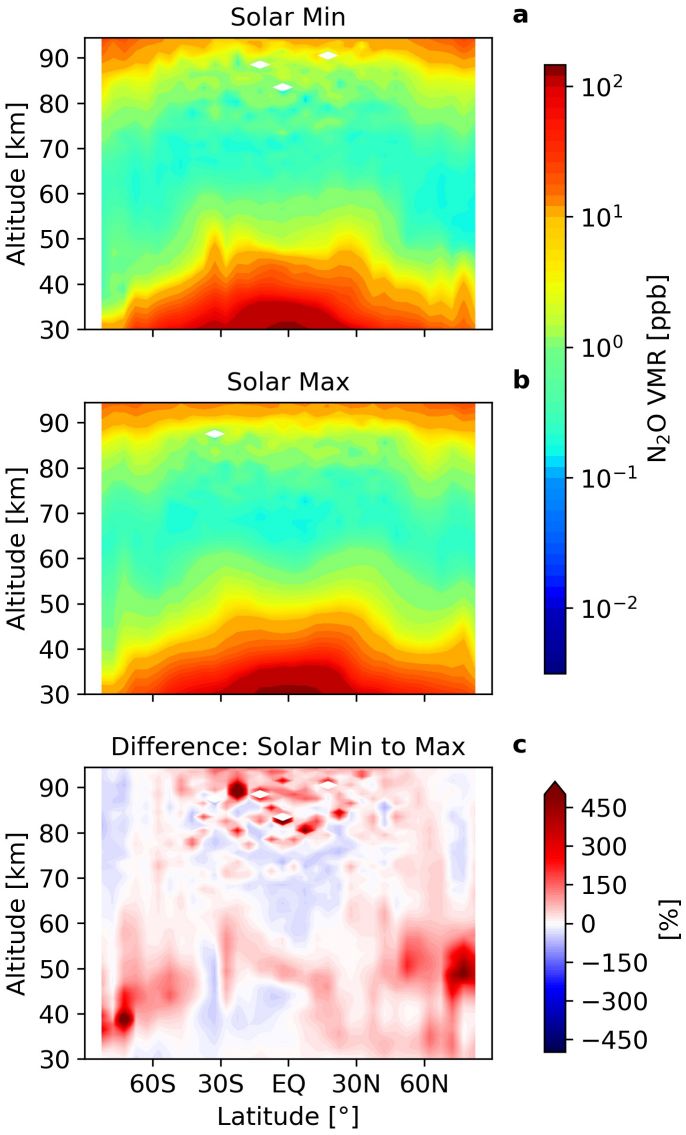

Figure 6.5 Solar cycle comparison: latitude-height zonal mean annual mean cross-sections of ACE-FTS N_2O VMR (ppb) for (a) 2008 near solar minimum and (b) 2014 near solar maximum. Panel (c) shows relative percentage difference at solar maximum with respect to solar minimum, where a +500% limit was applied to saturate anomalies (characteristic of the calculation used on satellite data).

negative deviation is even seen throughout the mesosphere, particularly in the SH. As recorded in the NOAA database, the increase in mean geomagnetic activity levels observed throughout 2014 compared to 2008 was relatively small (~25%). Since EEP is the dominant driver of $N_2(A^3\Sigma_u^+)$ production over the polar regions, the observed smaller solar cycle impact on N_2O concentration at high latitudes compared to mid-low latitudes is therefore expected. One reason for this is that solar minimum and maximum do not necessarily correspond to EEP minimum and maximum, which in this example both fell around a year later. Furthermore, the geomagnetic activity change during this solar cycle was small compared to the typical change (e.g. ~+40% from 1996 to 2001 in the previous cycle).

6.5 Summary

The reaction between $N_2(A^3\Sigma_u^+)$ (produced via collisions between secondary electrons and N_2) and O_2 to form N_2O has been included for the first time in a chemistry-climate model. WACCM simulations provide strong quantitative support for the ACE-FTS observations of N_2O VMR enhancements above 90 km, first reported in Sheese et al. (2016). Essentially all of the N_2O enhancement (>99%) in the MLT occurs through the reaction of $N_2(A^3\Sigma_u^+)$ and O_2. Therefore, its inclusion in future modelling studies is essential for providing a description of N_2O production in the MLT. The reaction between $N(^4S)$ and NO_2 appears to be less important than previously suggested (Funke et al., 2008; Semeniuk et al., 2008), contributing no more than 20% of overall N_2O simulated at any altitude or latitude band in WACCM. However, this may in part be due to mesospheric NO_2 being underestimated in the model, something that could be investigated in a future study using a model with more detailed *D* region ion chemistry.

Latitudinal cross-sections comparing the WACCM simulation against the ACE-FTS measurements generally show a good spatial agreement, and replicate the seasonal N_2O variations observed near the poles. Both EEP and photoelectrons are found to play an important role in the production of $N_2(A^3\Sigma_u^+)$ and ultimately N_2O in the MLT. As expected, EEP is the dominant process near the poles, whereas photoelectrons are most significant in the extra-polar regions, and contribute approximately twice as much as EEP to the global N_2O budget. Analysis of the ACE-FTS data over the

extremes of the 11-year solar cycle show typical N_2O enhancements of ~10-100% during solar maximum, compared to solar minimum. Photoelectrons appear to be the more responsive process here, as the positive deviations are seen over the extra-polar latitudes of the MLT.

The findings from this chapter have provided a suitable explanation for the origins of the second layered phenomena of the MLT studied in this thesis: the N_2O layer. More generally, they have furthered our understanding of how space weather interacts with atmospheric chemistry. My conclusions make an immediate impact on the accepted chemical description of N_2O in the MLT, and in the long-term, promote the case for the search of other space-weather-driven minor chemical production sources.

7 CONCLUSIONS

7.1 Completion of Objectives

The overall objective of this thesis was to further scientific understanding of the chemical and transport properties of layered phenomena in the mesosphere-lower thermosphere (MLT). A key model development task of my PhD, essential to this, was to provide the coupling of the UK Chemistry and Aerosols (UKCA) scheme to an extended altitude configuration of the Met Office Unified Model (Extended UM). Layered phenomena in the MLT are particularly sensitive to temperature and chemistry. Therefore, a detailed review into the current Extended UM-UKCA model performance, focusing on neutral chemistry, was a prerequisite to my investigation of the atomic sodium (Na) layer. The development of individual parametrisations, including those for atomic Na ion production and lower-thermospheric nitrous oxide (N_2O) production, and their inclusion in chemistry-climate model simulations, have enabled various scientific findings in the domain of my overall objective. The following paragraphs of this section address my conclusions with respect to the three specific research questions outlined in Chapter 1.

1. How does the Met Office's chemistry-climate model perform in the MLT and what is the best way to optimise neutral chemistry below the 120 km lid?

As the major influencers on the aeronomy of the MLT, simulated atomic oxygen (O) and atomic hydrogen (H) distributions were the focus of my model performance analysis. However, simulated atmospheric temperature was reviewed prior to this, given the strong temperature dependencies exerted by many of the chemical reactions in the MLT. The Extended UM-UKCA was able to replicate the observed global mean temperature profile around the mesopause, between 90 and 100 km, to within a tolerance of ±3 K when a 25 K increment was added to the prescribed thermospheric climatology. The implementation of extended photolysis treatments for molecular oxygen (O_2) and water vapour (H_2O), based on offline rates, generated H magnitudes that matched reference volume mixing ratios (VMRs) reasonably well, but corresponding O magnitudes were a factor of ten larger than expected. This was

somewhat explained by the fact that O_2 is treated as uniform in UKCA, although diagnostic analysis revealed an accumulation of O near the polar region of the summer hemisphere to be a contributing factor, most likely attributable to transport deficiencies in the model.

I considered the prescription of upper-boundary conditions for O and H through the assessment of the seasonal and inter-annual variation in each species in a long-term Whole Atmosphere Community Climate Model with thermosphere and ionosphere eXtension (WACCM-X) simulation. It was established that a solar-cycle-mean of the data would provide the most suitable treatment at the top level. A robust case was made for the implementation of such treatment for O, while it was concluded that the existing seasonal variation in H was more valuable than the adjustment offered. Simulations containing this development saw an improved representation of O in the lower thermosphere. Estimated chemical heating rate profiles from the Extended UM-UKCA saw generally good agreement with WACCM-X, bar a couple of exceptions. The heating contribution from the recombination of O_2 reaction was around a factor of six higher than WACCM-X at its peak, attributable to the known difference in O magnitudes. Meanwhile, a lack of odd nitrogen (NO_x) in the Extended UM-UKCA, attributable to the absence of energetic particle precipitation (EPP) driven NO_x generation, was found to be the cause of the missing chemical heating contribution from the reaction between N and NO.

2. How does the chemical and physical structure of the background MLT influence the distribution and seasonal evolution of the atomic Na layer?

An atomic Na diagnostic package was developed to test the performance of Extended UM-UKCA chemistry and transport in the MLT. The resulting layer size of each Na compound was found to scale approximately with the Na input rate, aside from $NaHCO_3$, which scaled by the square root of this. Simulations with an Na injection rate equivalent to that used in a recent WACCM study (Li et al., 2018) generated peak atomic Na abundances around a factor of ten greater than the measured values. The known excess of O simulated by the Extended UM-UKCA was found to be a key cause of this, through enhanced dissociation of Na compounds back to atomic Na, based on similarities in the latitudinal distributions of O and Na. As an initial metric of model performance, it was therefore concluded that the Extended UM-UKCA

required an Na input scaling factor of 50 (ten times larger than the factor of 5 used by WACCM in Li et al. (2018)) in order to simulate the observed *absolute* Na density. Above 100 km, the Extended UM-UKCA simulated a global mean Na^+:Na ratio that was typically 2-4 times larger than WACCM. Enhancements of Na^+ are also chemically consistent with high levels of O, but a greater rate of Na^+ removal through chemistry would be expected in the colder MLT of the Extended UM-UKCA. Transport deficiencies were also deemed likely to contribute to the discrepancies simulated in both Na and Na^+. Some imbalances in the partitioning of Na compounds were simulated by the Extended UM-UKCA. Disproportionately large densities of $NaHCO_3$ and $Na.CO_2^+$ were generated in the lower thermosphere, exceeding the corresponding WACCM densities by factors of up to ten and 1000, respectively. The breakdown of the assumption that CO_2 is uniform throughout the atmosphere was found to contribute in both cases (up to 20% for $NaHCO_3$ and 4% for $Na.CO_2^+$).

The altitude of the Na layer peak in Extended UM-UKCA simulations was, on average, around 3 km below the observed height, but around 2 km above the WACCM generated height. The precise height of maximum Na injection was found to be more important in the Extended UM-UKCA than in WACCM, since fast vertical transport provided by eddy diffusion quickly adjusts the vertical distribution of the Na layer in WACCM simulations. The comparatively better observational agreement of the Extended UM-UKCA than WACCM was deemed likely to be partly attributable to the Na input profile, although the fact that the Extended UM-UKCA simulated a colder mesopause than WACCM was also considered to be a likely contributing factor. The observed seasonal evolution of the Na layer was reproduced by the Extended UM-UKCA to some extent, although limitations in the meridional circulation of the model were exposed. Near the peak of the layer, the Extended UM-UKCA temperature field showed the expected seasonal perturbations over the polar regions, but this declined towards the tropics. Transformed Eulerian Mean (TEM) diagnostics confirmed that the correct direction of circulation was simulated by the Extended UM-UKCA through the MLT, but deficiencies in mesospheric upwelling and meridional transport were highlighted. Furthermore, the Extended UM-UKCA was shown to suffer from the downward reflection of propagating atmospheric waves off the model lid, emphasising both the limitation of a 120 km ceiling and the requirement of eddy diffusion for wave dissipation.

3. What is the underlying mechanism behind novel observations of an N_2O layer in the mesopause region?

A parametrisation of N_2O production in the MLT, based on the reaction between $N_2(A^3\Sigma_u^+)$ (produced via collisions between secondary electrons and N_2) and O_2 was developed. This mechanism was included for the first time in a chemistry-climate model. WACCM simulations were completed, designed to determine the principal mechanism for the proposed atmospheric N_2 excitation, and assess the relative overall importance of the new mechanism compared to a competing mechanism (N_2O production via the reaction between $N(^4S)$ and NO_2). Model results provided strong quantitative support for the Atmospheric Chemistry Experiment - Fourier Transform Spectrometer (ACE-FTS) observations of N_2O VMR enhancements above 90 km, first reported in Sheese et al. (2016). Essentially all of the N_2O enhancement (>99%) in the MLT was found to occur through the new mechanism ($N_2(A^3\Sigma_u^+) + O_2$). The reaction between $N(^4S)$ and NO_2 appeared to be less important than previously suggested (Funke et al., 2008; Semeniuk et al., 2008), contributing no more than 20% of overall N_2O simulated at any altitude or latitude band in WACCM. However, it was acknowledged that this may have been in part due to the known underestimation of mesospheric NO_2 in the model. Both Energetic Electron Precipitation (EEP) and photoelectrons were found to play an important role in the production of $N_2(A^3\Sigma_u^+)$ and ultimately N_2O in the MLT. As expected, EEP was the dominant process near the poles, whereas photoelectrons were most significant in the extra-polar regions, and contributed approximately twice as much as EEP to the global N_2O budget.

Synthesis

The results presented in this thesis contribute towards a growing body of evidence that suggests the importance of computationally modelling the MLT and its impact on the lower atmosphere (e.g. Jackson et al. (2019)). In particular, results highlight the extent to which the top boundary of an atmospheric model can impact the chemistry and transport below it; as well as drawing attention to a previously overlooked minor source of stratospheric ozone (O_3) depletion originating from the MLT. More broadly, this work highlights the value gained from coupling chemistry to upper atmospheric models, when used in connection with observations of upper atmospheric chemical species. Original insight into the chemistry and physics of the

MLT is provided in terms of new processes and new modelling tools. It is proven that complicated mechanisms may be appropriately simplified within a chemistry-climate model, to represent key processes in an efficient way (e.g. O_2/H_2O offline photolysis schemes, Na^+ production parametrisation and N_2O steady-state assumption (Kelly et al., 2018)). Minor constituent chemistry should not be overlooked in such models, as Na is shown to be an excellent diagnostic of fundamental chemistry and transport, and N_2O production is shown to be a useful test of atmospheric interactions with EEP.

7.2 Future Work

Recommendations for the direction of future work related to my PhD are made from the results presented in this thesis. These are split into two categories: 'Extended UM-UKCA development priorities' and 'Investigations of particular scientific interest'.

Extended UM-UKCA development priorities

It was clear from the poleward accumulation of O and Na identified in Chapters 4 and 5 that constituent transport needs to be improved in the MLT, as an Extended UM-UKCA development priority. This may be done in part through the inclusion of sub-grid scale physics parametrisations, including eddy diffusion, molecular viscosity and molecular diffusion. A more realistic seasonal temperature gradient through the low latitudes of the MLT will assist meridional transport. This may be provided by direct chemical heating in the MLT, once the chemistry and radiation schemes of the model have been coupled. An extension of the model lid to at least 140 km is recommended to avoid the generation of unphysical downward motions in the MLT, caused by the reflection of propagating atmospheric waves off the model lid.

It was also apparent that some of the chemical approximations used by the model in the stratosphere and lower mesosphere break down in the MLT. For example, O_2 and CO_2 would be better treated as advected tracers in the current model configuration, with the importance of this only increasing in future model iterations with further altitude extensions. The inferred electron density profile from Chapter 5 highlighted the need for the new photoionisation scheme to calculate rates up to an altitude higher than 120 km, when used with the 120 km lid model. This will avoid the severe overestimation of photoionisation originally simulated at the top level. In addition to the upper-boundary conditions discussed in Chapter 4, other top-down forcings also

need to be added to the model. For example, the inclusion of an EPP scheme will provide more realistic NO_x generation in the MLT.

Investigations of particular scientific interest

Recreation of the positive correlation in $\log_{10}(O)$ vs. temperature, identified in WACCM-X data near the mesopause (Chapter 4), may be used as a metric of model performance in the MLT. Pearson correlation coefficients could be recalculated after each future development phase of the Extended UM-UKCA, and be used as a quantitative measure of future chemistry improvements in the MLT. Equally, the factor by which the rate of meteoric input needs to be scaled down by, in order to replicate the observed magnitude of the Na layer in future atomic Na scheme Extended UM-UKCA simulations (Chapter 5), could provide another proxy of model performance. Building on this work, chemistry schemes for other atomic metal layers, such as those of iron (Fe), potassium (K) and calcium (Ca) could also be added to the model. In particular, an atomic K scheme would provide another test of chemistry and transport in the MLT, as differences in the semiannual variations of the K layer and the Na layer have been observed (Plane et al., 2015).

The Na^+ production parametrisation from Chapter 5 may be adapted for use in other chemistry-climate models that do not contain a description of ion chemistry. The parametrisation is not only valid for Na^+, as it can be easily modified to represent the impact of a background ionosphere in any chemical reaction involving O_2^+ or NO^+. This would enable a greater pool of models to be suitable for studies of the MLT. Equally, there is motivation to test the N_2O production parametrisation from Chapter 6 in other models. There is an immediate incentive to first do this using a variant of WACCM with *D* region ion chemistry (WACCM-D) (Verronen et al., 2016). This will enable the impact of mesospheric NO_2 deficiencies on the N_2O budget in the same region to be quantified. It would also be useful to measure the extent to which the findings from the WACCM study are reproducible by models with different dynamical formulations. Furthermore, replication of the observed mesospheric descent rate of N_2O through the polar vortices could be used as another model performance benchmark, as it appeared challenging to simulate with WACCM. It would be of particular interest to test this with a future configuration of the Extended

UM-UKCA, as it may be a feature that is more easily reproducible by a model with a non-hydrostatic dynamical core.

Multiyear simulations containing the N_2O production parametrisation would provide a valuable insight into the wider implications of the newly discovered source. Based on a model climatology, the impact of *in situ* atmospheric N_2O production on stratospheric ozone depletion could be quantified. The potential for there to be contributions to the N_2O layer from other atmospheric processes should also be investigated. For example, Pérez-Invernón et al. (2020) have very recently suggested that sprite streamers may have a role in N_2O production in the MLT, based on results from a 2D model. This could be investigated further through the development of a sprite-induced N_2O production parametrisation for future chemistry-climate model simulations.

REFERENCES

Andersson, M.E., Verronen, P.T., Rodger, C.J., Clilverd, M.A. and Seppälä, A. 2014. Missing driver in the Sun-Earth connection from energetic electron precipitation impacts mesospheric ozone. *Nature Communications.* **5**(5197).

Andrews, D.G. 2000. *An Introduction to Atmospheric Physics*. Cambridge, UK: Cambridge University Press.

Andrews, D.G. and Mcintyre, M.E. 1976. Planetary Waves in Horizontal and Vertical Shear: The Generalized Eliassen-Palm Relation and the Mean Zonal Acceleration. *Journal of the Atmospheric Sciences.* **33**(11), pp.2301-2048.

Archibald, A.T., Connor, F.M., Abraham, N.L., Archer-Nicholls, S., Chipperfield, M.P., Dalvi, M., Folberth, G.A., Dennison, F., Dhomse, S.S., Griffiths, P.T., Hardacre, C., Hewitt, A.J., Hill, R., Johnson, C.E., Keeble, J., Köhler, M.O., Morgenstern, O., Mulchay, J.P., Ordóñez, C., Pope, R.J., Rumbold, S., Russo, M.R., Savage, N., Sellar, A., Stringer, M., Turnock, S., Wild, O. and Zeng, G. 2019. Description and evaluation of the UKCA stratosphere-troposphere chemistry scheme (StratTrop vn 1.0) implemented in UKESM1. *Geoscientific Model Development.* **13**(3), pp.1223-1266.

Arsenovic, P., Rozanov, E., Stenke, A., Funke, B., Wissing, J.M., Mursula, K., Tummon, F. and Peter, T. 2016. The influence of Middle Range Energy Electrons on atmospheric chemistry and regional climate. *Journal of Atmospheric and Solar-Terrestrial Physics.* **149**, pp.180-190.

Atkinson, R., Baulch, D.L., Cox, R.A., Crowley, J.N., Hampson, R.F., Hynes, R.G., Jenkin, M.E., Rossi, M.J. and Troe, J. 2004. Evaluated kinetic and photochemical data for atmospheric chemistry: Volume I – gas phase reactions of Ox, HOx, NOx and SOx species. *Atmospheric Chemistry and Physics.* **4**, pp.1461-1738.

Aulanier, G., Démoulin, P., Schrijver, C.J., Janvier, M., Pariat, E. and Schmieder, B. 2012. The standard flare model in three dimensions - II. Upper limit on solar flare energy. *Astronomy & Astrophysics.* **549**(A66).

Banks, P.M., Chappell, C.R. and Nagy, A.F. 1974. A New Model for the Interaction of Auroral Electrons With the Atmosphere: Spectral Degradation, Backscatter, Optical Emission, and Ionization. *Journal of Geophysical Research.* **79**(10), pp.1459-1470.

Baulch, D.L., Bowman, C.T., Cobos, C.J., Cox, R.A., Just, T., Kerr, J.A., Pilling, M.J., Stocker, D., Troe, J., Tsang, W., Walker, R.W. and Warnatz, J. 2005. Evaluated Kinetic Data for Combustion Modeling: Supplement II. *Journal of Physical and Chemical Reference Data.* **34**(3), pp.757-1397.

Baumgaertner, A.J.G., Jockel, P. and Bruhl, C. 2009. Energetic particle precipitation in ECHAM5/MESSy1 – Part 1: Downward transport of upper atmospheric NOx

produced by low energy electrons. *Atmospheric Chemistry and Physics.* **9**, pp.2729-2740.

Baumgaertner, A.J.G., Seppälä, A., Jöckel, P. and Clilverd, M.A. 2011. Geomagnetic activity related NOx enhancements and polar surface air temperature variability in a chemistry climate model: modulation of the NAM index. *Atmospheric Chemistry and Physics.* **11**, pp.4521-4531.

Bernath, P.F., McElroy, C.T., Abrams, M.C., Boone, C.D., Butler, M., Camy-Peyret, C., Carleer, M., Clerbaux, C., Coheur, P.-F., Colin, R., DeCola, P., DeMazie`re, M., Drummond, J.R., Dufour, D., Evans, W.F.J., Fast, H., Fussen, D., Gilbert, K., Jennings, D.E., Llewellyn, E.J., Lowe, R.P., Mahieu, E., McConnell, J.C., McHugh, M., McLeod, S.D., Michaud, R., Midwinter, C., Nassar, R., Nichitiu, F., Nowlan, C., Rinsland, C.P., Rochon, Y.J., Rowlands, N., Semeniuk, K., Simon, P., Skelton, R., Sloan, J.J., Soucy, M.-A., Strong, K., Tremblay, P., Turnbull, D., Walker, K.A., Walkty, I., Wardle, D.A., Wehrle, V., Zander, R. and Zou, J. 2005. Atmospheric Chemistry Experiment (ACE): Mission overview. *Geophysical Research Letters.* **32**(L15S01).

Bertaux, J.L., Hauchecorne, A., Dalaudier, F., Cot, C., Kyrölä, E., Fussen, D., Tamminen, J., Leppelmeier, G.W., Sofieva, V., Hassinen, S., Fanton d'Andon, O., Barrot, G., Mangin, A., Théodore, B., Guirlet, M., Korablev, O., Snoeij, P., Koopman, R. and Fraisse, R. 2004. First results on GOMOS/ENVISAT. *Advances in Space Research.* **33**, pp.1029-1035.

Bian, H. and Prather, M.J. 2002. Fast-J2: Accurate Simulation of Stratospheric Photolysis in Global Chemical Models. *Journal of Atmospheric Chemistry.* **41**, pp.281-296.

Boone, C.D., Walker, K.A. and Bernath, P.F. 2013. *Version 3 Retrievals for the Atmospheric Chemistry Experiment Fourier Transform Spectrometer (ACE-FTS)*. *The Atmospheric Chemistry Experiment ACE at 10: A Solar Occultation Anthology.* Hampton, Virginia, USA: A. Deepak Publishing.

Bovensmann, H., Burrows, J.P., Buchwitz, M., Frerick, J., Noel, S. and Rozanov, V.V. 1999. SCIAMACHY: Mission Objectives and Measurement Modes. *Journal of the Atmospheric Sciences.* **56**(2), pp.127-150.

Braesicke, P. 2015. *Zonal Mean Climatology*. *Encyclopedia of Atmospheric Sciences.* Vol **4**. 2nd ed. Academic Press.

Brasseur, G.P. and Solomon, S. 2005. *Aeronomy of the Middle Atmosphere: Chemistry and Physics of the Stratosphere and Mesosphere*. 3rd ed. Dordrecht, The Netherlands: Springer.

Brewer, A.W. 1949. Evidence for a world circulation provided by the measurements of helium and water vapour distribution in the stratosphere. *Quarterly Journal of the Royal Meteorological Society.* **75**(326), pp.351-363.

Burkholder, J.B., Sander, S.P., Abbatt, J., Barker, J.R., Huie, R.E., Kolb, C.E., Kurylo, M.J., Orkin, V.L., Wilmouth, D.M. and Wine, P.H. 2015. *Chemical Kinetics and*

Photochemical Data for Use in Atmospheric Studies, Evaluation Number 18. Jet Propulsion Laboratory, Pasadena: JPL Publication 15-10.

Burrows, J.P., Holzle, E., Goede, A.P.H., Visser, H. and Fricke, W. 1995. SCIAMACHY-Scanning Imaging Absorption Spectrometer for Atmospheric Chartography. *Acta Astronautica.* **35**(7), pp.445-451.

Calisto, M., Usoskin, I., Rozanov, E. and Peter, T. 2011. Influence of Galactic Cosmic Rays on atmospheric composition and dynamics. *Atmospheric Chemistry and Physics.* **11**, pp.4547-4556.

Carrillo-Sánchez, J.D., Nesvorný, D., Pokorný, P., Janches, D. and Plane, J.M.C. 2016. Sources of cosmic dust in the Earth's atmosphere. *Geophysical Research Letters.* **43**, pp.11,979-11,986.

Cartwright, D.C., Trajmar, S., Chutjian, A. and Williams, W. 1977. Electron impact excitation of the electronic states of N2. II. Integral cross sections at incident energies from 10 to 50 eV. *Physical Review A.* **16**(3), pp.1041-1051.

Casadio, S., Retscher, C., Lang, R., di Sarra, A., Clemesha, B. and Zehner, C. 2007. *Retrieval of Mesospheric Sodium Densities from SCIAMACHY Daytime Limb Spectra*. Montreux, Switzerland: ESA SP-636.

Chabrillat, S., Kockarts, G., Fonteyn, D. and Brasseur, G. 2002. Impact of molecular diffusion on the CO2 distribution and the temperature in the mesosphere. *Geophysical Research Letters.* **29**(15).

COESA. 1976. *U.S. Standard Atmosphere*. **40**. Washington DC: US Government Printing Office.

Cohen, N.Y., Gerber, E.P. and Bühler, O. 2014. What Drives the Brewer–Dobson Circulation? *Journal of the Atmospheric Sciences.* **71**(10), pp.3837-3855.

COST. 2007. *COST 724 final report: Developing the scientific basis for monitoring, modelling and predicting Space Weather*. Luxembourg: Office for Official Publications of the European Communities.

Crutzen, P.J. 1970. The influence of nitrogen oxides on the atmospheric ozone content. *Quarterly Journal of the Royal Meteorological Society.* **96**(408), pp.320-325.

Crutzen, P.J., Isaksen, I.S.A. and Reid, G.C. 1975. Solar Proton Events: Stratospheric Sources of Nitric Oxide. *Science.* **189**(4201), pp.457-459.

Cullen, M.J.P. 1993. The unified forecast/climate model. *The Meteorological Magazine.* **122**, pp.81-95.

Danabasoglu, G., Lamarque, J.F., Bacmeister, J., Bailey, D.A., DuVivier, A.K., Edwards, J., Emmons, L.K., Fasullo, J., Garcia, R., Gettelman, A., Hannay, C., Holland, M.M., Large, W.G., Lauritzen, P.H., Lawrence, D.M., Lenaerts, J.T.M., Lindsay, K., Lipscomb, W.H., Mills, M.J., Neale, R., Oleson, K.W., Otto-Bliesner, B., Phillips, A.S., Sacks, W., Tilmes, S., Kampenhout, L., Vertenstein, M., Bertini, A., Dennis, J., Deser, C., Fischer, C., Fox-Kemper, B., Kay, J.E., Kinnison, D.,

Kushner, P.J., Larson, V.E., Long, M.C., Mickelson, S., Moore, J.K., Nienhouse, E., Polvani, L., Rasch, P.J. and Strand, W.G. 2020. The Community Earth System Model Version 2 (CESM2). *Journal of Advances in Modeling Earth Systems.* **12**(e2019MS001916).

DeMore, W.B., Sander, S.P., Golden, D.M., Hampson, R.F., Kurylo, M.J., Howard, C.J., Ravishankara, A.R., Kolb, C.E. and Molina, M.J. 1997. *Chemical Kinetics and Photochemical Data for Use in Stratospheric Modeling, Evaluation Number 12*. Jet Propulsion Laboratory, Pasadena: JPL Publication 97-4.

Dobson, G.M.B. 1956. Origin and distribution of the polyatomic molecules in the atmosphere. *Proceedings of the Royal Society A.* **236**, pp.187-193.

Emmert, J.T., Stevens, M.H., Bernath, P.F., Drob, D.P. and Boone, C.D. 2012. Observations of increasing carbon dioxide concentration in Earth's thermosphere. *Nature Geoscience.* **5**, pp.868-871.

Esplin, R., Batty, C., Jensen, M., McLain, D., Stauder, J. and Jensen, S. 1994. SABER instrument overview. *Proceedings of SPIE 2268: 207–17.*

Eyring, V., Bony, S., Meehl, G.A., Senior, C.A., Stevens, B., Stouffer, R.J. and Taylor, K.E. 2016. Overview of the Coupled Model Intercomparison Project Phase 6 (CMIP6) experimental design and organization. *Geoscientific Model Development.* **9**, pp.1937-1958.

Fan, Z.Y., Plane, J.M.C., Gumbel, J., Stegman, J. and Llewellyn, E.J. 2007. Satellite measurements of the global mesospheric sodium layer. *Atmospheric Chemistry and Physics.* **7**, pp.4107-4115.

Feng, W., Marsh, D.R., Chipperfield, M.P., Janches, D., Höffner, J., Yi, F. and Plane, J.M.C. 2013. A global atmospheric model of meteoric iron. *Journal of Geophysical Research: Atmospheres.* **118**, pp.9456-9474.

Fischer, H. and Oelhaf, H. 1996. Remote sensing of vertical profiles of atmospheric trace constituents with MIPAS limb-emission spectrometers. *Applied Optics.* **35**(16), pp.2787-2796.

Fisher, M. and O'Neill, A. 1993. Rapid descent of mesospheric air into the stratospheric polar vortex. *Geophysical Research Letters.* **20**(12), pp.1267-1270.

Fleming, E.L., Chandra, S., Barnett, J.J. and Corney, M. 1990. Zonal mean temperature, pressure, zonal wind and geopotential height as functions of latitude. *Advances in Space Research.* **10**(12), pp.11-59.

Fraser, M.E. and Piper, L.G. 1989. Product Branching Ratios from the $N_2(A^3\Sigma_u^+)$ + O_2 Interaction. *Journal of Physical Chemistry.* **93**(3), pp.1107-1111.

Friederich, M., Gumbel, J. and Pilgrim, R. 1999. Atomic Oxygen in the Mesosphere and its Relevance for the Ionosphere: A Summary of Empirical Evidence. *European Rocket and Balloon Programs and Related Research, Proceedings of the 14th ESA Symposium.* **437**, pp.287-290.

Fritts, D.C. 2015. *Gravity Waves*. *Encyclopedia of Atmospheric Sciences.* Vol **3**. 2nd ed. Academic Press.

Funke, B., Baumgaertner, A., Calisto, M., Egorova, T., Jackman, C.H., Kieser, J., Krivolutsky, A., López-Puertas, M., Marsh, D.R., Reddmann, T., Rozanov, E., Salmi, S.M., Sinnhuber, M., Stiller, G.P., Verronen, P.T., Versick, S., von Clarmann, T., Vyushkova, T.Y., Wieters, N. and Wissing, J.M. 2011. Composition changes after the "Halloween" solar proton event: the High Energy Particle Precipitation in the Atmosphere (HEPPA) model versus MIPAS data intercomparison study. *Atmospheric Chemistry and Physics.* **11**(17), pp.9089-9139.

Funke, B., López-Puertas, M., García-Comas, M., Stiller, G.P., von Clarmann, T. and Glatthor, N. 2008. Mesospheric N_2O enhancements as observed by MIPAS on Envisat during the polar winters in 2002–2004. *Atmospheric Chemistry and Physics Discussions.* **8**(3), pp.10561-10596.

Funke, B., López-Puertas, M., Gil-Lopez, S., von Clarmann, T., Stiller, V.P., Fischer, H. and Kellmann, S. 2005. Downward transport of upper atmospheric NOx into the polar stratosphere and lower mesosphere during the Antarctic 2003 and Arctic 2002/2003 winters. *Journal of Geophysical Research.* **110**(D24308).

Fussen, D., Vanhellemont, F., Tétard, C., Mateshvili, N., Dekemper, E., Loodts, N., Bingen, C., Kyrölä, E., Tamminen, J., Sofieva, V., Hauchecorne, A., Dalaudier, F., Bertaux, J.L., Barrot, G., Blanot, L., Fanton d'Andon, O., Fehr, T., Saavedra, L., Yuan, T. and She, C.Y. 2010. A global climatology of the mesospheric sodium layer from GOMOS data during the 2002–2008 period. *Atmospheric Chemistry and Physics.* **10**(19), pp.9225-9236.

Garcia, R.R., López-Puertas, M., Funke, B., Marsh, D.R., Kinnison, D.E., Smith, A.K. and González-Galindo, F. 2014. On the distribution of CO2 and CO in the mesosphere and lower thermosphere. *Journal of Geophysical Research: Atmospheres.* **119**(9), pp.5700-5718.

Garcia, R.R., Marsh, D.R., Kinnison, D.E., Boville, B.A. and Sassi, F. 2007. Simulation of secular trends in the middle atmosphere, 1950–2003. *Journal of Geophysical Research.* **112**(D09301).

Garcia, R.R., Smith, A.K., Kinnison, D.E., Cámara, Á.d.l. and Murphy, D.J. 2017. Modification of the Gravity Wave Parameterization in the Whole Atmosphere Community Climate Model: Motivation and Results. *Journal of the Atmospheric Sciences.* **74**(1), pp.275-291.

Gardner, C.S., Liu, A.Z. and Guo, Y. 2017. Vertical and horizontal transport of mesospheric Na: Implications for the mass influx of cosmic dust. *Journal of Atmospheric and Solar-Terrestrial Physics.* **162**, pp.192-202.

Gardner, C.S., Plane, J.M.C., Pan, W., Vondrak, T., Murray, B.J. and Chu, X. 2005. Seasonal variations of the Na and Fe layers at the South Pole and their implications for the chemistry and general circulation of the polar mesosphere. *Journal of Geophysical Research.* **110**(D10302).

Gettelman, A., Mills, M.J., Kinnison, D.E., Garcia, R.R., Smith, A.K., Marsh, D.R., Tilmes, S., Vitt, F., Bardeen, C.G., McInerny, J., Liu, H.L., Solomon, S.C., Polvani, L.M., Emmons, L.K., Lamarque, J.F., Richter, J.H., Glanville, A.S., Bacmeister, J.T., Phillips, A.S., Neale, R.B., Simpson, I.R., DuVivier, A.K., Hodzic, A. and Randel, W.J. 2019. The Whole Atmosphere Community Climate Model Version 6 (WACCM6). *Journal of Geophysical Research: Atmospheres.* **124**(23), pp.12380-12403.

Gillan, C.J., Tennyson, J., McLaughlin, B.M. and Burke, P.G. 1996. Low-energy electron impact excitation of the nitrogen molecule: optically forbidden transitions. *Journal of Physics B: Atomic, Molecular and Optical Physics.* **29**(8), pp.1531-1547.

González, M., Miquel, I. and Sayós, R. 2001. VTST kinetics study of the N(2D)+O2(X3Σg-) → NO(X2Π)+O(3P,1D) reactions based on CASSCF and CASPT2 ab initio calculations including excited potential energy surfaces. *Chemical Physics Letters.* **335**(3-4), pp.339-347.

Gordon, W.E. 1958. Incoherent Scattering of Radio Waves by Free Electrons with Applications to Space Exploration by Radar. *Proceedings of the IRE.* **46**(11), pp.1824-1829.

Grebowsky, J.M., Goldberg , R.A. and Pesnell, W.D. 1998. Do meteor showers significantly perturb the ionosphere? *Journal of Atmospheric and Solar-Terrestrial Physics.* **60**, pp.607-615.

Griffin, D.J. and Thuburn, J. 2018. Numerical effects on vertical wave propagation in deep-atmosphere models. *Quarterly Journal of the Royal Meteorological Society.* **144**(711), pp.567-580.

Griffith, M.J., Jackson, D.R., Griffin, D.J. and Budd, C.J. 2020. Stable extension of the unified model into the mesosphere and lower thermosphere. *Journal of Space Weather and Space Climate.* **10**(19).

Gumbel, J., Fan, Z.Y., Waldemarsson, T., Stegman, J., Witt, G., Llewellyn, E.J., She, C.Y. and Plane, J.M.C. 2007. Retrieval of global mesospheric sodium densities from the Odin satellite. *Geophysical Research Letters.* **34**(L04813).

Hagan, M.E., Roble, R.G. and Hackney, J. 2001. Migrating thermospheric tides. *Journal of Geophysical Research.* **106**(A7), pp.12739-12752.

Hapgood, M. 2017. *Space Weather*. Bristol, UK: IOP Publishing.

Harper, A.B., Wiltshire, A.J., Cox, P.M., Friedlingstein, P., Jones, C.D., Mercado, L.M., Sitch, S., Williams, K. and Duran-Rojas, C. 2018. Vegetation distribution and terrestrial carbon cycle in a carbon cycle configuration of JULES4.6 with new plant functional types. *Geoscientific Model Development.* **11**(7), pp.2857-2873.

Harry, G. 2015. *Stabilising and Validating the Met Office's Unified Model with 100 and 120 km Ceilings*. Master's thesis, University of Bath.

Hedin, A.E. and Mayr, H.G. 1987. Solar EUV Induced Variations in the Thermosphere. *Journal of Geophysical Research.* **92**(D1), pp.869-875.

Hedin, A.E., Salah, J.E., Evans, J.V., Reber, C.A., Newton, G.P., Spencer, N.W., Kayser, D.C., Alcaydé, D., Bauer, P., Cogger, L. and McClure, J.P. 1977. A global thermospheric model based on mass spectrometer and incoherent scatter data MSIS, 1. N2 density and temperature. *Journal of Geophysical Research.* **82**(16), pp.2139-2147.

Hedin, J. and Gumbel, J. 2011. The global mesospheric sodium layer observed by Odin/OSIRIS in 2004–2009. *Journal of Atmospheric and Solar-Terrestrial Physics.* **73**(14-15), pp.2221-2227.

Herrmann, A., Schumacher, E. and Wöste, L. 1978. Preparation and photoionization potentials of molecules of sodium, potassium, and mixed atoms. *The Journal of Chemical Physics.* **68**(5), pp.2327-2336.

Herron, J.T. 1999. Evaluated Chemical Kinetics Data for Reactions of $N(^2D)$, $N(^2P)$, and $N_2(A^3\Sigma_u^+)$ in the Gas Phase. *Journal of Physical and Chemical Reference Data.* **28**(5), pp.1453-1483.

Hurrell, J.W., Holland, M.M., Gent, P.R., Ghan, S., Kay, J.E., Kushner, P.J., Lamarque, J.-F., Large, W.G., Lawrence, D., Lindsay, K., Lipscomb, W.H., Long, M.C., Mahowald, N., Marsh, D.R., Neale, R.B., Rasch, P., Vavrus, S., Vertenstein, M., Bader, D., Collins, W.D., Hack, J.J., Kiehl, J. and Marshall, S. 2013. The Community Earth System Model: A Framework for Collaborative Research. *Bulletin of the American Meteorological Society.* **94**(9), pp.1339-1360.

Immel, T.J., Sagawa, E., England, S.L., Henderson, S.B., Hagan, M.E., Mende, S.B., Frey, H.U., Swenson, C.M. and Paxton, L.J. 2006. Control of equatorial ionospheric morphology by atmospheric tides. *Geophysical Research Letters.* **33**(L15108).

Ineson, S., Scaife, A.A., Knight, J.R., Manners, J.C., Dunstone, N.J., Gray, L.J. and Haigh, J.D. 2011. Solar forcing of winter climate variability in the Northern Hemisphere. *Nature Geoscience.* **4**(11), pp.753-757.

IPCC. 2014. *Climate Change 2014: Synthesis Report. Contribution of Working Groups I, II and III to the Fifth Assessment Report of the Intergovernmental Panel on Climate Change*. Geneva, Switzerland: IPCC.

Itikawa, Y. 2006. Cross Sections for Electron Collisions with Nitrogen Molecules. *Journal of Physical and Chemical Reference Data.* **35**(1), pp.31-53.

Jackman, C.H., Marsh, D.R., Kinnison, D.E., Mertens, C.J. and Fleming, E.L. 2016. Atmospheric changes caused by galactic cosmic rays over the period 1960–2010. *Atmospheric Chemistry and Physics.* **16**(9), pp.5853-5866.

Jackman, C.H., McPeters, R.D., Labow, G.J., Fleming, E.L., Praderas, C.J. and Russell, J.M. 2001. Northern hemisphere atmospheric effects due to the July 2000 Solar Proton Event. *Geophysical Research Letters.* **28**(15), pp.2883-2886.

Jackson, D.R., Fuller-Rowell, T.J., Griffin, D.J., Griffith, M.J., Kelly, C.W., Marsh, D.R. and Walach, M.T. 2019. Future Directions for Whole Atmosphere Modeling: Developments in the Context of Space Weather. *Space Weather.* **17**(9), pp.1342-1350.

Janches, D., Heinselman, C.J., Chau, J.L., Chandran, A. and Woodman, R. 2006. Modeling the global micrometeor input function in the upper atmosphere observed by high power and large aperture radars. *Journal of Geophysical Research.* **111**(A07317).

Karpechko, A.Y., Hitchcock, P., Peters, D.H.W. and Schneidereit, A. 2017. Predictability of downward propagation of major sudden stratospheric warmings. *Quarterly Journal of the Royal Meteorological Society.* **143**(704), pp.1459-1470.

Kato, S. 1962. Joule Heating and Temperature in the Upper Atmosphere. *Planetary and Space Science.* **9**, pp.939-946.

Keeble, J., Bednarz, E.M., Banerjee, A., Abraham, N.L., Harris, N.R.P., Maycock, A.C. and Pyle, J.A. 2017. Diagnosing the radiative and chemical contributions to future changes in tropical column ozone with the UM-UKCA chemistry–climate model. *Atmospheric Chemistry and Physics.* **17**(22), pp.13801-13818.

Kelley, M.C. 2009. *The Earth's Ionosphere: Plasma Physics and Electrodynamics*. 2nd ed. Academic Press.

Kelley, M.C. 2015. *Ionosphere*. *Encyclopedia of Atmospheric Sciences.* Vol **3**. 2nd ed. Academic Press.

Kelly, C.W., Chipperfield, M.P., Plane, J.M.C., Feng, W., Sheese, P.E., Walker, K.A. and Boone, C.D. 2018. An Explanation for the Nitrous Oxide Layer Observed in the Mesopause Region. *Geophysical Research Letters.* **45**(15), pp.7818–7827.

Kinnison, D.E., Brasseur, G.P., Walters, S., Garcia, R.R., Marsh, D.R., Sassi, F., Harvey, V.L., Randall, C.E., Emmons, L., Lamarque, J.F., Hess, P., Orlando, J.J., Tie, X.X., Randel, W., Pan, L.L., Gettelman, A., Granier, C., Diehl, T., Niemeier, U. and Simmons, A.J. 2007. Sensitivity of chemical tracers to meteorological parameters in the MOZART-3 chemical transport model. *Journal of Geophysical Research.* **112**(D20302).

Knipp, D.J., Pette, D.V., Kilcommons, L.M., Isaacs, T.L., Cruz, A.A., Mlynczak, M.G., Hunt, L.A. and Lin, C.Y. 2017. Thermospheric nitric oxide response to shock-led storms. *Space Weather.* **15**, pp.325-342.

Kopp, E. 1997. On the abundance of metal ions in the lower ionosphere. *Journal of Geophysical Research.* **102**(A5), pp.9667-9674.

Kopp, E., Andre, L. and Smith, L.G. 1985. Positive ion composition and derived particle heating in the lower auroral ionosphere. *Journal of Atmospheric and Terriestrial Physics.* **47**(1-3), pp.301-308.

Kopp, E., Eberhardt, P. and Herrmann, U. 1985. Positive Ion Composition of the High-Latitude Summer D Region With Noctilucent Clouds. *Journal of Geophysical Research.* **90**(D7), pp.13041-13053.

Kopp, E. and Herrmann, U. 1984. Ion composition in the lower ionosphere. *Annales Geophysicae.* **2**(1), pp.83-94.

Kopp, E., Ramseyer, H. and Bjorn, L.G. 1984. Positive Ion Composition and Electron Density in a Combined Auroral and NLC Event. *Advances in Space Research.* **4**(4), pp.157-161.

Kovács, T., Plane, J.M.C., Feng, W., Nagy, T., Chipperfield, M.P., Verronen, P.T., Andersson, M.E., Newnham, D.A., Clilverd, M.A. and Marsh, D.R. 2016. D-region ion–neutral coupled chemistry (Sodankylä Ion Chemistry, SIC) within the Whole Atmosphere Community Climate Model (WACCM 4) – WACCM-SIC and WACCM-rSIC. *Geoscientific Model Development.* **9**, pp.3123-3136.

Kyrölä, E., Tamminen, J., Leppelmeier, G.W., Sofieva, V., Hassinen, S., Bertaux, J.L., Hauchecorne, A., Dalaudier, F., Cot, C., Korablev, O., Fanton d'Andon, O., Barrot, G., Mangin, A., Théodore, B., Guirlet, M., Etanchaud, F., Snoeij, P., Koopman, R., Saavedra, L., Fraisse, R., Fussen, D. and Vanhellemont, F. 2004. GOMOS on Envisat: an overview. *Advances in Space Research.* **33**(7), pp.1020-1028.

Lam, M.M., Horne, R.B., Meredith, N.P., Glauert, S.A., Moffat-Griffin, T. and Green, J.C. 2010. Origin of energetic electron precipitation >30 keV into the atmosphere. *Journal of Geophysical Research.* **115**(A00F08).

Lary, D.J. and Pyle, J.A. 1991. Diffuse radiation, twilight, and photochemistry — I. *Journal of Atmospheric Chemistry.* **13**(4), pp.373-392.

Lee, K.H., Li, Z., Kim, Y.J. and Kokhanovsky, A. 2009. *Atmospheric Aerosol Monitoring from Satellite Observations: A History of Three Decades*. *Atmospheric and Biological Environmental Monitoring.* Dordrecht: Springer.

Li, T., Ban, C., Fang, X., Li, J., Wu, Z., Feng, W., Plane, J.M.C., Xiong, J., Marsh, D.R., Mills, M.J. and Dou, X. 2018. Climatology of mesopause region nocturnal temperature, zonal wind and sodium density observed by sodium lidar over Hefei, China (32° N, 117° E). *Atmospheric Chemistry and Physics.* **18**(16), pp.11683-11695.

Liu, H.L., Bardeen, C.G., Foster, B.T., Lauritzen, P., Liu, J., Lu, G., Marsh, D.R., Maute, A., McInerney, J.M., Pedatella, N.M., Qian, L., Richmond, A.D., Roble, R.G., Solomon, S.C., Vitt, F.M. and Wang, W. 2018. Development and Validation of the Whole Atmosphere Community Climate Model With Thermosphere and Ionosphere Extension (WACCM-X 2.0). *Journal of Advances in Modeling Earth Systems.* **10**(2), pp.381-402.

Liu, H.L., Foster, B.T., Hagan, M.E., McInerney, J.M., Maute, A., Qian, L., Richmond, A.D., Roble, R.G., Solomon, S.C., Garcia, R.R., Kinnison, D., Marsh, D.R., Smith, A.K., Richter, J., Sassi, F. and Oberheide, J. 2010. Thermosphere extension of the Whole Atmosphere Community Climate Model. *Journal of Geophysical Research.* **115**(A12302).

Llewellyn, E.J., Degenstein, D.A., Lloyd, N.D., Gattinger, R.L., Petelina, S., McDade, I.C., Haley, C.S., Solheim, B.H., von Savigny, C., Sioris, C., Evans, W.F.J., Strong, K., Murtagh, D.P. and Stegman, J. 2003. First Results from the OSIRIS Instrument on-board Odin. *Sodankyla Geophysical Observatory Publications.* **92**, pp.41-47.

Llewellyn, E.J., Lloyd, N.D., Degenstein, D.A., Gattinger, R.L., Petelina, S.V., Bourassa, A.E., Wiensz, J.T., Ivanov, E.V., McDade, I.C., Solheim, B.H., McConnell,

J.C., Haley, C.S., von Savigny, C., Sioris, C.E., McLinden, C.A., Griffioen, E., Kaminski, J., Evans, W.F.J., Puckrin, E., Strong, K., Wehrle, V., Hum, R.H., Kendall, D.J.W., Matsushita, J., Murtagh, D.P., Brohede, S., Stegman, J., Witt, G., Barnes, G., Payne, W.F., Piché, L., Smith, K., Warshaw, G., Deslauniers, D.L., Marchand, P., Richardson, E.H., King, R.A., Wevers, I., McCreath, W., Kyrölä, E., Oikarinen, L., Leppelmeier, G.W., Auvinen, H., Mégie, G., Hauchecorne, A., Lefèvre, F., de La Nöe, J., Ricaud, P., Frisk, U., Sjoberg, F., von Schéele, F. and Nordh, L. 2004. The OSIRIS instrument on the Odin spacecraft. *Canadian Journal of Physics.* **82**(6), pp.411-422.

Lockwood, M., Owens, M.J., Barnard, L., Davis, C.J. and Thomas, S. 2012. Solar Cycle 24: what is the Sun up to? *Astronomy & Geophysics.* **53**.

Lu, H., Jarvis, M.J. and Hibbins, R.E. 2008. Possible solar wind effect on the northern annular mode and northern hemispheric circulation during winter and spring. *Journal of Geophysical Research.* **113**(D23104).

Manney, G.L., Kruger, K., Sabutis, J.L., Sena, S.A. and Pawson, S. 2005. The remarkable 2003–2004 winter and other recent warm winters inthe Arctic stratosphere since the late 1990s. *Journal of Geophysical Research.* **110**(D04107).

Manney, G.L., Schwartz, M.J., Krüger, K., Santee, M.L., Pawson, S., Lee, J.N., Daffer, W.H., Fuller, R.A. and Livesey, N.J. 2009. Aura Microwave Limb Sounder observations of dynamics and transport during the record-breaking 2009 Arctic stratospheric major warming. *Geophysical Research Letters.* **36**(L12815).

Marsh, D.R., Garcia, R.R., Kinnison, D.E., Boville, B.A., Sassi, F., Solomon, S.C. and Matthes, K. 2007. Modeling the whole atmosphere response to solar cycle changes in radiative and geomagnetic forcing. *Journal of Geophysical Research.* **112**(D23306).

Marsh, D.R., Janches, D., Feng, W. and Plane, J.M.C. 2013. A global model of meteoric sodium. *Journal of Geophysical Research: Atmospheres.* **118**(19), pp.11,442-11,452.

Marsh, D.R., Mills, M.J., Kinnison, D.E., Lamarque, J.-F., Calvo, N. and Polvani, L.M. 2013. Climate Change from 1850 to 2005 Simulated in CESM1(WACCM). *Journal of Climate.* **26**, pp.7372-7391.

Martin, J.J. 1965. Evaluation of the Atmospheric Density Scale Height. *Journal of Geophysical Research.* **70**(20), pp.5328-5329.

McElroy, M.B., Salawitch, R.J. and Minschwaner, K. 1992. The Changing Stratosphere. *Planetary and Space Science.* **40**(2-3), pp.373-401.

McInerney, J.M., Marsh, D.R., Liu, H.-L., Solomon, S.C., Conley, A.J. and Drob, D.P. 2018. Simulation of the 21 August 2017 Solar Eclipse Using the Whole Atmosphere Community Climate Model-eXtended. *Geophysical Research Letters.* **45**(9), pp.3793-3800.

McNeil, W.J., Murad, E. and Lai, S.T. 1995. Comprehensive model for the atmospheric sodium layer. *Journal of Geophysical Research.* **100**(D8), pp.16847-16855.

Mills, M.J., Schmidt, A., Easter, R., Solomon, S., Kinnison, D.E., Ghan, S.J., Neely, R.R., Marsh, D.R., Conley, A., Bardeen, C.G. and Gettelman, A. 2016. Global volcanic aerosol properties derived from emissions, 1990-2014, using CESM1(WACCM). *Journal of Geophysical Research: Atmospheres.* **121**(5), pp.2332-2348.

Mlynczak, M.G. 1997. Energetics of the Mesosphere and Lower Thermosphere and the SABER Experiment. *Advances in Space Research.* **20**(6), pp.1177-1183.

Mlynczak, M.G. and Hunt, L.A. 2015. *Atomic Species in the Mesopause Region*. *Encyclopedia of Atmospheric Sciences.* Vol **3**. 2nd ed. Academic Press.

Mlynczak, M.G. and Solomon, S. 1993. A Detailed Evaluation of the Heating Efficiency in the Middle Atmosphere. *Journal of Geophysical Research.* **98**(D6), pp.10517-10541.

Monks, P.S., Archibald, A.T., Colette, A., Cooper, O., Coyle, M., Derwent, R., Fowler, D., Granier, C., Law, K.S., Mills, G.E., Stevenson, D.S., Tarasova, O., Thouret, V., von Schneidemesser, E., Sommariva, R., Wild, O. and Williams, M.L. 2015. Tropospheric ozone and its precursors from the urban to the global scale from air quality to short-lived climate forcer. *Atmospheric Chemistry and Physics.* **15**(15), pp.8889-8973.

Morgenstern, O., Braesicke, P., O'Connor, F.M., Bushell, A.C., Johnson, C.E., Osprey, S.M. and Pyle, J.A. 2009. Evaluation of the new UKCA climate-composition model – Part 1: The stratosphere. *Geoscientific Model Development.* **2**, pp.43-57.

Mulcahy, J.P., Jones, C., Sellar, A., Johnson, B., Boutle, I.A., Jones, A., Andrews, T., Rumbold, S.T., Mollard, J., Bellouin, N., Johnson, C.E., Williams, K.D., Grosvenor, D.P. and McCoy, D.T. 2018. Improved Aerosol Processes and Effective Radiative Forcing in HadGEM3 and UKESM1. *Journal of Advances in Modeling Earth Systems.* **10**(11), pp.2786-2805.

Nagy, A.F. and Banks, P.M. 1970. Photoelectron Fluxes in the Ionosphere. *Journal of Geophysical Research: Space Physics.* **75**(31), pp.6260-6270.

Newnham, D.A., Clilverd, M.A., Rodger, C.J., Hendrickx, K., Megner, L., Kavanagh, A.J., Seppälä, A., Verronen, P.T., Andersson, M.E., Marsh, D.R., Kovács, T., Feng, W. and Plane, J.M.C. 2018. Observations and modelling of increased nitric oxide in the Antarctic polar middle atmosphere associated with geomagnetic storm driven energetic electron precipitation. *Journal of Geophysical Research: Space Physics.* **123**, pp.6009-6025.

Nisbet, J.S. 1967. Neutral Atmospheric Temperatures from Incoherent Scatter Observations. *Journal of the Atmospheric Sciences.* **24**(5), pp.586-593.

O'Connor, F.M., Johnson, C.E., Morgenstern, O., Abraham, N.L., Braesicke, P., Dalvi, M., Folberth, G.A., Sanderson, M.G., Telford, P.J., Voulgarakis, A., Young,

P.J., Zeng, G., Collins, W.J. and Pyle, J.A. 2014. Evaluation of the new UKCA climate-composition model – Part 2: The Troposphere. *Geoscientific Model Development.* **7**(1), pp.41-91.

Offermann, D. 1985. The Energy Budget Campaign 1980: introductory review. *Journal of Atmospheric and Terriestrial Physics.* **47**(1-3), pp.1-26.

Offermann, D., Friederich, P.R. and von Zahn, U. 1981. Neutral Gas Composition Measurements Between 80 and 120 km. *Planetary and Space Science.* **29**(7), pp.747-764.

Orsolini, Y.J., Smith-Johnsen, C., Marsh, D.R., Stordal, F., Rodger, C.J., Verronen, P.T. and Clilverd, M.A. 2018. Mesospheric nitric acid enhancements during energetic electron precipitation events simulated by WACCM-D. *Journal of Geophysical Research: Atmospheres.* **123**, pp.6984-6998.

Pérez-Invernón, F.J., Malagón-Romero, A., Gordillo-Vázquez, F.J. and Luque, A. 2020. The Contribution of Sprite Streamers to the Chemical Composition of the Mesosphere-Lower Thermosphere. *Geophysical Research Letters.* **47**(e2020GL088578).

Picone, J.M., Hedin, A.E., Drob, D.P. and Aikin, A.C. 2002. NRLMSISE-00 empirical model of the atmosphere: Statistical comparisons and scientific issues. *Journal of Geophysical Research: Space Physics.* **107**(A12).

Plane, J.M.C. 2003. Atmospheric Chemistry of Meteoric Metals. *Chemical Reviews.* **103**(12), pp.4963-4984.

Plane, J.M.C. 2004. A time-resolved model of the mesospheric Na layer: constraints on the meteor input function. *Atmospheric Chemistry and Physics.* **4**, pp.627-638.

Plane, J.M.C. 2012. Cosmic dust in the earth's atmosphere. *Chemical Society Reviews.* **41**(19), pp.6507-6518.

Plane, J.M.C. 2015. *Metal Layers*. *Encyclopedia of Atmospheric Sciences.* Vol **3**. 2nd ed. Academic Press.

Plane, J.M.C., Feng, W. and Dawkins, E.C.M. 2015. The Mesosphere and Metals: Chemistry and Changes. *Chemical Reviews.* **115**(10), pp.4497-4541.

Plane, J.M.C., Flynn, G.J., Määttänen, A., Moores, J.E., Poppe, A.R., Carrillo-Sanchez, J.D. and Listowski, C. 2018. Impacts of Cosmic Dust on Planetary Atmospheres and Surfaces. *Space Science Reviews.* **214**(23).

Portmann, R.W., Daniel, J.S. and Ravishankara, A.R. 2012. Stratospheric ozone depletion due to nitrous oxide: influences of other gases. *Philosophical Transactions of the Royal Society B.* **367**(1593), pp.1256-1264.

Prasad, S.S. and Zipf, E.C. 2000. Middle Atmospheric Sources of Nitrous Oxide (N_2O): O_2(B) and N_2(A) Chemistry. *Physics and Chemistry of the Earth, Part C: Solar, Terrestrial & Planetary Science.* **25**(3), pp.213-222.

Pulkkinen, T. 2007. Space Weather: Terrestrial Perspective. *Living Reviews in Solar Physics.* **4**(1).

Randall, C.E., Harvey, V.L., Manney, G.L., Orsolini, Y., Codrescu, M., Sioris, C., Brohede, S., Haley, C.S., Gordley, L.L., Zawodny, J.M. and Russell III, J.M. 2005. Stratospheric effects of energetic particle precipitation in 2003–2004. *Geophysical Research Letters.* **32**(L05802).

Randall, C.E., Harvey, V.L., Singleton, C.S., Bernath, P.F., Boone, C.D. and Kozyra, J.U. 2006. Enhanced NOx in 2006 linked to strong upper stratospheric Arctic vortex. *Geophysical Research Letters.* **33**(L18811).

Ravishankara, A.R., Daniel, J.S. and Portmann, R.W. 2009. Nitrous Oxide (N_2O): The Dominant Ozone-Depleting Substance Emitted in the 21st Century. *Science.* **326**(5949), pp.123-125.

Rawlins, F., Ballard, S.P., Bovis, K.J., Clayton, A.M., Li, D., Inverarity, G.W., Lorenc, A.C. and Payne, T.J. 2007. The Met Office global four-dimensional variational data assimilation scheme. *Quarterly Journal of the Royal Meteorological Society.* **133**(623), pp.347-362.

Rienecker, M.M., Suarez, M.J., Gelaro, R., Todling, R., Bacmeister, J., Liu, E., Bosilovich, M.G., Schubert, S.D., Takacs, L., Kim, G.-K., Bloom, S., Chen, J., Collins, D., Conaty, A., da Silva, A., Gu, W., Joiner, J., Koster, R.D., Lucchesi, R., Molod, A., Owens, T., Pawson, S., Pegion, P., Redder, C.R., Reichle, R., Robertson, F.R., Ruddick, A.G., Sienkiewicz, M. and Woollen, J. 2011. MERRA: NASA's Modern-Era Retrospective Analysis for Research and Applications. *Journal of Climate.* **24**, pp.3624-3648.

Roble, R.G. and Ridley, E.C. 1987. An auroral model for the NCAR thermospheric general circulation model (TGCM). *Annales Geophysicae.* **5**(6), pp.369-382.

Rozanov, E., Calisto, M., Egorova, T., Peter, T. and Schmutz, W. 2012. Influence of the Precipitating Energetic Particles on Atmospheric Chemistry and Climate. *Surveys in Geophysics.* **33**, pp.483-501.

Russell III, J.M., Mlynczak, M.G., Gordley, L.L., Tansock, J. and Esplin, W. 1999. Overview of the SABER experiment and preliminary calibration results. *Proceedings of SPIE 3756: 277–88.* pp.277-288.

Russell, J.M., Bailey, S.M., Gordley, L.L., Rusch, D.W., Horányi, M., Hervig, M.E., Thomas, G.E., Randall, C.E., Siskind, D.E., Stevens, M.H., Summers, M.E., Taylor, M.J., Englert, C.R., Espy, P.J., McClintock, W.E. and Merkel, A.W. 2009. The Aeronomy of Ice in the Mesosphere (AIM) mission: Overview and early science results. *Journal of Atmospheric and Solar-Terrestrial Physics.* **71**(3-4), pp.289-299.

Schoeberl, M.R. and Newman, P.A. 2015. *Polar Vortex*. *Encyclopedia of Atmospheric Sciences.* Vol **4**. 2nd ed. Academic Press.

Schuchardt, K.G.H. and Blum, P.W. 1981. Eddy Diffusion Coefficient and Atmospheric Models. *Advances in Space Research.* **1**, pp.157-169.

Self, D.E. and Plane, J.M.C. 2002. Absolute photolysis cross-sections for NaHCO3 , NaOH, NaO, NaO2and NaO3 : implications for sodium chemistry in the upper mesosphere. *Physical Chemistry Chemical Physics.* **4**, pp.16-23.

Sellar, A.A., Jones, C.G., Mulcahy, J.P., Tang, Y., Yool, A., Wiltshire, A., O'Connor, F.M., Stringer, M., Hill, R., Palmieri, J., Woodward, S., Mora, L., Kuhlbrodt, T., Rumbold, S.T., Kelley, D.I., Ellis, R., Johnson, C.E., Walton, J., Abraham, N.L., Andrews, M.B., Andrews, T., Archibald, A.T., Berthou, S., Burke, E., Blockley, E., Carslaw, K., Dalvi, M., Edwards, J., Folberth, G.A., Gedney, N., Griffiths, P.T., Harper, A.B., Hendry, M.A., Hewitt, A.J., Johnson, B., Jones, A., Jones, C.D., Keeble, J., Liddicoat, S., Morgenstern, O., Parker, R.J., Predoi, V., Robertson, E., Siahaan, A., Smith, R.S., Swaminathan, R., Woodhouse, M.T., Zeng, G. and Zerroukat, M. 2019. UKESM1: Description and Evaluation of the U.K. Earth System Model. *Journal of Advances in Modeling Earth Systems.* **11**(12), pp.4513-4558.

Semeniuk, K., McConnell, J.C., Jin, J.J., Jarosz, J.R., Boone, C.D. and Bernath, P.F. 2008. N_2O production by high energy auroral electron precipitation. *Journal of Geophysical Research.* **113**(D16302).

Seppälä, A., Lu, H., Clilverd, M.A. and Rodger, C.J. 2013. Geomagnetic activity signatures in wintertime stratosphere wind, temperature, and wave response. *Journal of Geophysical Research: Atmospheres.* **118**(5), pp.2169-2183.

Sheese, P.E., Walker, K.A., Boone, C.D., Bernath, P.F. and Funke, B. 2016. Nitrous oxide in the atmosphere: First measurements of a lower thermospheric source. *Geophysical Research Letters.* **43**, pp.2866-2872.

Shemansky, D.E. 1969. N_2 Vegard–Kaplan System in Absorption. *Journal of Chemical Physics.* **51**(2), pp.689-700.

Sinnhuber, M., Funke, B., von Clarmann, T., López-Puertas, M., Stiller, G.P. and Seppälä, A. 2014. Variability of NOx in the polar middle atmosphere from October 2003 to March 2004: vertical transport vs. local production by energetic particles. *Atmospheric Chemistry and Physics.* **14**, pp.7681-7692.

Sinnhuber, M., Nieder, H. and Wieters, N. 2012. Energetic Particle Precipitation and the Chemistry of the Mesosphere/Lower Thermosphere. *Surveys in Geophysics.* **33**, pp.1218-1334.

Smith, A.K. 2012. Global Dynamics of the MLT. *Surveys in Geophysics.* **33**(6), pp.1177-1230.

Smith, A.K., Garcia, R.R., Marsh, D.R. and Richter, J.H. 2011. WACCM simulations of the mean circulation and trace species transport in the winter mesosphere. *Journal of Geophysical Research.* **116**(D20115).

Smith, A.K. and Perlwitz, J. 2015. *Planetary Waves*. *Encyclopedia of Atmospheric Sciences.* Vol **4**. 2nd ed. Academic Press.

Solomon, S.C. 2017. Global modeling of thermospheric airglow in the far ultraviolet. *Journal of Geophysical Research: Space Physics.* **122**, pp.7834-7848.

Solomon, S.C. and Roble, R.G. 2015. *Thermosphere*. *Encyclopedia of Atmospheric Sciences.* Vol **5**. 2nd ed. Academic Press.

States, R.J. and Gardner, C.S. 1999. Structure of the mesospheric Na layer at 40°N latitude: Seasonal and diurnal variations. *Journal of Geophysical Research.* **104**(D9), pp.11783-11798.

Stolarski, R.S., Douglass, A.R., Remsberg, E.E., Livesey, N.J. and Gille, J.C. 2012. Ozone temperature correlations in the upper stratosphere as a measure of chlorine content. *Journal of Geophysical Research: Atmospheres.* **117**(D10305).

Storkey, D., Blaker, A.T., Mathiot, P., Megann, A., Aksenov, Y., Blockley, E.W., Calvert, D., Graham, T., Hewitt, H.T., Hyder, P., Kuhlbrodt, T., Rae, J.G.L. and Sinha, B. 2018. UK Global Ocean GO6 and GO7: a traceable hierarchy of model resolutions. *Geoscientific Model Development.* **11**(8), pp.3187-3213.

Strahan, S.E. 2015. *Transport Circulation*. *Encyclopedia of Atmospheric Sciences.* Vol **4**. 2nd ed. Academic Press.

Swider, W. and Keneshea, T.J. 1973. Decrease of ozone and atomic oxygen in the lower mesosphere during a PCA event. *Planetary and Space Science.* **21**, pp.1969-1973.

Tsang, W. and Hampson, R.F. 1986. Chemical Kinetic Data Base for Combustion Chemistry. Part I. Methane and Related Compounds. *Journal of Physical and Chemical Reference Data.* **15**(1087).

Turányi, T., Nagy, T., Zsély, I.G., Cserháti, M., Varga, T., Szabó, B.T., Sedyó, I., Kiss, P.T., Zempléni, A. and Curran, H.J. 2012. Determination of rate parameters based on both direct and indirect measurements. *International Journal of Chemical Kinetics.* **44**, pp.284-302.

Varney, R.H. and Kelley, M.C. 2015. *Polar Summer Mesopause*. *Encyclopedia of Atmospheric Sciences.* Vol **3**. 2nd ed. Academic Press.

Verronen, P.T., Andersson, M.E., Marsh, D.R., Kovács, T. and Plane, J.M.C. 2016. WACCM-D-Whole Atmosphere Community Climate Model with D-region ion chemistry. *Journal of Advances in Modeling Earth Systems.* **8**(2), pp.954-975.

Verronen, P.T., Andersson, M.E., Rodger, C.J., Clilverd, M.A., Wang, S. and Turunen, E. 2013. Comparison of modeled and observed effects of radiation belt electron precipitation on mesospheric hydroxyl and ozone. *Journal of Geophysical Research: Atmospheres.* **118**(19), pp.11,419-11,428.

Verronen, P.T. and Lehmann, R. 2013. Analysis and parameterisation of ionic reactions affecting middle atmospheric HOx and NOy during solar proton events. *Annales Geophysicae.* **31**, pp.909-956.

Vincent, R.A. 2015. The dynamics of the mesosphere and lower thermosphere: a brief review. *Progress in Earth and Planetary Science.* **2**(4).

von Zahn, U. 2003. Are Noctilucent Clouds Truly a "Miner's Canary" for Global Change? *Eos, Transactions, AGU.* **84**(28), pp.261-268.

Walters, D., Baran, A.J., Boutle, I., Brooks, M., Earnshaw, P., Edwards, J., Furtado, K., Hill, P., Lock, A., Manners, J., Morcrette, C., Mulcahy, J., Sanchez, C., Smith, C., Stratton, R., Tennant, W., Tomassini, L., Van Weverberg, K., Vosper, S., Willett, M., Browse, J., Bushell, A., Carslaw, K., Dalvi, M., Essery, R., Gedney, N., Hardiman, S., Johnson, B., Johnson, C., Jones, A., Jones, C., Mann, G., Milton, S., Rumbold, H., Sellar, A., Ujiie, M., Whitall, M., Williams, K. and Zerroukat, M. 2019. The Met Office Unified Model Global Atmosphere 7.0/7.1 and JULES Global Land 7.0 configurations. *Geoscientific Model Development.* **12**(5), pp.1909-1963.

Wild, O., Zhu, X. and Prather, M.J. 2000. Fast-J: Accurate Simulation of In- and Below-Cloud Photolysis in Tropospheric Chemical Models. *Journal of Atmospheric Chemistry.* **37**, pp.245-282.

Wood, N., Staniforth, A., White, A., Allen, T., Diamantakis, M., Gross, M., Melvin, T., Smith, C., Vosper, S., Zerroukat, M. and Thuburn, J. 2014. An inherently mass-conserving semi-implicit semi-Lagrangian discretization of the deep-atmosphere global non-hydrostatic equations. *Quarterly Journal of the Royal Meteorological Society.* **140**(682), pp.1505-1520.

Xu, J. and Smith, A.K. 2003. Perturbations of the sodium layer: controlled by chemistry or dynamics? *Geophysical Research Letters.* **30**(20).

Xu, J. and Smith, A.K. 2004. Studies of gravity wave–induced fluctuations of the sodium layer using linear and nonlinear models. *Journal of Geophysical Research.* **109**(D02306).

Zhou, Q., Friedman, J., Raizada, S., Tepley, C. and Morton, Y.T. 2005. Morphology of nighttime ion, potassium and sodium layers in the meteor zone above Arecibo. *Journal of Atmospheric and Solar-Terrestrial Physics.* **67**(13), pp.1245-1257.

Zipf, E.C. and Prasad, S.S. 1982. A mesospheric source of nitrous oxide. *Nature.* **295**, pp.133-135.

LIST OF ABBREVIATIONS

ACE-FTS	**A**tmospheric **C**hemistry **E**xperiment - **F**ourier **T**ransform **S**pectrometer
BDC	**B**rewer **D**obson **C**irculation
CESM	**C**ommunity **E**arth **S**ystem **M**odel
CIRA	**C**OSPAR **I**nternational **R**eference **A**tmosphere
CMAM	**C**anadian **M**iddle **A**tmosphere **M**odel
CME	**C**oronal **M**ass **E**jection
COSPAR	**C**ommittee **O**n **SPA**ce **R**esearch
COST	European **CO**operation in **S**cience and **T**echnology
EEP	**E**nergetic **E**lectron **P**recipitation
EPP	**E**nergetic **P**article **P**recipitation
EUV	**E**xtreme-**UV**
FUV	**F**ar-**UV**
GCR	**G**alactic **C**osmic **R**ay
GLOW	**GL**obal Airgl**OW**
GOMOS	**G**lobal **O**zone **M**easurement by **O**ccultation of **S**tars
HEE	**H**igh-**E**nergy **E**lectrons
ICS	**I**ntegrated **C**ross-**S**ection
LEE	**L**ow-**E**nergy **E**lectrons
LTE	**L**ocal **T**hermodynamic **E**quilibrium
MEE	**M**edium-**E**nergy **E**lectrons
MEPED	**M**edium **E**nergy **P**roton and **E**lectron **D**etector
MERRA	**M**odern-**E**ra **R**etrospective analysis for **R**esearch and **A**pplications
MIF	**M**eteoric **I**nput **F**unction

MIPAS	**M**ichelson **I**nterferometer for **P**assive **A**tmospheric **S**ounding
MLT	**M**esosphere-**L**ower **T**hermosphere
MMR	**M**ass **M**ixing **R**atio
MSIS	**M**ass **S**pectrometer **I**ncoherent **S**catter
NCAR	**N**ational **C**enter for **A**tmospheric **R**esearch
NCAS	**N**ational **C**entre for **A**tmospheric **S**cience
NH	**N**orthern **H**emisphere
NLTE	**N**on-**L**ocal **T**hermodynamic **E**quilibrium
NOAA	**N**ational **O**ceanic and **A**tmospheric **A**dministration
NRL	**N**aval **R**esearch **L**aboratory
OSIRIS	**O**ptical **S**pectrograph and **I**nfra-**R**ed **I**mager **S**ystem
POES	**P**olar **O**rbiting **E**nvironmental **S**atellites
SAA	**S**outh **A**tlantic Magnetic **A**nomaly
SABER	**S**ounding of the **A**tmosphere using **B**roadband **E**mission **R**adiometry
SCIAMACHY	**SC**anning **I**maging **A**bsorption spectro**M**eter for **A**tmospheric **CH**artograph**Y**
SH	**S**outhern **H**emisphere
SPE	**S**olar **P**roton **E**vent
SSW	**S**udden **S**tratospheric **W**arming
TEM	**T**ransformed **E**ulerian **M**ean
TIMED	**T**hermosphere-**I**onosphere-**M**esosphere **E**nergetics and **D**ynamics
UKCA	**UK C**hemistry and **A**erosols
UKESM	**UK E**arth **S**ystem **M**odel
UM	**U**nified **M**odel
USSA	**US S**tandard **A**tmosphere
VMR	**V**olume **M**ixing **R**atio

WACCM	**W**hole **A**tmosphere **C**ommunity **C**limate **M**odel
WACCM-D	**W**hole **A**tmosphere **C**ommunity **C**limate **M**odel with **D** region ion chemistry
WACCM-X	**W**hole **A**tmosphere **C**ommunity **C**limate **M**odel with thermosphere and ionosphere e**X**tension

APPENDIX: TECHNICAL STEPS FOR UKCA COMPATIBILITY WITH THE EXTENDED UM

A.1 Introduction

This appendix provides an overview of the technical steps completed to enable compatibility between UKCA and the Extended UM. It is intended that this supplement could provide a useful resource to developers of the Extended UM-UKCA who wish to recreate the modifications made to enable the basic configuration of the model that is used in this thesis. In Section A.2, I list the additional input file requirements specific to running UKCA at a different number of vertical levels. In Section A.3, I outline the changes made to the Rose framework for running meteorological suites. In Section A.4, I summarise the relevant UM source code changes. Note that these technical steps are valid for version 11.3 of the UM. To be used with later versions of the model, some adjustments may be required.

A.2 Input Files

It is a prerequisite that all 3D UKCA input files are transformed from the original 85-level (85 km lid) vertical grid to the extended 100-level (120 km lid) vertical grid. This includes:

- the model start dump (containing all dynamical, chemical and state variables);
- chemical emissions (aircraft NO_x);
- and the aerosol climatology ancillaries (including biogenic, biomass burning, black carbon, organic carbon, dust, sea salt, sulphate and unspecified).

A model start dump on user defined vertical levels is generated by the Reconfiguration task in the UM workflow. Reconfiguration requires the model to have successfully built before functioning. Therefore, it is necessary to make the changes in Sections A.3.1 and A.3.2 first. The only chemical emission file that requires a transformation onto the 100-level (L100) grid is that for aircraft NO_x. This can be done offline by using IRIS to append 15 additional levels containing zero emissions above the original

85-level (L85) file. For the aerosol ancillaries, there is currently no straightforward way of transforming their vertical resolution. Hence, Met Office assistance is recommended for this task.

A.3 Rose Suite Settings

Chemistry changes should be built into a Rose suite configured for the Extended UM. A suitable starting point is suite I.D. u-bl305 at revision number 154213.

A.3.1 Switch on UKCA

The first task is to switch on UKCA without GLOMAP, initially under the StratTrop chemistry scheme. The necessary suite changes required for this are available through the aeroclim-chem UM optional configuration file, documented under ticket #183 on the Rose repository.

A.3.2 Generation of Start Dumps

The second task is to generate a compatible model start dump containing the UKCA fields. At first instance, this will be on the L85 grid. This can be done by running the Build UM and Reconfiguration tasks without any L100 UM or Ancillary optional configuration keys specified. Next, the resulting L85 start dump needs to be transformed onto the L100 grid. Set the suite to initialise from the new start dump and configure each UKCA tracer to read from the same location. Now, re-run the Build UM and Reconfiguration tasks, this time with the L100 UM and Ancillary optional configuration keys. This will produce a start dump that includes UKCA fields on the L100 grid.

A.3.3 Additional Modifications

Finally, there are a few additional modifications required to ensure that the suite runs correctly. The first two of which are UKCA settings.

1. Set the Fast-JX mode (for the photolysis treatment above the Fast-JX cut-off) to ‘Fast-JX and lookup table’. Testing revealed this setting to produce the most reliable results.

2. Set the UKCA top boundary (for the optional overwriting of tracer densities for selected UKCA species) to 'No top boundary condition'. Existing treatments are incompatible with the additional vertical model levels.

The last modification refers to the tuning of the model in aid of stability.

3. Increase the vertical damping coefficient to a factor of 0.25. Testing revealed this to be the lowest factor that could reliably complete a 2-year simulation.

Before the model can be run successfully, UM source code modifications need to be made. The changes specified in Section A.4.1 are sufficient to run with the StratTrop scheme, while the changes in Section A.4.2 are also required to run with the Strat scheme. By default, the aeroclim-chem UM optional configuration key selects the StratTrop scheme. To use the Strat scheme instead (recommended), it will need to be manually selected. The suite will also need to be set to read the STASHMaster file from the new branch. In addition, all chemical emission files aside from CH_4, CO, NO, HCHO and aircraft NO_x will need to be deallocated from the suite.

A.4 UM Branch Settings

Chemistry changes should be applied to new branches. This must be done incrementally, first to enable simulations using the StratTrop scheme, then to enable simulations using the Strat scheme.

A.4.1 StratTrop Scheme

One minor code change is necessary to remove a problematic reference to the original model lid height. In the 'ukca_calc_ozone_col' subroutine of the 'ukca_strat_update' module, delete the condition '.AND. z_top_of_model < 85500.0'.

A.4.2 Strat Scheme

In addition to the above change, a collection of further code changes are required to run with the Strat scheme. The necessary changes are available at vn11.1 in the 'lukeabraham/vn11.1_ukca_change_diagnostics' branch, upgradable to vn11.3.